

N67-15901-29  
NASA CR 81209

NATIONAL AERONAUTICS AND SPACE ADMINISTRATION

*Space Programs Summary 37-42, Vol. III*

*The Deep Space Network*

For the Period September 1 to October 31, 1966

FACILITY FORM 802

N67 15901

(ACCESSION NUMBER)

138

(PAGES)

CR-81209

(NASA CR OR TMX OR AD NUMBER)

N67 15929

(THRU)

1

(CODE)

07

(CATEGORY)

GPO PRICE \$ \_\_\_\_\_

CFSTI PRICE(S) \$ \_\_\_\_\_

Hard copy (HC) 3.00

Microfiche (MF) 1.95

ff 653 July 65

JET PROPULSION LABORATORY  
CALIFORNIA INSTITUTE OF TECHNOLOGY  
PASADENA, CALIFORNIA

November 30, 1966

NATIONAL AERONAUTICS AND SPACE ADMINISTRATION

*Space Programs Summary 37-42, Vol. III*

*The Deep Space Network*

For the Period September 1 to October 31, 1966

**JET PROPULSION LABORATORY  
CALIFORNIA INSTITUTE OF TECHNOLOGY  
PASADENA, CALIFORNIA**

November 30, 1966

Space Programs Summary 37-42, Vol. III

Copyright © 1967  
Jet Propulsion Laboratory  
California Institute of Technology  
Prepared Under Contract No. NAS 7-100  
National Aeronautics & Space Administration

## Preface

The Space Programs Summary is a six-volume bimonthly publication designed to report on JPL space exploration programs and related supporting research and advanced development projects. The titles of all volumes of the Space Programs Summary are:

- Vol. I. *The Lunar Program* (Confidential)
- Vol. II. *The Planetary-Interplanetary Program* (Confidential)
- Vol. III. *The Deep Space Network* (Unclassified)
- Vol. IV. *Supporting Research and Advanced Development* (Unclassified)
- Vol. V. *Supporting Research and Advanced Development* (Confidential)
- Vol. VI. *Space Exploration Programs and Space Sciences* (Unclassified)

The Space Programs Summary, Vol. VI, consists of: an unclassified digest of appropriate material from Vols. I, II, and III; an original presentation of the JPL quality assurance and reliability efforts, and the environmental- and dynamic-testing facility-development activities; and a reprint of the space science instrumentation studies of Vols. I and II.

Approved by:



W. H. Pickering, Director

Jet Propulsion Laboratory

## Contents

<b>I. Introduction</b> . . . . .	1
<b>II. Tracking and Navigational Accuracy Analysis</b> . . . . .	3
A. DSN Inherent Accuracy Project <i>T. W. Hamilton and D. W. Trask</i> . . . . .	3
B. Effect of Constant Acceleration on the Information Content of a Single Pass of Doppler Data <i>T. Nishimura</i> . . . . .	3
C. Entry Capsule Orbit Determination Accuracy <i>C. Scranage</i> . . . . .	8
D. The JPL Matrix Operations Programming System <i>P. M. Muller</i> . . . . .	12
E. Theoretical Basis for the Double Precision Orbit Determination Program: V. Doppler and Range Observations <i>T. D. Moyer</i> . . . . .	15
F. Pioneer Project Support <i>D. W. Curkendall, J. E. Ball, and J. F. Gallagher</i> . . . . .	21
References . . . . .	23
<b>III. Communications Research and Development</b> . . . . .	24
A. Frequency Generation and Control: Atomic Hydrogen Frequency Standard <i>W. H. Higa</i> . . . . .	24
B. Improved RF Calibration Techniques: Daily System Noise Temperature Measurements <i>C. T. Stelzried</i> . . . . .	25
C. Improved RF Calibration Techniques: Weekly Noise Temperature Calibrations <i>T. Y. Otoshi</i> . . . . .	32
D. Efficient Antenna Systems: Calculated Gain of the Advanced Antenna System <i>A. C. Ludwig</i> . . . . .	37
E. Efficient Antenna Systems: X-Band Gain Measurements <i>D. A. Bathker, and G. S. Levy</i> . . . . .	40
F. Low Noise Receivers: Microwave Maser Development <i>S. M. Petty, and R. C. Clauss</i> . . . . .	42
G. X-Band Cone RF Instrumentation <i>C. T. Stelzried</i> . . . . .	46
H. Digital Communication and Tracking: Ranging Measurement <i>R. C. Tausworthe</i> . . . . .	52

## Contents (contd)

I. Digital Communication and Tracking: Ranging Subsystem Acquisition Probabilities	56
<i>R. Didday</i> . . . . .	
J. Digital Communication and Tracking: a Phase-Locked Receiver Analysis Program	60
<i>R. C. Tausworthe</i> . . . . .	
K. Digital Communication and Tracking: Time Synchronization Experiment	61
<i>W. Martin</i> . . . . .	
L. Frequency Generation and Control: VCO Noise Measurement and Optimum Tracking Filters	67
<i>C. Cooper</i> . . . . .	
M. Frequency Generation and Control: S- and X-Band Central Frequency Synthesizer	71
<i>G. U. Barbani</i> . . . . .	
References . . . . .	74
<b>IV. Communications Engineering Development</b> . . . . .	<b>77</b>
A. S-Band Receiver-Exciter Ranging Subsystem (RER), Blocks IIA and IIIC	77
<i>H. Donnelly, C. E. Johns, R. W. Tappan, and M. R. Wick</i> . . . . .	
B. 57/221 Frequency Shifter—Block IIB	88
<i>C. E. Johns</i> . . . . .	
References . . . . .	86
<b>V. Deep Space Station Engineering and Operations</b> . . . . .	<b>87</b>
A. Flight Project Support	87
<i>J. Orbison</i> . . . . .	
B. Facility Construction and Equipment Installation	88
<i>J. Orbison</i> . . . . .	
C. Mariner Venus 67 Project: Ground Instrumentation for Occultation	90
<i>G. Levy</i> . . . . .	
D. Venus DSS Operations	92
<i>M. A. Gregg, E. B. Jackson, and A. L. Price</i> . . . . .	
E. DSIF FR-900 Video Recorders	95
<i>W. C. Allen</i> . . . . .	
F. DSIF Station Control Data and Equipment	96
<i>R. Flanders, G. Jenkins, A. Burke, W. Frey, and H. Baugh</i> . . . . .	
G. Conference Nets of the Operational Voice Communications Subsystems	98
<i>F. E. Bond, Jr., and J. W. Capps</i> . . . . .	

## I. Introduction

The Deep Space Network (DSN), established by the NASA Office of Tracking and Data Acquisition, is under the system management and technical direction of JPL. The DSN is responsible for two-way communications with unmanned spacecraft travelling from approximately 10,000 miles from Earth to interplanetary distances. Tracking and data-handling equipment to support these missions is provided. Present facilities permit simultaneous control of a newly launched spacecraft and a second one already in flight. In preparation for the increased number of U.S. activities in space, a capability is being developed for simultaneous control of either two newly launched spacecraft plus two in flight, or four spacecraft in flight. Advanced communications techniques are being implemented to make possible obtaining data from, and tracking spacecraft to, planets as far out in space as Jupiter.

The DSN is distinct from other NASA networks such as the Space Tracking and Data Acquisition Network (STADAN), which tracks Earth-orbiting scientific and communication satellites, and the Manned Space Flight Network (MSFN), which tracks the manned spacecraft of the *Gemini* and *Apollo* programs.

The DSN supports, or has supported, the following NASA space exploration projects: (1) *Ranger*, *Surveyor*, *Mariner*, and *Voyager* Projects of JPL; (2) *Lunar Orbiter* Project of the Langley Research Center; (3) *Pioneer* Project of the Ames Research Center, and (4) *Apollo* Project of the Manned Spacecraft Center (as backup to the Manned Space Flight Network). The main elements of the network are: the Deep Space Instrumentation Facility (DSIF), with space communications and tracking stations located around the world; the Ground Communi-

cations System (GCS), which provides communications between all elements of the DSN; and the JPL Space Flight Operations Facility (SFOF), the command and control center.

The DSIF tracking stations are situated such that three stations may be selected approximately 120 deg apart in longitude in order that a spacecraft in or near the ecliptic plane is always within the field of view of at least one of the selected ground antennas. The DSIF stations are:

Deep Space Communication Complex (DSCC)	Deep Space Station (DSS)	DSS serial designation
Goldstone	Pioneer	11
	Echo	12
	Venus	13
	Mars	14
Canberra	Woomera	41
	Tidbinbilla	42
	Booroomba <sup>2</sup>	43
	Johannesburg	51
Madrid <sup>1</sup>	Robledo	61
	Cebreros <sup>2</sup>	62
	Rio Cofio <sup>2</sup>	63
	Cape Kennedy (Spacecraft Monitoring)	71
	Ascension Island (Spacecraft Guidance and Command)	72
<sup>1</sup> Planned. <sup>2</sup> Station not yet authorized. <sup>3</sup> Station not yet operational.		

JPL operates the U.S. stations, and will operate the Ascension Island Station. The overseas stations are normally staffed and operated by government agencies of the respective countries, with the assistance of U.S. support personnel.

The Cape Kennedy Station supports spacecraft final checkout prior to launch, verifies compatibility between the DSN and the flight spacecraft, measures spacecraft frequencies during countdown, and provides telemetry reception from lift-off to local horizon. The other DSIF stations obtain angular position, velocity (doppler), and distance (range) data for the spacecraft, and provide command control to (up-link), and data reception from (down-link), the spacecraft. Large antennas, low noise phase-lock receiving systems, and high-power transmitters are utilized. The 85-ft diam antennas have gains of 53 db at 2300 MHz, with a system temperature of 55°K, making possible the receipt of significant data rates at distances as far as the planet Mars. To improve the data rate and distance capability, a 210-ft diam antenna has been built at DSS 14, and two additional antennas of this size are planned for installation at overseas stations.

In their present configuration all stations, with the exception of Johannesburg, are full S-band stations. The Johannesburg receiver has the capability for L- to S-band conversion.

It is the policy of the DSN to continuously conduct research and development of new components and systems and to engineer them into the network to maintain a state-of-the-art capability. Therefore, the Goldstone stations are also used for extensive investigation of space tracking and telecommunications techniques, establishment of DSIF/spacecraft compatibility, and development of new DSIF hardware and software. New DSIF-system equipment is installed and tested at the Goldstone facili-

ties before being accepted for system-wide integration into the DSIF. After acceptance for general use, it is classed as Goldstone Duplicate Standard (GSDS) equipment, thus standardizing the design and operation of identical items throughout the system.

The GCS consists of voice, teletype, and high-speed data circuits provided by the NASA World-Wide Communications Network between each overseas station, the Cape Kennedy Station, and the SFOF. Voice, teletype, high-speed data, and video circuits between the SFOF and the Goldstone stations are provided by a DSN microwave link. The NASA Communications Network is a global network consisting of more than 100,000 route mi and 450,000 circuit mi, interconnecting 89 stations of which 34 are overseas in 18 foreign countries. It is entirely operationally oriented and comprises those circuits, terminals, and switching equipments interconnecting tracking and data acquisition stations with, for example, mission control, project control, and computing centers. Circuits used exclusively for administrative purposes are not included.

During the support of a spacecraft, the entire DSN operation is controlled by the SFOF. All spacecraft command, data processing, and data analysis can be accomplished within this facility. The SFOF, located in a three-story building at JPL, utilizes operations control consoles, status and operations displays, computers, and data-processing equipment for the analysis of spacecraft performance and space science experiments, and communications facilities to control space flight operations. This control is accomplished by generating trajectories and orbits, command and control data from tracking and telemetry data received from the DSIF in near-real time. The SFOF also reduces the telemetry, tracking, command, and station performance data recorded by the DSIF into engineering and scientific information for analysis and use by scientific experimenters and spacecraft engineers.

## II. Tracking and Navigational Accuracy Analyses

### A. DSN Inherent Accuracy Project, **N67 15902** *T. W. Hamilton* and D. W. Trask

The DSN Inherent Accuracy Project was formally established by the DSN Executive Committee in July 1965. The objectives of the Project are:

- (1) Determination (and verification) of the inherent accuracy of the DSN as a radio navigation instrument for lunar and planetary missions.
- (2) Formulation of designs and plans for refining this accuracy to its practical limits.

Achievement of these goals is the joint responsibility of the Telecommunications Division (33) and the Systems Division (31) of JPL. To this end, regular monthly meetings are held to coordinate and initiate relevant activities. The Project leader and his assistant (from Divisions 31 and 33, respectively) report to the DSN Executive Committee, and are authorized to task Project members to (1) conduct analyses of proposed experiments, (2) prepare reports on current work, and (3) write descriptions of proposed experiments. The Project is further authorized to deal directly with those flight projects using the DSN regarding data-gathering procedures that bear on inherent accuracy.

The various data types and tracking modes provided by the DSIF in support of lunar and planetary missions are discussed in *SPS 37-39*, Vol. III, pp. 6-8.

Technical work directly related to the Inherent Accuracy Project was presented in *SPS 37-38*, Vol. III, and in subsequent issues, and is continued in the following sections of this volume.

### B. Effect of Constant Acceleration on the Information Content of a Single Pass of Doppler Data, **N67 15903** *T. Nishimura*

#### 1. Introduction

In *SPS 37-33*, Vol. IV, pp. 8-16, J. O. Light has pointed out that the velocity parallax effect due to the rotation of the ground station around the Earth's spin axis plays a dominant role in the orbit redetermination when the information is supplied by a single pass of doppler data from a distant spacecraft. Then T. W. Hamilton and W. G. Melbourne have clarified (*SPS 37-39*, Vol. III, pp. 18-23) that the mean geocentric radial velocity, its right ascension, and the cosine of its declination are three major parameters that can be meaningfully measured from a full pass of doppler data. D. Curkendall (*SPS 37-41*,

Vol. III, pp. 47-50) has extended the analysis to the case when the noise in information may be regarded as white range noise.

It is the objective of this article to evaluate the extent to which a small constant acceleration acting on the spacecraft (solar pressure, gas leakage) will affect the estimates of the three major parameters mentioned above, especially the cosine of declination of the spacecraft's trajectory.

A definition of terms used appears at the end of this article.

## 2. Mathematical Model

The assumptions made in this article are identical with those of Hamilton and Melbourne; namely, the spacecraft is moving away from the Earth with an almost straight line motion while the observer (tracking station) is rotating around the  $z$ -axis at a distance  $r_s$  (Fig. 1).

The range  $\rho$  from the observer to the spacecraft is given by

$$\rho^2 = (x - r_s \cos \theta)^2 + (y - r_s \sin \theta)^2 + (z - z_s)^2 \quad (1)$$

Differentiating Eq. (1) with respect to time yields

$$\begin{aligned} \rho \dot{\rho} = & r \dot{r} - r_s (\dot{x} \cos \theta + \dot{y} \sin \theta) - \dot{z} z_s \\ & + r_s \dot{\theta} (x \sin \theta - y \cos \theta) \end{aligned} \quad (2)$$

The speed components  $\dot{x}$ ,  $\dot{y}$ ,  $\dot{z}$ , are described as follows under the constant acceleration

$$\dot{x} = \dot{x}_0 + L_x (t - t_0) \quad (3)$$

$$\dot{y} = \dot{y}_0 + L_y (t - t_0) \quad (4)$$

$$\dot{z} = \dot{z}_0 + L_z (t - t_0) \quad (5)$$

and the angular rate  $\dot{\theta}$  is given by

$$\dot{\theta} = \omega \quad (6)$$

However, for the probe at a distance  $r \gg r_s$ ,  $r \gg z_s$ , Eq. (2) can be simplified by dividing by  $\rho$ , expanding it in terms of  $1/r$ , then dropping higher-order terms. It is also assumed that the positional coordinates of the probe at time  $t$  do not deviate significantly from the original straight line at time  $t_0$ , so that the same rotational cosines are employed throughout a pass

$$\dot{\rho} \doteq \dot{r} + r_s \omega \cos \delta \cos \theta_0 \sin \theta - r_s \omega \sin \theta_0 \cos \delta \cos \theta \quad (7)$$

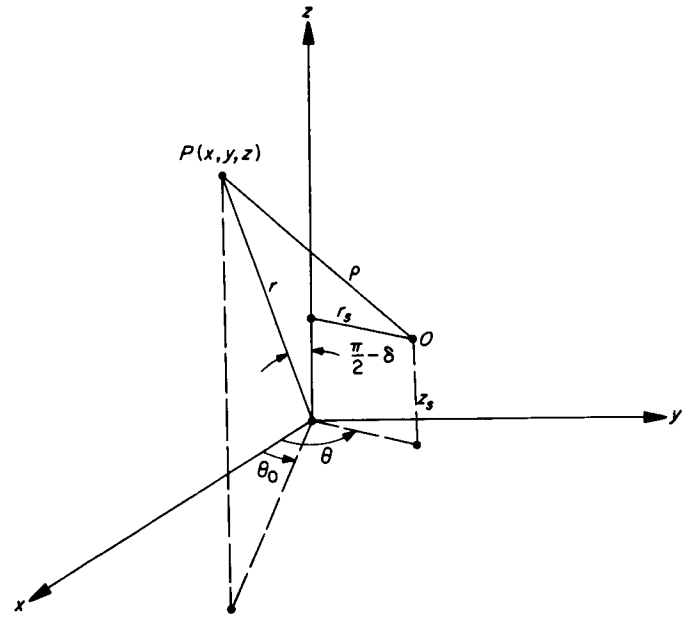


Fig. 1. Coordinates of probe P and observer O

Let  $\dot{r}_0$  and  $L_r$ , respectively, be the projections of the velocity vector and the constant acceleration vector on  $\bar{r}$  vector at time  $t_0$ . Then

$$\dot{r} = \dot{r}_0 + L_r (t - t_0) \quad (8)$$

Now, by employing the fact that  $t_0 \doteq 0$ , and adding the white doppler noise  $n(t)$ , Eq. (7) can be rewritten in the following form:

$$\dot{\rho} = a + b \sin \theta + c \cos \theta + d \theta + n \quad (9)$$

where

$$a = \dot{r}_0 - L_r t_0 \doteq \dot{r}_0 \quad (10)$$

$$b = r_s \omega \cos \delta \cos \theta_0 \doteq r_s \omega \cos \delta \quad (11)$$

$$c = -r_s \omega \cos \delta \sin \theta_0 \doteq -\theta_0 r_s \omega \cos \delta \quad (12)$$

$$d = L_r / \omega \quad (13)$$

## 3. Minimum Variance Filter Design

When we have almost continuous doppler data (e.g., 1 sample per minute) contaminated by white noise, continuous estimators  $\hat{a}$ ,  $\hat{b}$ ,  $\hat{c}$ , and  $\hat{d}$  can be designed which yield minimum variance estimates of constant parameters  $a$ ,  $b$ ,  $c$ , and  $d$ , respectively.

Following the standard design procedure of the minimum variance filters, the covariance matrix  $\Lambda(\psi)$  associated with the estimator is derived as

$$\Lambda(\psi) = [\Lambda(0)^{-1} + J(\psi)]^{-1} \quad (14)$$

$$J(\psi) = \frac{1}{\Phi_{\dot{\rho}} \omega} \int_{-\psi}^{\psi} A'(\theta) A(\theta) d\theta \quad (15)$$

where  $A(\theta)$  is the observation matrix defined as

$$A(\theta) = [1, \sin \theta, \cos \theta, \theta] \quad (16)$$

and  $\psi$  is the half-width of the pass ( $-\psi \leq \theta \leq \psi$ ) and  $\Phi_{\dot{\rho}}$  is the power spectral density of white noise  $n$ . When  $N$  observations are made over a pass at an equally spaced time interval  $T$ , the mean squared value of  $\sigma_{\dot{\rho}}^2$  of the discrete data noise is related to the power spectral density  $\Phi_{\dot{\rho}}$  by the following:

$$\sigma_{\dot{\rho}}^2 = \frac{\Phi_{\dot{\rho}}}{T} = N \cdot \frac{\omega \Phi_{\dot{\rho}}}{2\psi} \quad (17)$$

When no *a priori* information is available,  $\Lambda(0)^{-1}$  becomes zero, so that  $\Lambda(\psi)$  is simply reduced to

$$\Lambda(\psi) = J(\psi)^{-1} \quad (18)$$

assuming  $J(\psi)$  is nonsingular.

Carrying out the integration of Eq. (15),  $\Lambda(\psi)$  is found to be

$$\Lambda(\psi) = \frac{\omega \Phi_{\dot{\rho}}}{2\psi} \begin{bmatrix} \frac{1}{1 - \rho_{13}^2} & 0 & \frac{-2 \sin \psi}{(\psi + \frac{1}{2} \sin 2\psi)(1 - \rho_{13}^2)} & 0 \\ 0 & \frac{2\psi}{(\psi - \frac{1}{2} \sin 2\psi)(1 - \rho_{24}^2)} & 0 & \frac{-6(\sin \psi - \psi \cos \psi)}{\psi^2(\psi - \frac{1}{2} \sin 2\psi)(1 - \rho_{24}^2)} \\ \frac{-2 \sin \psi}{(\psi + \frac{1}{2} \sin 2\psi)(1 - \rho_{13}^2)} & 0 & \frac{2\psi}{(\psi + \frac{1}{2} \sin 2\psi)(1 - \rho_{13}^2)} & 0 \\ 0 & \frac{-6(\sin \psi - \psi \cos \psi)}{\psi^2(\psi - \frac{1}{2} \sin 2\psi)(1 - \rho_{24}^2)} & 0 & \frac{3}{\psi^2(1 - \rho_{24}^2)} \end{bmatrix} \quad (19)$$

where

$$\rho_{13} = -\frac{\sin \psi}{\psi} \left( \frac{2}{1 + \frac{1}{2\psi} \sin 2\psi} \right)^{1/2} \quad (20)$$

$$\rho_{24} = -\frac{\sin \psi - \psi \cos \psi}{\psi^3} \left( \frac{6\psi^3}{\psi - \frac{1}{2} \sin 2\psi} \right)^{1/2} \quad (21)$$

When we compare this with the results of Hamilton and Melbourne (Eq. 3, SPS 37-39, Vol. III, p. 19), distinguishing the components of their matrix by putting a bar at the top, we observe

$$\sigma_{\hat{a}} = \bar{\sigma}_{\hat{a}} \quad (22)$$

$$\sigma_{\hat{c}} = \bar{\sigma}_{\hat{c}} \quad (23)$$

but

$$\bar{\sigma}_b = \frac{\bar{\sigma}_b}{(1 - \rho_{24}^2)^{1/2}} > \bar{\sigma}_b \text{ for } |\rho_{24}| > 0 \quad (24)$$

The estimators  $\hat{a}$ ,  $\hat{b}$ ,  $\hat{c}$ , and  $\hat{d}$  are also constructed, setting their *a priori* values equal to zero.

$$\hat{a} = \frac{1}{2(1 - \rho_{13}^2)\psi} \left[ \int_{-\psi}^{\psi} \dot{\rho}(\theta) d\theta - \frac{2 \sin \psi}{\psi + \frac{1}{2} \sin 2\psi} \int_{-\psi}^{\psi} \dot{\rho}(\theta) \cos \theta d\theta \right] \quad (25)$$

$$\hat{b} = \frac{1}{(\psi - \frac{1}{2} \sin 2\psi)(1 - \rho_{24}^2)} \left[ \int_{-\psi}^{\psi} \dot{\rho}(\theta) \sin \theta d\theta - \frac{3(\sin \psi - \psi \cos \psi)}{\psi^3} \int_{-\psi}^{\psi} \dot{\rho}(\theta) \theta d\theta \right] \quad (26)$$

$$\hat{c} = \frac{1}{(\psi + \frac{1}{2} \sin 2\psi)(1 - \rho_{13}^2)} \left[ \int_{-\psi}^{\psi} \dot{\rho}(\theta) \cos \theta d\theta - \frac{\sin \psi}{\psi} \int_{-\psi}^{\psi} \dot{\rho}(\theta) d\theta \right] \quad (27)$$

$$\hat{d} = \frac{3}{2\psi^3(1 - \rho_{24}^2)} \left[ \int_{-\psi}^{\psi} \dot{\rho}(\theta) \theta d\theta - \frac{2(\sin \psi - \psi \cos \psi)}{\psi - \frac{1}{2} \sin 2\psi} \int_{-\psi}^{\psi} \dot{\rho}(\theta) \sin \theta d\theta \right] \quad (28)$$

The correlation factors  $\rho_{13}$  and  $\rho_{24}$  are plotted in Fig. 2, and square roots of the diagonal elements of the  $\Lambda$  matrix are depicted in Fig. 3.

Suppose that the doppler data are processed as if there were no acceleration, whereas the spacecraft is actually subject to an acceleration  $L_r$ . Then the actual estimate of  $b$ , which is denoted  $\bar{b}_a$ , would be different from  $\bar{b}$ , the optimal estimate for the no-acceleration case. According to Hamilton and Melbourne,  $\bar{b}$  is given by

$$\bar{b} = \frac{1}{\psi - \frac{1}{2} \sin 2\psi} \int_{-\psi}^{\psi} \dot{\rho}(\theta) \sin \theta d\theta \quad (29)$$

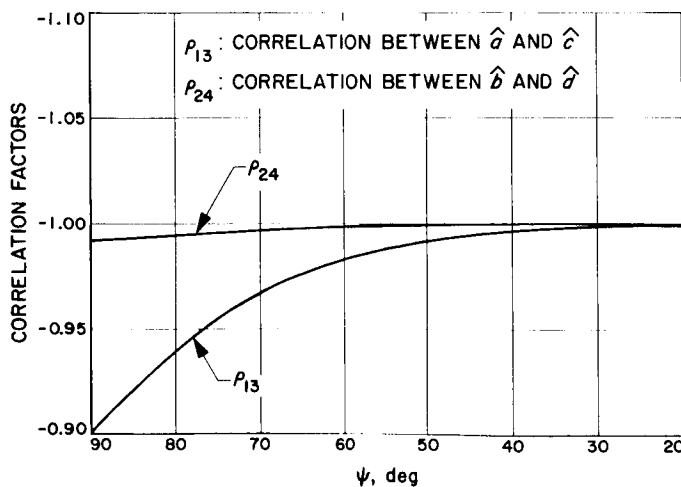


Fig. 2. Correlation factors of estimators

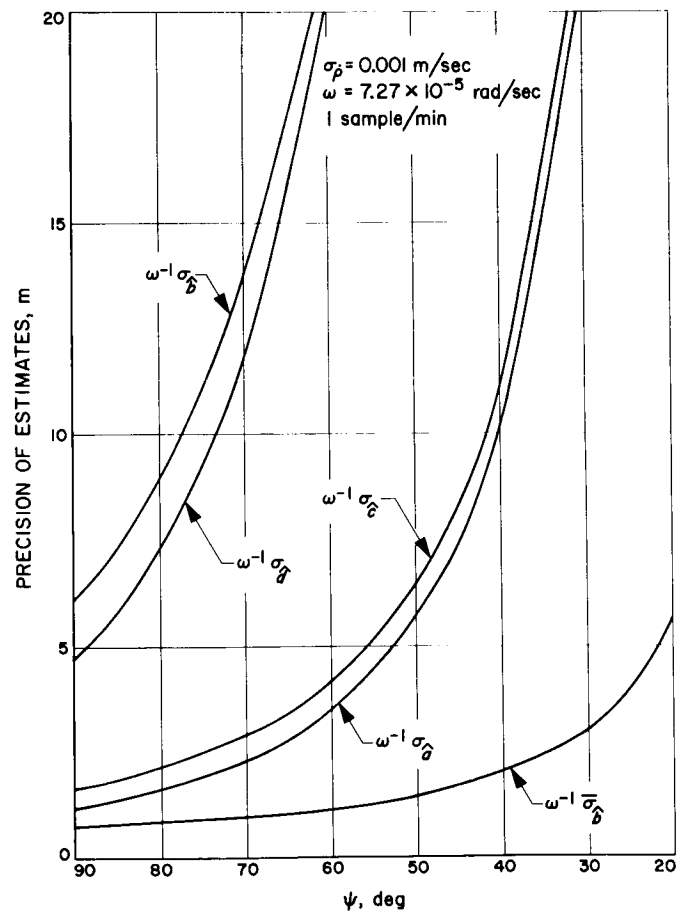


Fig. 3. Precisions of estimators  $\hat{a}$ ,  $\hat{b}$ ,  $\hat{c}$ ,  $\hat{d}$  with half-width of pass  $\psi$

Then  $\widehat{b}_a$  is computed using  $\dot{\rho}$  of Eq. (9) for nonzero  $d$  as the actual data in the above equation.

The variance associated with this actual estimate  $\widehat{b}_a$ , denoted as  $\lambda_{\delta}$ , is an ensemble average of  $(\widehat{b}_a - b)^2$ , which is found to be

$$\lambda_{\delta} = \bar{\sigma}_{\delta}^2 + \frac{4d^2 (\sin \psi - \psi \cos \psi)^2}{(\psi - \frac{1}{2} \sin 2\psi)^2} - \bar{\sigma}_{\delta}^2 + \Delta\lambda_{\delta} \quad (30)$$

When  $\psi = 90$  deg,  $\omega^{-2}\Delta\lambda_{\delta}$  becomes

$$\omega^{-2}\Delta\lambda_{\delta} = \frac{16L_r^2}{\omega^4\pi^2} \doteq 0.64 \times 10^{17} \times L_r^2 \text{ (m}^2\text{)} \quad (31)$$

#### 4. Discussion

The variances  $\sigma_{\delta}^2$  and  $\sigma_{\theta}^2$ , respectively associated with the estimate of the geocentric radial velocity and the right ascension, are not affected by the constant acceleration because the even functions 1 and  $\cos \theta$  over  $-\psi \leq \theta \leq \psi$  are orthogonal to the odd function  $\theta$ . Therefore, these two quantities remain identical with those obtained by Hamilton and Melbourne.

The variance  $\sigma_{\delta}^2$  associated with the estimate of the cosine of declination is severely degraded by the presence of constant acceleration because the odd function  $\sin \theta$  is nonorthogonal to the odd function  $\theta$  over  $-\psi \leq \theta \leq \psi$ . These two quantities are strongly correlated over the intervals  $0 \leq \psi \leq 90$  deg, as observed from Fig. 2, where the correlation factor  $\rho_{24}$  lies in the range  $-1 \leq \rho_{24} \leq -0.99$ . This indicates that a small acceleration acting on the spacecraft in the radial direction may seriously damage the precision of the cosine of declination. For example, for  $\psi = 90$  deg,  $\omega^{-1} \sigma_{\delta}$  jumps from 0.725 m without acceleration, to 6.027 m with acceleration. Care must therefore be exercised in determining  $\cos \delta$  when the spacecraft is subject to an acceleration.

If the radial acceleration  $L_r$  is so small that the term associated with it becomes the same order of magnitude as higher-order terms in the expansion of Eq. (7), which have been neglected as small, the preceding discussion does not apply. However, the original model in Hamilton-Melbourne's article, as well as their conclusion, remains valid.

For example, when

$$L_r = 10^{-8.5} \quad (\text{m/sec}^2) = 10^{-9.5} g$$

the deviation term  $\omega^{-2}\Delta\lambda_{\delta}$  of Eq. (30) becomes comparable to  $\omega^{-2}\bar{\sigma}_{\delta}^2$  which is  $(0.725 \text{ m})^2$ , according to Fig. 3

for  $\psi = 90$  deg. We may therefore safely conclude that the deviation term may be neglected when  $L_r$  is smaller than  $10^{-10} g$ , but cannot be ignored if the acceleration is larger than this value. Hence, the formulation developed in this article becomes necessary.

The concept of the observability which has been first introduced by Kalman (Ref. 1) is closely related to the preceding analysis. According to Kalman, the parameters are observable if the matrix  $J$  in Eq. (15) which is called Fisher's information matrix, is positive definite, or equivalently if all the elements of the observation matrix  $A$  are linearly independent of each other (Ref. 2).

Although  $\theta$  and  $\sin \theta$  are linearly independent of each other, and hence  $d$  and  $b$  are observable according to the above definitions, they are so closely correlated over  $-\psi \leq \theta \leq \psi$  and  $0 \text{ deg} \leq \psi \leq 90 \text{ deg}$ , as indicated by their correlation  $\rho_{24}$ , that they behave almost like unobservable (or undistinguishable) parameters. This accounts for the poor performance revealed by the estimators  $\widehat{b}$  and  $\widehat{d}$  (Fig. 3), especially for small  $\psi$ .

However, if some *a priori* information is available concerning these parameters, a simple analysis using Eq. (14) will indicate that the performance of these estimators can be significantly improved, and the curve for  $\omega^{-1}\sigma_{\delta}$  will approach that of  $\omega^{-1}\sigma_{\theta}$  in Fig. 3.

#### Definition of terms

$x, y, z$	rectangular coordinates of the spacecraft
$r_s$	distance of the station from the Earth's spin axis
$z_s$	distance of the station from the Earth's equatorial plane
$\omega$	Earth's rotation rate
$r, \dot{r}$	geocentric range and range-rate of the spacecraft
$\delta$	declination of the probe
$t$	time measured from the expected time that the probe will cross the meridian of the station
$t_0$	actual time of the meridian crossing
$\dot{x}_0, \dot{y}_0, \dot{z}_0$	speed of the spacecraft at time $t_0$
$L_x, L_y, L_z$	components of acceleration
$\theta - \theta_0 = \omega(t - t_0)$	

**C. Entry Capsule Orbit Determination**

**Accuracy, C. Scranage**

**1. Introduction**

Future planetary missions will employ an entry-lander capsule to collect data pertaining to the climatological, biological, and surface conditions existing on and near a planet. Advanced mission planning such as that required for *Voyager 1973* specifies that these data be transmitted by the DSN tracking system via two links: (1) the capsule-orbiting bus link (COL), and (2) the bus-Earth tracking station link (BEL). The presence of two vehicles in the vicinity of a planet presents the interesting possibility of using an on-board coherent two-way doppler system to determine range rate between the vehicles. Not only can this data type be used to determine the orbit of the capsule, but, as in the case where one spacecraft is an entry capsule, it can be used to estimate the atmospheric parameters of the planet. This observable should be highly accurate because of the large position and velocity parallax that is possible between the two moving spacecraft. This article presents some of the results obtained from a preliminary investigation on the effect of high frequency noise of two-way coherent doppler on the estimates of the orbit of the capsule and the atmospheric constants.

The material contained in this introductory article will encompass (1) a description of the computer programs and procedures, (2) a brief discussion regarding entry and impact statistics of the orbital parameters, and (3) a presentation of the estimated uncertainties on the atmospheric constants. To be discussed in future articles will be an estimate of the atmospheric winds (most of this work is completed), and an investigation of time-

varying drift in one-way doppler (this study is now underway).

The Martian atmosphere was simulated as piecewise continuous with a constant lapse rate. Since this is a feasibility investigation, a trajectory of simple geometry was chosen. This trajectory constrained both the bus and capsule to orbits lying in the equatorial plane of the planet; therefore, it was not possible to solve for latitude and flight path azimuth of the capsule with respect to Mars. These restrictions did not limit the generality of the method or the results.

Most significant of the results is that this new observable determined the stratosphere scale height, surface temperature, and stratosphere base temperature to a greater accuracy than was attained by the *Mariner IV* Mars occultation experiment.

**2. Mathematical Simulation**

*a. Trajectory program.* Two-body equations of motion employing three degrees of freedom were used to simulate the orbits of the bus and capsule. Both vehicles were represented as point masses in the program. Atmospheric drag was assumed to be the only nongravitational force acting on the capsule; the orbit of the bus was beyond the specified limits of the atmosphere. Normal trajectory conditions are given in Table 1. The bus-capsule geometry is illustrated in Fig. 4.

The atmosphere was assumed to be composed entirely of CO<sub>2</sub>. Since a temperature maximum does not occur for Mars (due to lack of ozone), the adiabatic lapse rate for temperature was applied immediately above the surface. The stratosphere is defined as the region extending

**Table 1. Nominal trajectory conditions (parameters referenced to coordinate system centered on Mars)**

Injection T <sub>0</sub>		Entry
Capsule	Bus	Capsule
$\tau_I$ , inertial longitude, 235 deg	$a$ , 6478 km	$R_I$ , altitude, 243.8 km
$\lambda_I$ , inertial latitude, 0 deg	$e$ , 0.2933004	$t_e$ , time of entry 3061 sec
$\gamma_{VI}$ , inertial flight-path angle, -21.381 deg	$i$ , 0	$\gamma_{VI}$ , inertial flight-path angle, -15.65 deg
$\beta_{VI}$ , flight-path azimuth, 90 deg	$\Omega$ , 270 deg	$V_I$ , inertial velocity, 4.014 km/sec
$R_I$ , inertial radial distance from geocenter, 7118.1966 km	$\omega$ , 90 deg	$\tau_I$ , inertial longitude, -33.61 deg
$V_I$ , inertial velocity, 2.1224864 km/sec	$T_p$ , -11681.825 sec	
GMM, gravitational constant of Mars, 42977.8 km <sup>3</sup> /sec <sup>2</sup>		

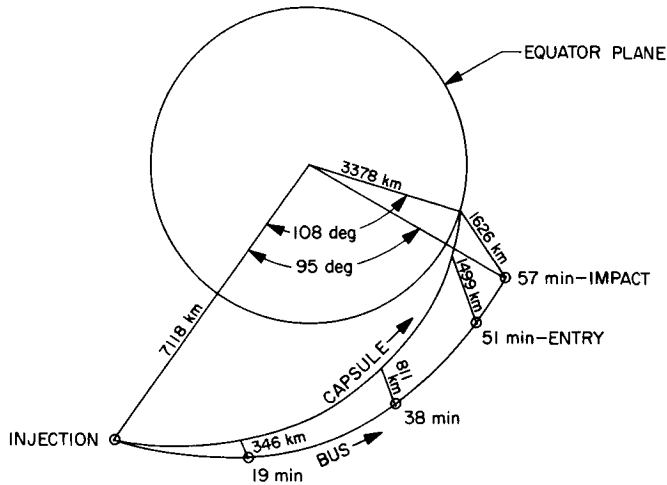


Fig. 4. Capsule-bus geometry

from tropopause to mesopause. Values of atmospheric density and temperature at the surface and at the base altitude of the stratosphere (namely,  $\rho_0$ ,  $T_0$ ,  $\rho_b$ ,  $T_b$ ) and the temperature gradient  $\Gamma = +\partial T/\partial(h - h_b)$  are given. The temperature and density as a function of altitude are computed as follows:

$$T = T_0 + \Gamma(h - h_{n-1}^*), \quad h_{n-1} \leq h < h_n^* \quad (1)$$

$$\rho = \rho_0 \left(\frac{T_0}{T}\right)^{(1+\Delta\Gamma_b)} \left(\frac{r_b}{r}\right)^{(2-\Delta\Gamma)} \times \exp \left[ -\Delta(t_0 - r_b\Gamma)r_b \left(1 - \frac{r_b}{r}\right) \right] \quad (2)$$

where

$$\Delta = \frac{g_0 R_0^2}{R'(T_b - \Gamma r_b)^2}$$

$$M = \frac{V_A}{(\gamma R'T)^{1/2}}$$

$R$  = universal gas constant

$R'$  = gas constant

$R_0$  = equatorial radius

$h$  = geometric altitude

$h^*$  = base altitude for atmospheric calculations

$h_b$  = base altitude of stratosphere

$$r = R_0 + h$$

$$r_b = R_0 + h_{n-1}^*$$

$V_A$  = velocity with respect to atmosphere

The scale height of the stratosphere  $H'_b$  is given as

$$H'_b = \frac{T_b R}{m_0 g_b} \quad (3)$$

where  $m_0$  is the molecular weight of the atmosphere at the surface and  $g_b$  is the acceleration of gravity at  $h_b$ .

If  $m_0 g_b$  is assumed constant for small changes in  $h$ ,

$$\delta H'_b = K \delta T_b \quad (4)$$

where

$$K = \frac{R}{m_0 g_b}$$

The ratio (standard deviation of  $H'_b$ )/ $H'_b$ , called coefficient variation, becomes

$$\frac{\sigma_{H'_b}}{H'_b} \cong \frac{\sigma_{T_b}}{T_b} \quad (5)$$

**b. Statistical program.** An IBM 1620 statistical program (MOPOS) employing Bayes' estimation theory was used to compute the uncertainties on the parameters at injection. The effects of data noise and *a priori* uncertainties were included in the statistical model. The covariance on the estimates of the parameter set  $X$  are contained in the matrix

$$\Gamma = [A^T W A + \tilde{\Gamma}_X^{-1}]^{-1} \quad (6)$$

where  $A$  is a matrix of partials of range rate with respect to  $X$ , and  $\Gamma_X$  is the *a priori* covariance matrix. In the  $W$  matrix the data is weighted as the inverse of the square of standard deviations on the observables. In this program it is assumed that the observations are not correlated with each other.

### 3. Procedures

**a. A priori uncertainties.** The sigmas on the estimated parameters are affected by inherent inaccuracies of the BEL which limit the uncertainties in the *a priori* injection conditions. The present S-band BEL configuration estimates position at the distance of Mars to within 10 km ( $3\sigma$ ).

For this study, the position of the bus is assumed to be known perfectly, and the 10 km uncertainty is assumed to be simulated as an error in the position of the capsule only. A retro-thrust of 500 m/sec and 1- $\sigma$  uncertainty in the pointing angle of  $\frac{2}{3}$  deg was used. The uncertainty of 1 km<sup>3</sup>/sec<sup>2</sup> in the gravitational constant of Mars was determined from *Mariner IV* data. From these data the 1- $\sigma$  *a priori* uncertainties of Table 2 were computed. *A priori* uncertainties assumed for the atmospheric constants are tabulated in Table 3.

**b. Data weighting.** The high frequency noise observed on  $\dot{\rho}$  in the BEL is generated by the hardware associated with the coherent two-way doppler. The level of this noise is directly related to oscillator instability (which varies with the type of oscillator) and oscillator temperature. Tracking data noise of 10<sup>-6</sup> km/sec (60-sec count

time) is considered a reasonable level for an Earth-based S-band system.

For this study it is assumed that the doppler is counted in the COL. Since it is highly improbable that capsule design will permit a rigid on-board environmental control to maintain oscillator stability, it is equally improbable that the doppler counted in the capsule would be of the quality associated with a high frequency noise level of 10<sup>-5</sup> km/sec. A knowledgeable guess of  $\sigma_{\dot{\rho}} = 10^{-3}$  km/sec is more likely.

**c. Statistics.** Finite difference partials to be used in the A matrix were computed by the trajectory program. The partials were generated to simulate observations taken at 1-min intervals before entry and at 2-sec intervals through the atmosphere. The injection statistics computed by the program were mapped to entry and impact altitudes. Elements of the mapping matrices were also computed by finite differences.

**Table 2. A priori uncertainties, 1 $\sigma$**

Capsule parameter	A priori values
Longitude	0.05 deg
Latitude	0.05 deg
Flight-path angle	0.1 deg
Azimuth	0.1 deg
Radial distance from planet	3.0 km
Velocity	0.002 km/sec
GM Mars	1.0 km <sup>3</sup> /sec <sup>2</sup>

#### 4. Discussion of Results

##### a. Orbital parameters

**Statistics at entry.** As mentioned previously, the geometry of the trajectory permits only four of the six orbital parameters to be estimated; namely, inertial longitude  $\tau_I$ , inertial flight path angle  $\gamma_{VI}$ , radial distance from the geocenter  $R_I$ , and inertial velocity  $V_I$ . Uncertainties in position were mapped into uncertainties in time of entry and time of impact. Impact statistics on all four parameters are given. In this article, the discussion of entry statistics

**Table 3. Coefficient of variation on atmospheric parameters**

Parameter	Nominal value	Coefficient of variation, %			Values obtained from <i>Mariner</i> occultation experiment	
		A priori	Data noise, km/sec		Nominal value	CV, %
			10 <sup>-2</sup>	10 <sup>-5</sup>		
$\gamma$	1.37	0.7	0.7	0.2		
$R', \frac{\text{km}^2}{\text{sec}^2 \cdot ^\circ\text{K}}$	$0.1889 \times 10^{-3}$	15	11	2		
$h_b, \text{km}$	18.6	5	5	0.06		
$T_0, ^\circ\text{K}$	200	12	11	2	180	11
$T_b, ^\circ\text{K}$	100	25	13	2		
$\rho_0, \frac{\text{kg}}{\text{km}^3}$	$0.132 \times 10^5$	70	27	0.3	$0.143 \times 10^5$	7
$H'_b, \text{km}$	5		13	2	8-10	20
$I', \text{k/km}$	-5.37					

is limited to the uncertainties in  $V_I$  and  $\gamma_{VI}$ , the two parameters which are of interest to the aerodynamicist engaged in the design of the capsule because they are necessary in computing the degree of atmospheric "braking."

Figs. 5 and 6 include plots of the standard deviations of  $V_I$  and  $\gamma_{VI}$  mapped to entry. An increase in time from injection corresponds to an increase in the number of observations at the rate of one observation per minute, which is used in the solution of the estimates. These plots indicate that uncertainties determined from tracking data (assuming no *a priori*) with high frequency noise in the

range  $10^{-5}$  to  $10^{-3}$  km/sec are not significantly improved when the combination of *a priori* and tracking data is used to determine the uncertainties. It is interesting to note that *a priori* plus tracking data with  $\sigma_{\dot{\rho}} = 10^{-2}$  km/sec produce statistics equal in magnitude to those obtained had only the *a priori* covariance matrix been mapped to entry.

*Impact statistics.* Table 4 is presented to illustrate the dependence of the uncertainties at impact on the quality of the observations, the quantity of the observations, and the number of parameters estimated. Noise on the data of  $10^{-5}$  and  $10^{-2}$  km/sec is given (statistics for  $10^{-4}$  and

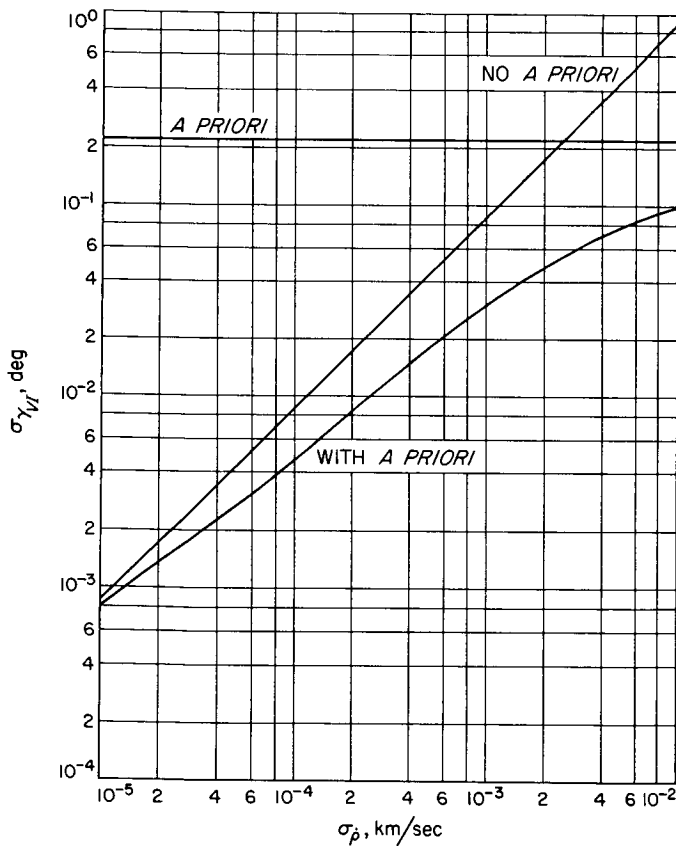


Fig. 5. Flight-path angle versus doppler noise

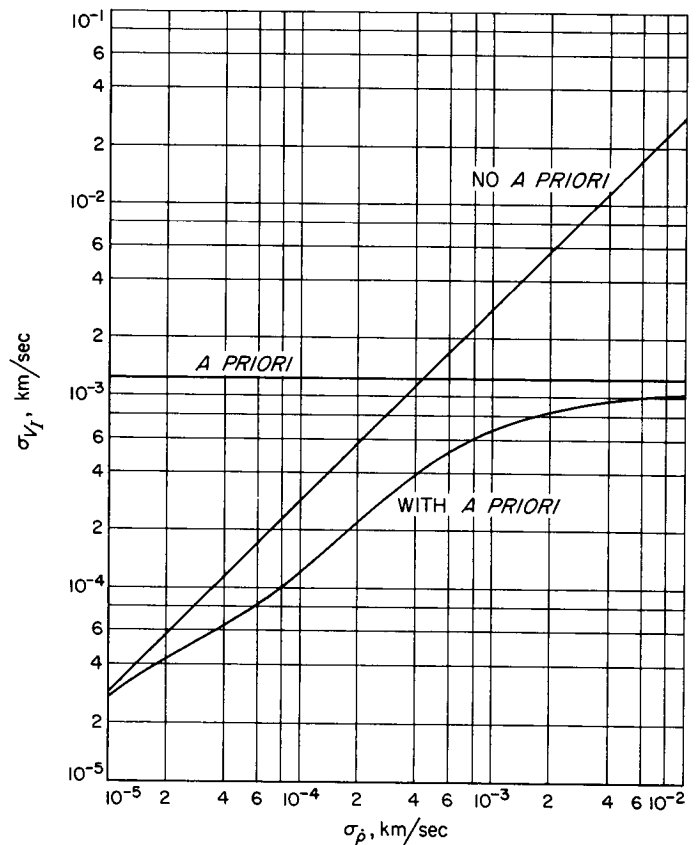


Fig. 6. Velocity versus doppler noise

Table 4. Impact statistics

Tracking data	$\sigma_{\dot{\rho}}$ km/sec	$\sigma_{\tau_I}$ , deg		$\sigma_{\gamma_{VI}}$ , deg		$\sigma_{T_{imp}}$ , sec		$\sigma_{V_I}$ , km/sec	
		5	12	5	12	5	12	5	12
Injection to impact	$10^{-2}$	$4.6 \times 10^{-2}$	1.7	$2.8 \times 10^{-2}$	$1.3 \times 10^{-1}$	$3.7 \times 10^{-2}$	$8.5 \times 10^2$	$4.5 \times 10^{-4}$	$1.8 \times 10^{-2}$
	$10^{-5}$	$2.0 \times 10^{-1}$	$4.4 \times 10^{-1}$	$3.5 \times 10^{-4}$	$8.8 \times 10^{-1}$	$1.1 \times 10^{-2}$	$1.8 \times 10^2$	$6.0 \times 10^{-6}$	$8.0 \times 10^{-1}$
Injection to entry	$10^{-2}$	$3.5 \times 10^{-1}$		$4.6 \times 10^{-1}$		$6.0 \times 10^{-1}$		$8.0 \times 10^{-3}$	
	$10^{-5}$	$3.3 \times 10^{-3}$		$6.0 \times 10^{-3}$		$1.3 \times 10^{-1}$		$1.0 \times 10^{-4}$	

$10^{-3}$  were obtained, but their inclusion here is not necessary for a general discussion). *A priori* uncertainties are included in the estimates. The numbers 5 and 12 indicate the number of parameters estimated: 5 = 4 orbital + gravitational constant of Mars (GMM); 12 = 4 orbital + GMM + angular velocity of planet  $\omega$  + 6 atmospheric constants.

The increase in standard deviations when the 12 parameters were estimated is due to (1) the correlation of the four orbital parameters with the eight constants, and (2) the inclusion of the *a priori* uncertainties in  $\lambda_l$  and  $\beta_{V_l}$  in the calculations. An increase in the noise on the tracking data from  $10^{-5}$  to  $10^{-2}$  km/sec results in an increase of 11 min in the uncertainty of impact time and corresponding increases in the uncertainties in  $\tau_l$ ,  $\gamma_{V_l}$ , and  $V_l$  of 1.3 deg, 0.13 deg and 0.017 km/sec, respectively.

**b. Atmospheric constants.** The coefficients of variation (CV) on the atmospheric parameters determined from a solution vector that included the 12 parameters mentioned above are given in Table 3. The values listed under the heading "Occultation Experiment" were determined from the values of  $T_0$ ,  $\rho_0$ , and  $H'_b$  obtained from the *Mariner IV* occultation experiment (Ref. 3). In this study,  $H'_b$  was not determined directly. The CV of  $H'_b$  was evaluated by equation using the value of the CV of  $T_b$  determined from the study. Judging from the accuracies attained from the *Mariner IV* mission, the *a priori* uncertainties appear to be conservative. As a result, the statistics on the atmospheric parameters can be considered realistic. The most significant fact obtained from this table is the degree of accuracy to which atmospheric constants can be estimated, even from a doppler system limited by high frequency noise to an inherent accuracy of  $10^{-2}$  km/sec. The uncertainties on the estimates of some atmospheric constants obtained from this study are an improvement over those obtained from the occultation experiment.

## 5. Conclusions

This investigation indicates that an on-board tracking system of two-way coherent doppler between an entry capsule and an orbiting bus is a highly reliable observable for determining the orbit of an entry capsule and estimating atmospheric parameters. The uncertainties on the estimates of the parameters do not appear to be as dependent on the inherent accuracy of the system as with an Earth-based system. High fidelity estimates can be obtained even when such a system is limited to inherent accuracy of  $10^{-2}$  km/sec due to high frequency noise. When this observable (with noise of  $10^{-2}$  km/sec)

was used in a simulated orbit determination accuracy study, estimates of the surface temperature, stratosphere base temperature, and stratosphere scale height were obtained which were comparable to those attained by the present methods of occultation.

The results presented here were computed using both statistical and mathematical models which were assumed to describe perfectly the atmosphere of Mars. Therefore, first-order changes in the model of the atmosphere would produce significant changes in the standard deviations.

## D. The JPL Matrix Operations Programming System, P. M. Muller

The interactions between various computer programs used in processing and analyzing DSN tracking data have been described in SPS 37-39, Vol. III, pp. 34-36. To illustrate how these programs fit together, systems for processing non-real-time data were reviewed. In addition, programs designed to establish the orbit determination accuracies obtainable with the DSIF tracking data were discussed. In this paper, one of the programs for processing and analyzing tracking data is considered.

## 1. Summary

The purpose of this article is to briefly describe an automatic FORTRAN IV programming system which accomplishes all matrix and vector operations plus a sophisticated input-output and housekeeping scheme. This system is programmed in FORTRAN IV in such a way that it should be readily convertible to any modern computing system with a FORTRAN IV compiler and at least 16,000 words of core. Minor changes are necessary for such conversion between machines, or between single and double precision (the latter is nominal). These changes are all made to a small number of subroutines, and thereafter the system will operate correctly and automatically under the new requirements. Dimensioning of arrays can range from 2 to 100, and is handled in one subroutine and the main (user's) program only. The system allows efficient use of programming, computer, and documentation time, but is comparatively inefficient with respect to the use of core storage. With the expenditure of about 3000 words in core, any subset of the system may be used, and this eases somewhat the core requirements for small jobs.

## 2. System Description

At this time, the JPL matrix operations programming (MOP) system consists of some 85 subroutines plus over two dozen additional named entry points. This is one of

two basic methods of programming a system that accomplishes the vector and matrix algebra operations and related manipulations. The other method, VECTRAN, to be found in the SHARE catalogue<sup>1</sup>, uses an addition to the FORTRAN compiler which accepts matrix algebra expressions in addition to FORTRAN. The MOP method requires the user to code the FORTRAN program in which the MOP subroutines are called by the user. The VECTRAN type of compiler system presumably allows the user to code a FORTRAN type of program which has expanded capability. In practice, this compiler method has not proved to be completely versatile or free from errors. On the other hand, the reliability of the subsystem routine has been established, since it can and has been exhaustively checked out by an automatic debugging package. For this reason, plus advantages in facility of updating and modifying the system as well as greater ease of learning and use, the subroutine system was chosen in preference to a compiler system.

### 3. Advantages and Costs

If the MOP were merely a series of library subroutines, it would still have the advantages of coherent naming, calling sequences, and philosophy. However, it surpasses that role, as it also includes a large amount of automatic control. The error messages, page registration, page headings, output labels, parameter (row-column) names, and many of the subroutine conditions are all automatically controlled regardless of which subroutines or which subsets of the system are used. The calling sequences involve, for the most part, only the operator names, and are free of the control indices always found in library routines. The naming of the subroutines is highly mnemonic and lends itself to rapid mastery. The cost for all of this is about 3000 words of core, which must be used and initialized before any or all of the system can be effectively run. The programmer need have only a fair understanding of FORTRAN IV to use the basic system. The more advanced FORTRAN programmer can quickly and conveniently use the system to accomplish virtually any and all matrix algebra manipulations, including input and output, and can do so most efficiently.

### 4. The System Operators

The possible operators for the system are listed as follows:

MATRIX: A square array (two-dimensional) of real numbers.

<sup>1</sup>IBM Systems Reference Library "SHARE" Program Listing and Dictionary of Titles.

TRIMAT: A square array matrix with the property of symmetry, stored in core as the triangular portion plus the diagonal (saves core).

DIAG: Diagonal matrix, stored as a vector, but handled in subroutines as though it were a diagonal matrix.

VECTOR: A vector of real numbers, either row or column vector, according to the subroutine called.

CONSTANT: A real number to be used in some matrix-algebra operation.

There is some provision for optimizing certain operations for nonsquare matrices stored in a square-matrix array (by augmenting with zeroes). Future development of the system will include the general rectangular matrix array (RECMAT). There are integer-vector arrays used for program control and for alphameric names and variables.

### 5. System Operations

The system includes several single-operator functions. They are inversion, correlation, normalization, duplication (of an operator), conversion (of an operator from one form to another; e.g., TRIMAT to MATRIX), input, output print, output punch, summation (of the elements), test for nonzero elements, zero to all elements, perform any FORTRAN library function upon all elements of an operator, and a large number of reordering or partitioning functions. The multiple-operator functions are addition, subtraction, and multiplication (including nonsquare matrices and DIAGs used in pre-post multiply situations). The subroutines SETUP and IOU (Input-Output-Utility) are required to initialize and preserve the system. Future development will include subroutines for RECMAT operations, eigenvalues and vectors, and name-list-format output of arrays.

### 6. Automatic Functions and Controls

The program has a common location for scratch vectors and scalars used by the subroutines themselves, which can occasionally be used in a program, but are normally left buried and untouched. There is a common location for a set of real-number indices (DPIX), fixed-point indices (INDEX), 10 word by 6 character page headings and labels (PHEADS), and 1 word, 6 character parameter or row and column names (PLABS). All system constants are stored in DPIX and referred to by subroutines as needed. The system control indices are in

INDEX. Both system-nominal and user-input page headings are addressable in PHEADS by the output routines, and are controlled by the user in blocks of 10 words from anywhere in the variable. The row and column names (which may be addressed independently) are taken from PLABS, beginning with any address chosen. These variables, once set by the user, conveniently allow labeling of all output, automatic registration to any form length, page numbering, diagnostic outputs for debugging or other uses, and alterations to the nominal mode of operation of many subroutines. The presence of these controls results in very simple calling sequences. For example, matrix inversion (Call IM(A)), matrix multiplication (Call MXM (A, B, C)) wherein C may replace either operator, and many others, all allowed without recourse to the EPSILON increments, convergence tests, variable dimensions, or others indices always present in library subroutines. All these variables, when needed, are found in the INDEX variables. There they can be initialized once and forgotten, or changed at will in the user's main program, depending upon the required program sophistication. All nominal system settings are made once in the subroutines SETUP and IOU, and thereafter will automatically serve the particular use in question.

## 7. Additional System Design Features

The MATRIX arrays are all dimensioned as vectors in the subroutines. In the main program, either single or double subscripting may be used for convenience. Therefore, the subroutines must compute their own addresses because of the presence of TRIMAT storage elements. MATRIX storage is by columns of length  $KD$ , with any matrix of that size or smaller stored by columns, each beginning at the top of the master columns and having length  $KORD$  where  $KORD \leq KD$ . TRIMAT storage is also by columns, with each successive master column beginning on the diagonal element instead of the first row. The matrix is dimensional with  $(KD + 1)$  columns of length  $KD$  each to permit overlay of two TRIMATs on one matrix. Thus, two TRIMATs of length  $(KD + 1) * KD / 2$  fit exactly (by EQUIVALENCE) on top of one MATRIX. This type of core allocation allows use of given core for either array type or for both sequentially. Most subroutines allow simultaneous use of these array types, even though overlaid at the time the answer is delivered. It is important to note that every operation was programmed to permit the maximum mathematically allowable overlay and identity of operators. Therefore, it is possible to do very large matrix allocations and still use the system efficiently. For example, in a typical case, the IBM 7094

computer, with 32,000 words of core, may be allocated as follows: 10,000 words for the monitor system software, 12,000 words for two MATRIX arrays overlaid with four TRIMAT arrays plus several vectors, and the remaining 10,000 words of core for MOP subroutines. It is possible to execute any of the MOP subroutines under this minimum configuration, and it is possible to load about one-third of the subroutines without overlay. A loading such as this permits the writing of a very large matrix program, with at least two MATRIX and four TRIMAT operators available for manipulation. This layout has been used for several NORMAL programs described here.

If care is exercised, the system can be run with matrices of several master dimensions all existing at the same time, even if overlaid. The subroutines, with the exception of duplication, are limited to having arrays of the same master dimension ( $KD$ ) in any one calling sequence. The duplication routines are used, for example, to remove a  $6 \times 6$  submatrix of a  $50 \times 50$  and thereafter operate upon it as a  $6 \times 6$  to save core. The two INDEX variables,  $KD$  and  $KORD$ , are used by the main program to keep the logic operating correctly.

It has been questioned why the system did not use the variable dimensions which FORTRAN IV permits, thereby eliminating the necessity of a master and sub-dimension. The answer is twofold: First, TRIMAT core allocation cannot be handled by convenient variable dimensions; second, the requirement that all such variable dimensions must appear in the calling sequences was not considered advantageous. In addition, single-subscripted subroutines run from slightly faster to a factor of 4 faster than double-subscripted subroutines, depending upon the computer system used. Therefore, the MOP system was compiled in such a fashion that the user sets  $KD$  and  $KORD$  to the proper values, where they remain until a further change is required.

## 8. Examples of MOP System Programs

The author has written ten distinct programs using the system, ranging from a matrix partitioning plus punchout, to the entire NORMAL and STATISTICS link, to the selenodesy programming system which will process the astrodynamical results from the *Lunar Orbiter* spacecraft data. The results have encouraged repeated use of the system for JPL Systems Analysis Section programs, and MOP is soon to be used as the basis for a very large and general NORMAL study program

## E. Theoretical Basis for the Double Precision Orbit Determination Program: V. Doppler and Range Observables, T. D. Moyer

(DPMMP). The system was completely revised into its present form, as documented here, in preparation for this effort.

As an example of a simple but representative NORMAL program, a description of the program MOPATA follows. It uses card or tape (standardized general format) input of vectors of partial derivatives relating some observables and some parameters at a number of points. Each such input is called an  $\mathbf{A}$  matrix, and has dimensions  $O$  by  $P$ , where  $O$  is the number of observables, and  $P$  is the number of parameters.  $\mathbf{W}$  is a weighting matrix of dimension  $O$  by  $O$ , which is the set of weights assigned to the observables. The program accumulates the product  $\mathbf{A}^T \mathbf{W} \mathbf{A}$  over the observations, the so-called normal, or  $\mathbf{J}$  matrix. Its inverse is the covariance matrix on the parameters estimated. Such a result may be "mapped" by application of a matrix containing the necessary coordinate transformation or translation partial derivatives  $\mathbf{U}$ , and computed by  $\mathbf{U} \mathbf{\Gamma} \mathbf{U}^T$  where  $\mathbf{\Gamma}$  is the covariance matrix in question. The answer covariance matrix has undergone the desired transformation.

In addition to these computations, the user may wish to begin the  $\mathbf{J}$  matrix accumulation at some point other than zero, and he may wish to study the effects of these various possible *a priori* conditions. The program MOPATA solves this general problem where any number of *a priori* conditions up to 50 may be given, any set of mapping matrix conditions given, and where any subset or subsets of the parameters to be estimated (to be actually inverted) are specified. We call this a parametric analysis program, since one run of the program results in answers involving all possible combinations of the user inputs, which are conveniently output for comparison. This program (to a dimension of  $50 \times 50$ ) was designed, programmed, checked out, and delivered by a single person in one week. It included useful page headings, labels, name list input of matrices, and many other features that are an integral part of the MOP system.

There is good evidence that this system reduces by a factor of 4 to 10 the time required to do the same job by other standard means, even assuming that library sub-routines are available. The automatic features of the MOP system are convenient and useful, and allow very sophisticated output (for example) with minimal programming effort. In addition, the resulting programs are easily and reliably modified to suit short-term user needs. The MOPATA program, as well as several others, will be documented in future Space Programs Summaries.

### 1. Introduction

This article is the fifth of a series presenting the theoretical basis for the double precision orbit determination program (DPODP), and gives the formulation for computing two-way doppler and round-trip range in light seconds. These are the primary observables taken by the tracking stations of the DSN.

An electromagnetic signal is transmitted continuously from a tracking station on Earth, received and retransmitted by the probe, and continuously received by the same tracking station on Earth. The frequency of the received signal differs from that of the transmitted signal because of the doppler shift. Two-way doppler is the average value of the frequency shift (transmitted minus received) over a period of time  $T_c$  (called the count time). An observable is generally recorded every  $T_c$  seconds. The round-trip time of the signal in seconds of station time is the two-leg ranging observable.

The formulation for computing two-way doppler and two-leg range is given in Sections 2 and 3, respectively. The formulation requires the solution to the light time problem (SPS 37-41, Vol. III, pp. 31-38); namely, the heliocentric position, velocity, acceleration, and jerk vectors of each participant evaluated at its epoch of participation. The rectangular components of each vector are referred to the mean Earth equator and equinox of 1950.0. The participants are the tracking station at the reception time  $t_3$  (midpoint of the count interval  $T_c$  for doppler), the probe at its reception/transmission time  $t_2$ , and the tracking station at its transmission time  $t_1$ .

The effect of atmospheric refraction on two-way doppler and two-leg range is accounted for by an additive correction, which is not considered here.

### 2. Computation of Two-Way Doppler

*a. General expression.* An expression is given here for two-way doppler as a function of the doppler frequency shift and its second-time derivative, both evaluated at the midpoint of the count interval  $T_c$ . Expressions for computing these quantities will be derived in the following two sections.

The output from the electronic equipment at the tracking station is a signal whose frequency in cycles per

second of station time is  $f$ :

$$f = C_3 \left[ f_q(t_3) - f_q(t_1) \left( \frac{f_R}{f_T} \right) \right] + C_4 \quad (1)$$

where

$f_q(t_3), f_q(t_1)$  = transmitter reference oscillator frequency at reception time  $t_3$  and transmission time  $t_1$ , respectively (generally identical unless  $f_q$  has been changed between  $t_1$  and  $t_3$ )

$f_R/f_T$  = ratio of received to transmitted frequency for unity frequency multiplication at spacecraft

$$C_3 = \begin{cases} 30 \left( \frac{96}{89} \right), & \text{L-band} \\ 96 \left( \frac{240}{221} \right), & \text{S-band} \end{cases}$$

$$C_4 = \begin{cases} 10^5, & \text{L-band} \\ 10^6, & \text{S-band} \end{cases}$$

The transmitted frequency is 30 or 96 times the reference oscillator frequency for L- or S-band operation. The spacecraft transponder multiplies the frequency of the received signal by 96/89 or 240/221 for L- or S-band operation before retransmitting. The expression for  $f$  may be written as

$$f = C_3 f_q(t_1) \left( 1 - \frac{f_R}{f_T} \right) + f_{bias} \quad (2)$$

where

$$f_{bias} = C_3 [f_q(t_3) - f_q(t_1)] + C_4 \quad (3)$$

Note that the first term of  $f_{bias}$  normally is zero.

The signal with frequency  $f$  is fed into an electronic counter whose register is incremented by 1 each time the amplitude of the signal changes from minus to plus.  $N$  cycles are counted during the count time  $T_c$ . The two-way doppler observable which the data editing program passes on to the orbit determination program (ODP) is:

$$\bar{f} = \frac{N}{T_c} - f_{bias} \quad (4)$$

The observed two-way doppler is the average of  $f - f_{bias}$  over the count time  $T_c$ :

$$\bar{f} = \frac{1}{T_c} \int_{t_3 - \frac{1}{2}T_c}^{t_3 + \frac{1}{2}T_c} (f - f_{bias}) dt \quad (5)$$

where  $t_3$  = epoch at midpoint of count interval, station time.

The expression for  $f - f_{bias}$  may be expanded in a Taylor series with coefficients evaluated at  $t_3$ . Eq. (5) may then be integrated term by term. The odd derivatives vanish, and the fourth and higher derivatives are ignored. The resulting expression for  $\bar{f}$  is

$$\bar{f} = C_3 f_q(t_1) \left[ \left( 1 - \frac{f_R}{f_T} \right) + \frac{T_c^2}{24} \left( 1 - \frac{f_R}{f_T} \right)'' \right] \quad (6)$$

where  $[1 - (f_R/f_T)]$  and its second derivative with respect to station time are evaluated at the midpoint of the count interval. The first term which has been truncated in Eq. (6) is  $(1/1920) (T_c^4) [1 - (f_R/f_T)]^{(iv)}$ . In order to minimize to truncation error in Eq. (6), the count time  $T_c$  must be limited to approximately 1 sec for a near Earth spacecraft, and to approximately 1000 sec when the spacecraft is in heliocentric cruise.

*b. Derivation of expression for  $[1 - (f_R/f_T)]$ .* The ratio of received to transmitted frequency, where the frequencies are measured relative to the atomic frequency standard at the tracking station, is

$$\frac{f_R}{f_T} = \frac{dn}{d\tau_3} \cdot \frac{d\tau_1}{dn} = \frac{d\tau_1}{d\tau_3} \quad (7)$$

where

$dn$  = infinitesimal number of cycles transmitted and received

$d\tau_1$  = infinitesimal period (of proper time  $\tau$ ) of transmission of  $dn$  cycles from tracking station at time  $t_1$

$d\tau_3$  = infinitesimal period (of proper time  $\tau$ ) of reception of  $dn$  cycles at tracking station at time  $t_3$

Note that proper time is time obtained from an atomic clock fixed in the observer's frame of reference. Eq. (7) may be written as

$$\frac{f_R}{f_T} = \frac{(d\tau_1/dt_1)}{(d\tau_3/dt_3)} \left( \frac{dt_1}{dt_2} \right) \left( \frac{dt_2}{dt_3} \right) \quad (8)$$

where

$dt_1, dt_2, dt_3$  = differentials of transmission time  $t_1$ , probe time  $t_2$ , and reception time  $t_3$  (ephemeris time).

The ratios  $dt_1/dt_2$  and  $dt_2/dt_3$  will be obtained by differentiating the light time equations for the up and down legs of the light path. An interval of proper time is given by

$$d\tau = \frac{ds}{c} \quad (9)$$

where

$c$  = speed of light

$ds$  = invariant interval between two near events in four dimensional space-time

The interval  $ds$  of transmission (or reception) of  $dn$  cycles is related to the transmission time  $dt$  (ephemeris time) and to the differentials of the heliocentric space coordinates of the station during  $dt$ . Using de Sitter's  $n$ -body line element (Ref. 4) (which reduces to the Schwarzschild isotropic line element when the mass of the Sun only is considered), and retaining terms of order  $(1/c)^0$ ,

$$ds^2 = c^2 \left( 1 - \frac{2\phi}{c^2} \right) dt^2 - dx^2 - dy^2 - dz^2 \quad (10)$$

where

$x, y, z$  = rectangular components of station position in heliocentric nonrotating frame of reference

$t$  = uniform coordinate time in heliocentric frame of reference (ephemeris time)

$\phi$  = Newtonian potential at station given approximately by

$$\phi = + \sum_j \frac{\mu_j}{r_j} \quad (11)$$

$\mu_j$  = gravitational constant of body  $j$ ,  $\text{km}^3/\text{sec}^2$

$r_j$  = distance from station to body  $j$ , km

Substituting Eq. (9) into Eq. (10) and using

$$\dot{s}^2 = \left( \frac{dx}{dt} \right)^2 + \left( \frac{dy}{dt} \right)^2 + \left( \frac{dz}{dt} \right)^2 \quad (12)$$

where

$\dot{s}$  = heliocentric velocity of tracking station

gives the ratio of proper time to ephemeris time for transmission or reception:

$$\frac{d\tau_i}{dt_i} = \left[ 1 - \frac{2\phi_i}{c^2} - \left( \frac{\dot{s}_i}{c} \right)^2 \right]^{1/2}, \quad i = 1, 3 \quad (13)$$

From SPS 37-41, Vol. III, pp. 31-38, the light time equation for the up leg of the light path is given by

$$t_2 - t_1 = \frac{r_{12}}{c} + \frac{2\mu}{c^3} \ln \left[ \frac{\tan \frac{1}{2} \beta_1}{\tan \frac{1}{2} \beta_2} \right] \quad (14)$$

where

$\mu$  = gravitational constant of Sun,  $\text{km}^3/\text{sec}^2$

$$r_{12} = || \mathbf{r}_{12} || \quad (15)$$

$$\mathbf{r}_{12} = \mathbf{r}_2 - \mathbf{r}_1, \quad \mathbf{r} \rightarrow \dot{\mathbf{r}}, \ddot{\mathbf{r}}, \ddot{\mathbf{r}} \quad (16)$$

$\mathbf{r}_i, \dot{\mathbf{r}}_i, \ddot{\mathbf{r}}_i, \ddot{\mathbf{r}}_i$  = heliocentric position, velocity, acceleration, and jerk of participant  $i$  at its epoch of participation  $t_i$ , with rectangular components referred to the mean Earth equator and equinox of 1950.0. The index  $i = 1$  (tracking station at transmission time  $t_1$ ), 2 (probe at  $t_2$ ), or 3 (tracking station at reception time  $t_3$ ).

$$\cos \beta_1 = \frac{\mathbf{r}_1}{r_1} \cdot \frac{\mathbf{r}_{12}}{r_{12}}, \quad 0 \leq \beta_1 \leq 180^\circ \quad (17)$$

$$\cos \beta_2 = \frac{\mathbf{r}_2}{r_2} \cdot \frac{\mathbf{r}_{12}}{r_{12}}, \quad 0 \leq \beta_2 < 180^\circ \quad (18)$$

Formula (14) is indeterminate for light traveling radially to or from the Sun. For this case,

$$t_2 - t_1 = \frac{r_{12}}{c} + \frac{2\mu}{c^3} \ln \frac{r_l}{r_s} \quad (19)$$

where  $r_l$  and  $r_s$  are the larger and smaller values of  $r_1$  and  $r_2$ . Eqs. (14) through (19) apply for the down leg of the light path when the subscript 1 is replaced by 2 and

2 is replaced by 3. Differentiating Eq. (14) with respect to  $t_2$  and collecting  $dt_1/dt_2$  terms gives

$$\frac{dt_1}{dt_2} = \frac{1 - \frac{1}{c} \frac{\partial r_{12}}{\partial t_2} + \frac{2\mu}{c^3} \left( \frac{1}{\sin \beta_2} \frac{\partial \beta_2}{\partial t_2} - \frac{1}{\sin \beta_1} \frac{\partial \beta_1}{\partial t_2} \right)}{1 + \frac{1}{c} \frac{\partial r_{12}}{\partial t_1} - \frac{2\mu}{c^3} \left( \frac{1}{\sin \beta_2} \frac{\partial \beta_2}{\partial t_1} - \frac{1}{\sin \beta_1} \frac{\partial \beta_1}{\partial t_1} \right)} \quad (20)$$

Ignoring terms of order higher than  $(1/c)^3$ , this can be written as

$$\frac{dt_1}{dt_2} = \frac{1 - \frac{1}{c} \frac{\partial r_{12}}{\partial t_2} + \frac{2\mu}{c^3} \epsilon_{12}}{1 + \frac{1}{c} \frac{\partial r_{12}}{\partial t_1}} \quad (21)$$

where

$$\epsilon_{12} = \frac{1}{\sin \beta_2} \left( \frac{\partial \beta_2}{\partial t_2} + \frac{\partial \beta_2}{\partial t_1} \right) - \frac{1}{\sin \beta_1} \left( \frac{\partial \beta_1}{\partial t_2} + \frac{\partial \beta_1}{\partial t_1} \right) \quad (22)$$

The derivatives of  $r_2$ ,  $r_1$ , and  $r_{12}$  with respect to  $t_2$  and  $t_1$  are

$$\frac{dr_2}{dt_2} = \frac{\mathbf{r}_2 \cdot \dot{\mathbf{r}}_2}{r_2} \quad (23)$$

$$\frac{dr_1}{dt_1} = \frac{\mathbf{r}_1 \cdot \dot{\mathbf{r}}_1}{r_1} \quad (24)$$

$$\frac{\partial r_{12}}{\partial t_2} = \frac{\mathbf{r}_{12} \cdot \dot{\mathbf{r}}_2}{r_{12}} \quad (25)$$

$$\frac{\partial r_{12}}{\partial t_1} = - \frac{\mathbf{r}_{12} \cdot \dot{\mathbf{r}}_1}{r_{12}} \quad (26)$$

Differentiating Eq. (18) with respect to  $t_2$  and  $t_1$  and adding gives

$$- \sin \beta_2 \left( \frac{\partial \beta_2}{\partial t_2} + \frac{\partial \beta_2}{\partial t_1} \right) = \frac{\mathbf{r}_{12} \cdot \dot{\mathbf{r}}_2 + \mathbf{r}_2 \cdot \dot{\mathbf{r}}_{12}}{r_2 r_{12}} - \cos \beta_2 \left( \frac{\mathbf{r}_{12} \cdot \dot{\mathbf{r}}_{12}}{r_{12}^2} + \frac{\mathbf{r}_2 \cdot \dot{\mathbf{r}}_2}{r_2^2} \right) \quad (27)$$

Differentiating Eq. (17) with respect to  $t_2$  and  $t_1$  and adding gives

$$- \sin \beta_1 \left( \frac{\partial \beta_1}{\partial t_1} + \frac{\partial \beta_1}{\partial t_2} \right) = \frac{\mathbf{r}_{12} \cdot \dot{\mathbf{r}}_1 + \mathbf{r}_1 \cdot \dot{\mathbf{r}}_{12}}{r_1 r_{12}} - \cos \beta_1 \left( \frac{\mathbf{r}_{12} \cdot \dot{\mathbf{r}}_{12}}{r_{12}^2} + \frac{\mathbf{r}_1 \cdot \dot{\mathbf{r}}_1}{r_1^2} \right) \quad (28)$$

Substituting Eqs. (25) and (26) into Eq. (21) gives

$$\frac{dt_1}{dt_2} = \frac{1 - \frac{1}{c} \frac{\mathbf{r}_{12}}{r_{12}} \cdot \dot{\mathbf{r}}_2 + \frac{2\mu}{c^3} \epsilon_{12}}{1 - \frac{1}{c} \frac{\mathbf{r}_{12}}{r_{12}} \cdot \dot{\mathbf{r}}_1}, \quad \begin{array}{l} 1 \rightarrow 2 \\ 2 \rightarrow 3 \end{array} \quad (29)$$

Substituting Eqs. (27) and (28) into Eq. (22) gives

$$\epsilon_{12} = \frac{1}{\sin^2 \beta_1} \left[ \frac{\mathbf{r}_{12} \cdot \dot{\mathbf{r}}_1 + \mathbf{r}_1 \cdot \dot{\mathbf{r}}_{12}}{r_1 r_{12}} - \cos \beta_1 \left( \frac{\mathbf{r}_{12} \cdot \dot{\mathbf{r}}_{12}}{r_{12}^2} + \frac{\mathbf{r}_1 \cdot \dot{\mathbf{r}}_1}{r_1^2} \right) \right], \quad \beta_1, \beta_2 \neq 0^\circ, 180^\circ$$

$$- \frac{1}{\sin^2 \beta_2} \left[ \frac{\mathbf{r}_{12} \cdot \dot{\mathbf{r}}_2 + \mathbf{r}_2 \cdot \dot{\mathbf{r}}_{12}}{r_2 r_{12}} - \cos \beta_2 \left( \frac{\mathbf{r}_{12} \cdot \dot{\mathbf{r}}_{12}}{r_{12}^2} + \frac{\mathbf{r}_2 \cdot \dot{\mathbf{r}}_2}{r_2^2} \right) \right], \quad \begin{array}{l} 1 \rightarrow 2 \\ 2 \rightarrow 3 \end{array} \quad (30)$$

Differentiating Eq. (19) with respect to  $t_2$  and collecting  $dt_1/dt_2$  terms gives Eq. (29) where  $\epsilon_{12}$  is given by

$$\epsilon_{12} = \frac{\dot{r}_s}{r_s} - \frac{\dot{r}_l}{r_l}, \quad \beta_1, \beta_2 = 0^\circ \text{ or } 180^\circ \quad \begin{array}{l} 1 \rightarrow 2 \\ 2 \rightarrow 3 \end{array} \quad (31)$$

where

$$\dot{r}_s = \frac{\mathbf{r}_s \cdot \dot{\mathbf{r}}_s}{r_s} \quad r_s \rightarrow r_i \quad (32)$$

Substituting Eq. (13) with  $i = 1, 3$  and  $dt_1/dt_2$  and  $dt_2/dt_3$  from Eq. (29) into Eq. (8) gives

$$\frac{f_R}{f_T} = \frac{\left[ 1 - \frac{2\phi_1}{c^2} - \left( \frac{\dot{s}_1}{c} \right)^2 \right]^{1/2}}{\left[ 1 - \frac{2\phi_3}{c^2} - \left( \frac{\dot{s}_3}{c} \right)^2 \right]^{1/2}} \cdot \frac{1 - \frac{1}{c} \frac{\mathbf{r}_{12}}{r_{12}} \cdot \dot{\mathbf{r}}_2 + \frac{2\mu}{c^3} \epsilon_{12}}{1 - \frac{1}{c} \frac{\mathbf{r}_{12}}{r_{12}} \cdot \dot{\mathbf{r}}_1} \cdot \frac{1 - \frac{1}{c} \frac{\mathbf{r}_{23}}{r_{23}} \cdot \dot{\mathbf{r}}_3 + \frac{2\mu}{c^3} \epsilon_{23}}{1 - \frac{1}{c} \frac{\mathbf{r}_{23}}{r_{23}} \cdot \dot{\mathbf{r}}_2} \quad (33)$$

Expanding Eq. (33) in powers of  $1/c$  and retaining terms to order  $(1/c)^3$  gives

$$\begin{aligned} \left(1 - \frac{f_R}{f_T}\right) &= \frac{1}{c} (\dot{r}_{12} + \dot{r}_{23}) + \frac{1}{c^2} \left[ \dot{p}_{12}\dot{r}_{12} + \dot{p}_{23}\dot{r}_{23} - \dot{r}_{12}\dot{r}_{23} + \phi_1 - \phi_3 + \frac{1}{2} (\dot{s}_1^2 - \dot{s}_3^2) \right] \\ &+ \frac{1}{c^3} \left\{ \dot{p}_{12}^2 \dot{r}_{12} + \dot{p}_{23}^2 \dot{r}_{23} - \dot{r}_{12}\dot{r}_{23} (\dot{p}_{12} + \dot{p}_{23}) - (\dot{r}_{12} + \dot{r}_{23}) \left[ \phi_1 - \phi_3 + \frac{1}{2} (\dot{s}_1^2 - \dot{s}_3^2) \right] \right. \\ &\left. - 2\mu (\varepsilon_{12} + \varepsilon_{23}) \right\} \end{aligned} \quad (34)$$

where  $\varepsilon_{12}$  and  $\varepsilon_{23}$  are given by Eqs. (30) or (31) and

$$\dot{r}_{12} = \frac{\mathbf{r}_{12}}{r_{12}} \cdot \dot{\mathbf{r}}_{12} \quad (35)$$

$$\dot{r}_{23} = \frac{\mathbf{r}_{23}}{r_{23}} \cdot \dot{\mathbf{r}}_{23} \quad (36)$$

$$\dot{p}_{12} = \frac{\mathbf{r}_{12}}{r_{12}} \cdot \dot{\mathbf{r}}_1 \quad (37)$$

$$\dot{p}_{23} = \frac{\mathbf{r}_{23}}{r_{23}} \cdot \dot{\mathbf{r}}_2 \quad (38)$$

$$\dot{s}_i^2 = \dot{\mathbf{r}}_i \cdot \dot{\mathbf{r}}_i \quad (39)$$

The Newtonian potential at the tracking station is computed from

$$\phi_i = \frac{\mu_s}{\|\mathbf{r}_i\|} + \frac{\mu_E}{\text{station radius}}, \quad i = 1, 3 \quad (40)$$

where

$\mu_s, \mu_E =$  gravitational constants for Sun and Earth,  $\text{km}^3/\text{sec}^2$

*c. Derivation of expression for  $[1 - (f_R/f_T)]''$ .* The second derivative of the doppler frequency shift with respect to station time, evaluated at the midpoint of the count interval, is approximated by the second derivative with respect to ephemeris time.

$$\begin{aligned} \left(1 - \frac{f_R}{f_T}\right)'' &\equiv \frac{d^2}{dt_3^2(\text{ST})} \left(1 - \frac{f_R}{f_T}\right) \\ &\approx \frac{d^2}{dt_3^2(\text{ET})} \left(1 - \frac{f_R}{f_T}\right) \end{aligned} \quad (41)$$

The error in this approximation is less than the accuracy of the doppler formulation; namely,  $10^{-5}$  m/sec. For purposes

of differentiation, the expression for  $[1 - (f_R/f_T)]$  is taken to be

$$\left(1 - \frac{f_R}{f_T}\right) \approx \frac{1}{c} (\dot{r}_{12} + \dot{r}_{23}) + \frac{1}{c^2} (\dot{p}_{12}\dot{r}_{12} + \dot{p}_{23}\dot{r}_{23} - \dot{r}_{12}\dot{r}_{23}) \quad (42)$$

The second derivatives of the omitted  $1/c^2$  potential  $\phi$  and velocity  $\dot{s}^2$  terms and the  $1/c^3$  terms contribute less than  $10^{-5}$  m/sec to observed average range rate. Differentiating Eq. (42) twice with respect to  $t_3$  (ET) gives

$$\begin{aligned} \left(1 - \frac{f_R}{f_T}\right)'' &= \frac{1}{c} \frac{d^2 \dot{r}_{12}}{dt_3^2} \left[1 + \frac{1}{c} (\dot{p}_{12} - \dot{r}_{23})\right] \\ &+ \frac{1}{c} \frac{d^2 \dot{r}_{23}}{dt_3^2} \left[1 + \frac{1}{c} (\dot{p}_{23} - \dot{r}_{12})\right] \\ &+ \frac{1}{c^2} \frac{d^2 \dot{p}_{12}}{dt_3^2} \dot{r}_{12} + \frac{1}{c^2} \frac{d^2 \dot{p}_{23}}{dt_3^2} \dot{r}_{23} \\ &+ \frac{2}{c^2} \left( \frac{d\dot{r}_{12}}{dt_3} \frac{d\dot{p}_{12}}{dt_3} \right. \\ &\left. + \frac{d\dot{r}_{23}}{dt_3} \frac{d\dot{p}_{23}}{dt_3} - \frac{d\dot{r}_{12}}{dt_3} \frac{d\dot{r}_{23}}{dt_3} \right) \end{aligned} \quad (43)$$

The quantities  $\dot{r}_{12}$ ,  $\dot{r}_{23}$ ,  $\dot{p}_{12}$ , and  $\dot{p}_{23}$  are functions of the state vectors at times  $t_3$ ,  $t_2$ , and  $t_1$ . In order to differentiate these quantities with respect to  $t_3$ (ET), the following derivatives (obtained by differentiating the light time equations) are used:

$$\frac{dt_2(\text{ET})}{dt_3(\text{ET})} = 1 - \frac{\dot{r}_{23}}{c} \quad (44)$$

$$\frac{dt_1(\text{ET})}{dt_3(\text{ET})} = 1 - \frac{1}{c} (\dot{r}_{12} + \dot{r}_{23}) \quad (45)$$

In carrying out the derivatives in Eq. (43), the following quantities appear:

$$\dot{r}_{12} \equiv \frac{\partial r_{12}}{\partial t_2} + \frac{\partial r_{12}}{\partial t_1} = \frac{\mathbf{r}_{12}}{r_{12}} \cdot \dot{\mathbf{r}}_{12}, \quad \begin{array}{l} 1 \rightarrow 2 \\ 2 \rightarrow 3 \end{array} \quad (46)$$

$$\ddot{r}_{12} \equiv \frac{\partial \dot{r}_{12}}{\partial t_2} + \frac{\partial \dot{r}_{12}}{\partial t_1} = \frac{\mathbf{r}_{12} \cdot \ddot{\mathbf{r}}_{12} + \dot{\mathbf{r}}_{12} \cdot \dot{\mathbf{r}}_{12} - \dot{r}_{12}^2}{r_{12}}, \quad \begin{array}{l} 1 \rightarrow 2 \\ 2 \rightarrow 3 \end{array} \quad (47)$$

$$\dddot{r}_{12} \equiv \frac{\partial \ddot{r}_{12}}{\partial t_2} + \frac{\partial \ddot{r}_{12}}{\partial t_1} = \frac{\mathbf{r}_{12} \cdot \dddot{\mathbf{r}}_{12} + 3\dot{\mathbf{r}}_{12} \cdot \ddot{\mathbf{r}}_{12} - 3\dot{r}_{12}\ddot{r}_{12}}{r_{12}}, \quad \begin{array}{l} 1 \rightarrow 2 \\ 2 \rightarrow 3 \end{array} \quad (48)$$

$$\dot{p}_{12} \equiv \frac{\mathbf{r}_{12}}{r_{12}} \cdot \dot{\mathbf{r}}_1, \quad \begin{array}{l} 1 \rightarrow 2 \\ 2 \rightarrow 3 \end{array} \quad (49)$$

$$\ddot{p}_{12} \equiv \frac{\partial \dot{p}_{12}}{\partial t_2} + \frac{\partial \dot{p}_{12}}{\partial t_1} = \frac{\mathbf{r}_{12} \cdot \ddot{\mathbf{r}}_1 + \dot{\mathbf{r}}_1 \cdot \dot{\mathbf{r}}_{12} - \dot{p}_{12}\dot{r}_{12}}{r_{12}}, \quad \begin{array}{l} 1 \rightarrow 2 \\ 2 \rightarrow 3 \end{array} \quad (50)$$

$$\dddot{p}_{12} \equiv \frac{\partial \ddot{p}_{12}}{\partial t_2} + \frac{\partial \ddot{p}_{12}}{\partial t_1} = \frac{\mathbf{r}_{12} \cdot \dddot{\mathbf{r}}_1 + 2\dot{\mathbf{r}}_{12} \cdot \ddot{\mathbf{r}}_1 + \dot{\mathbf{r}}_1 \cdot \ddot{\mathbf{r}}_{12} - 2\dot{r}_{12}\ddot{p}_{12} - \dot{p}_{12}\ddot{r}_{12}}{r_{12}}, \quad \begin{array}{l} 1 \rightarrow 2 \\ 2 \rightarrow 3 \end{array} \quad (51)$$

Also, the following relations are used:

$$\frac{\partial r_{12}}{\partial t_1} = -\dot{p}_{12}, \quad \begin{array}{l} 1 \rightarrow 2 \\ 2 \rightarrow 3 \end{array} \quad (52)$$

$$\frac{\partial \dot{r}_{12}}{\partial t_1} = -\ddot{p}_{12}, \quad \begin{array}{l} 1 \rightarrow 2 \\ 2 \rightarrow 3 \end{array} \quad (53)$$

$$\frac{\partial \ddot{r}_{12}}{\partial t_1} = -\dddot{p}_{12}, \quad \begin{array}{l} 1 \rightarrow 2 \\ 2 \rightarrow 3 \end{array} \quad (54)$$

Differentiating  $\dot{r}_{12}$  and  $\dot{r}_{23}$  twice with respect to  $t_3$  using the definitions in Eqs. (47) and (48), and using Eqs. (44), (45), (53), and (54), gives

$$\frac{d^2 \dot{r}_{12}}{dt_3^2} = \ddot{r}_{12} + \frac{1}{c} (2\ddot{p}_{12}\dot{r}_{12} - 2\ddot{r}_{12}\dot{r}_{23} + \dot{r}_{12}\dot{p}_{12} - \dot{r}_{12}\dot{r}_{23}) \quad (55)$$

$$\frac{d^2 \dot{r}_{23}}{dt_3^2} = \ddot{r}_{23} + \frac{1}{c} (2\ddot{p}_{23}\dot{r}_{23} + \dot{r}_{23}\dot{p}_{23}) \quad (56)$$

For the derivatives in the  $1/c^2$  terms of Eq. (43), the derivatives (44) and (45) are taken to be unity, and

$$\frac{d\dot{r}_{12}}{dt_3} \approx \dot{r}_{12}, \quad \begin{array}{l} 1 \rightarrow 2 \\ 2 \rightarrow 3 \end{array} \quad (57)$$

$$\frac{d\dot{p}_{12}}{dt_3} \approx \dot{p}_{12}, \quad \begin{array}{l} 1 \rightarrow 2 \\ 2 \rightarrow 3 \end{array} \quad (58)$$

$$\frac{d^2 \dot{p}_{12}}{dt_3^2} \approx \ddot{p}_{12}, \quad \begin{array}{l} 1 \rightarrow 2 \\ 2 \rightarrow 3 \end{array} \quad (59)$$

Substituting Eqs. (55) through (59) into Eq. 43 gives

$$\begin{aligned} \left(1 - \frac{f_R}{f_T}\right)'' &= \frac{1}{c} \ddot{r}_{12} \left[1 + \frac{1}{c} (\dot{p}_{12} - 3\dot{r}_{23})\right] + \frac{1}{c} \ddot{r}_{23} \left[1 + \frac{1}{c} (\dot{p}_{23} - \dot{r}_{12})\right] \\ &+ \frac{3}{c^2} (\ddot{p}_{12}\dot{r}_{12} + \ddot{p}_{23}\dot{r}_{23}) + \frac{3}{c^2} (\dot{r}_{12}\ddot{p}_{12} + \dot{r}_{23}\ddot{p}_{23} - \dot{r}_{12}\dot{r}_{23}) \end{aligned} \quad (60)$$

where the quantities used are computed from Eqs. (46) through (51).

### 3. Computation of Two-Leg Range

The two-leg range observable is computed from

$$\rho = t_3 - t_1 + \frac{R_c}{10^3 c} \quad (61)$$

where

$t_3$  = reception time of signal at tracking station, station time

$t_1$  = transmission time of signal at tracking station, station time

$R_c$  = solve for ranging bias, meters (specified by time block for each station)

$c$  = speed of light, km/sec

The light time problem is solved in ephemeris time, and the round-trip time is converted to station time using the time transformations given in SPS 37-39, Vol. III, pp. 36-38.

N67 15907

### F. Pioneer Project Support, D. W. Curkendall, J. E. Ball, and J. F. Gallagher

#### 1. Introduction, D. W. Curkendall

The *Pioneer* program consists of a series of spacecraft designed to gather scientific information concerning the deep-space environment in the region near the ecliptic plane and at a distance from the Sun varying from 0.8 to 1.2 AU. The DSN is committed to track the *Pioneer* spacecraft, obtain engineering and scientific telemetry, determine the orbit of each probe, and provide facilities to the Project within the SFOF and the DSIF for the conduct of the mission and reduction of data. Specific items under this task will be selected during each report period for further discussion.

In this issue, the successful launch and early orbit determination results of *Pioneer VII* are reported.

### 2. Pioneer VII Postlaunch Activities, J. E. Ball and J. F. Gallagher

*Pioneer VII* was launched on August 17, 1966, 15<sup>h</sup> 20<sup>m</sup> 17.<sup>s</sup>286 GMT. A nominal parking orbit was achieved and four AFETR tracking stations observed the coast phase. Transfer orbit injection occurred 25<sup>m</sup>21<sup>s</sup> from launch, and the heliocentric orbit was nominal. Three deep space stations (DSS 51, DSS 42, and DSS 11) tracked the spacecraft. After approximately 36 hr in orbit, the spacecraft went through a Type-II orientation maneuver to properly align its spin axis with respect to the ecliptic plane for communications purposes. Table 5 summarizes the results of the preorientation and the postorientation orbit computations.

The primary objective of the *Pioneer VII* mission was to send the spacecraft through the Earth's magnetosphere at a distance of several hundred Earth radii from the geocenter. On September 22, 1966, at about 12<sup>h</sup> GMT, the *Pioneer VII* passed through syzygy with the Sun and Earth. The celestial longitude of the Earth at this time was 359.0383 deg, and the celestial longitude and latitude of the spacecraft were 359.04009 and 0.0555337 deg, respectively. The distance of the spacecraft from the Earth was 5,146,000 km, or about 807 Earth radii. The distance of the probe above the ecliptic plane was 150,504 km, or about 23.6 Earth radii. This syzygy position satisfied the scientific needs of the magnetosphere experiment.

The best orbit determination to date (October 26, 1966, postorientation 3) shows that there will be an occultation of the *Pioneer VII* by the Moon on January 20, 1967, at about 5<sup>h</sup>30<sup>m</sup> GMT. The right ascension and declination of the Moon at this time are about 42.5 and 16.5 deg, respectively. This occultation will be visible to the Stanford antenna where the lunar occultation experiment will be carried out. A gas leak was recently discovered on the *Pioneer VII*. A cursory analysis of the perturbing effect of the gas leak on the trajectory of the spacecraft reveals that although its existence will considerably degrade the prediction of the probe position on January 20, an occultation should still occur.

Table 5. Summary of orbits

Items		Preorientation	Pastorientation 3
Injection conditions	Epoch	15 <sup>h</sup> 45 <sup>m</sup> 38 <sup>s</sup> .626 (66/08/17)	13 <sup>h</sup> 00 <sup>m</sup> 00 <sup>s</sup> .0 (66/08/19)
	x, km	-6317.0086	405987.78
	y, km	-1695.2897	-23031.865
	z, km	-1689.9426	-9448.2170
	$\dot{x}$ , km/sec	3.4921793	1.8976926
	$\dot{y}$ , km/sec	7.7612659	0.0266948
	$\dot{z}$ , km/sec	-6.8737429	0.0774747
Parameter statistics	$\sigma_x$ , km	0.063235	2.417940
	$\sigma_y$ , km	0.344739	3.065523
	$\sigma_z$ , km	0.315043	6.504306
	$\sigma_{\dot{x}}$ , km/sec	0.000533	0.000003
	$\sigma_{\dot{y}}$ , km/sec	0.000345	0.000005
	$\sigma_{\dot{z}}$ , km/sec	0.000811	0.000014
Number of data points in orbit	DSS 51 (Johannesburg) CC3	504	3050
	DSS 42 (Tidbinbilla) CC3	224	3860
	DSS 11 (Pioneer) CC3	183	2640
Geocentric conic <sup>a</sup> of pericenter passage	Epoch	15 <sup>h</sup> 44 <sup>m</sup> 53 <sup>s</sup> .9 (66/08/17)	15 <sup>h</sup> 48 <sup>m</sup> 08 <sup>s</sup> .5 (66/08/17)
	SMA	-238677.91	-241866.63
	ECC	1.0282655	1.0277063
	C3	1.6700384	1.6480210
	RCA	6746.3487	6701.2334
	TA	4.1508808	160.14153
	INC	41.924554	42.170418
	LAN	358.30088	358.22291
	APF	197.83713	197.87560
Heliocentric conic <sup>a</sup> of pericenter passage	Epoch	17 <sup>h</sup> 10 <sup>m</sup> 53 <sup>s</sup> .8 (66/05/28)	00 <sup>h</sup> 00 <sup>m</sup> 12 <sup>s</sup> .5 (66/07/18)
	SMA	118127660.0	162858590.
	ECC	0.42326200	0.07928469
	C3	-1123.4804	-814.90397
	RCA	68128711.0	149946400.
	TA	148.19573	32.939440
	INC	7.8074922	0.11492503
	LAN	144.28250	326.02138
	APF	31.805896	327.21709
<sup>a</sup> Osculating elements of injection epoch. Definition of terms: SMA—semi-major axis ECC—eccentricity C3—energy CC3—two-way doppler data RCA—radius of closest approach TA—true anomaly INC—inclination LAN—longitude of ascending node APF—argument of perifocus			

## References

1. Kalman, R. D., *New Methods and Results in Linear Prediction and Estimation Theory*, Technical Report 16-1, Research Institute for Advanced Study, Baltimore, Maryland, 1961.
2. Kreindler, E., and Sarachik, P. E., "On the Concept of Controllability and Observability of Linear Systems," *IEEE Transactions on Automatic Control*, Vol. AC-9, No. 2, pp. 129-136, April 1964.
3. Kliore, A., et al., "Occultation Experiment: Results of the First Direct Measurement of Mars Atmosphere and Ionosphere," *Science*, Vol. 149, pp. 1243-1248, September 10, 1965.
4. Moyer, T. D., *Relativistic Equations of Motion*, p. 50, Master's Thesis, University of California, Los Angeles, Calif., June 1965.

### III. Communications Research and Development

**N67 15908**

#### **A. Frequency Generation and Control: Atomic Hydrogen Frequency Standard, W. H. Higa**

The dual channel traveling wave maser (TWM) has been designed and is presently being integrated into a closed-cycle refrigerator (CCR). Each section will conform to the following specifications:

$$f = 1420 \text{ GHz}$$

$$3\text{-db BW} = 10 \text{ MHz}$$

$$\text{Gain} \cong 25 \text{ db}$$

$$\text{Noise temperature} \leq 10^\circ\text{K}$$

A simple test configuration will be used to evaluate the stability characteristics of the TWM. Subsequently, the atomic hydrogen masers will provide separate signals for the two channels of the dual TWM. Well known signal processing techniques (Ref. 1) may then be used to derive the power spectra of the maser oscillators.

Fig. 1 shows the dual channel maser installed in the CCR (SPS 37-39, Vol. III, pp. 79-81). Fig. 2 shows the top view of the assembly.

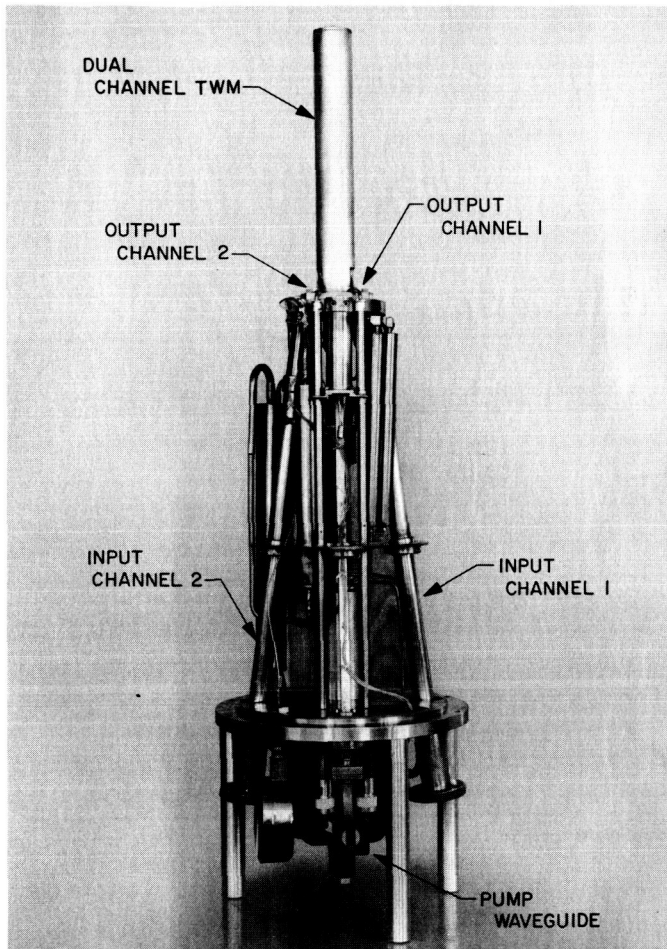


Fig. 1. Dual channel maser installed in the closed cycle refrigerator

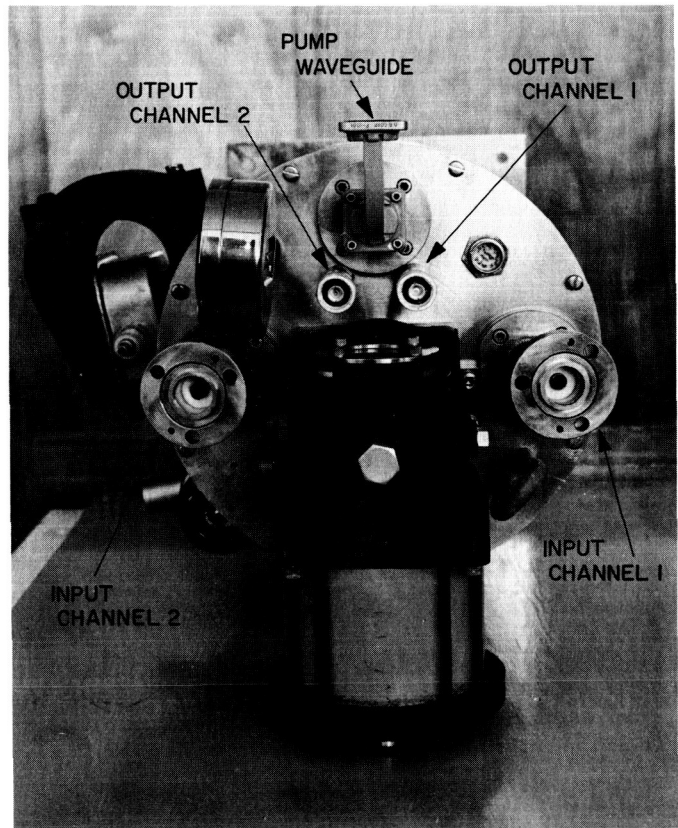


Fig. 2. Top view of the maser/CCR assembly

**B. Improved RF Calibration Techniques for Daily System Noise Temperature Measurements,**  
*C. T. Stelzried*

The daily noise temperature calibration technique used at the Mars and Venus stations has been discussed in detail (SPS 37-39, Vol. III, p. 96). Noise temperature calibrations are made by switching the maser input between the antenna and an ambient load with a waveguide switch. The principal advantage of this technique is the long term stability and reliability of the ambient waveguide termination. This technique depends on a previous calibration of the maser/follow-up amplifier effective noise temperature. A 1°K error in this calibration results in approximately a 0.1°K error in the system temperature calibration. A refinement has been made consisting of a follow-up temperature contribution measurement for each calibration with a maser off-on Y-factor measurement.

The follow-up contribution defined at the maser input measured by turning the maser off with the input connected to the ambient termination is given to good approximation by

$$T_F = \frac{T_M + T_0}{Y_{00} - 1} \quad (1)$$

where

$T_M$  = maser noise temperature defined at the maser input, °K

$T_0$  = ambient termination temperature, °K

$Y_{00}$  = receiver output noise ratio between maser on and off

The receiver noise temperature defined at the maser input is then given by

$$T_R = T_M + T_F \quad (2)$$

A revised calibration sheet, 1620 computer program (modified by Lois Busch), and sample print-out are shown in Figs. 3-5.

RECEIVING SYSTEM NOISE TEMPERATURE DAILY CALIBRATION

Operators Name N . M . K A K U  
Mission M A R I N E R I V  
Weather C L E A R  
Frequency 2 . 2 9 7 . 6

---

Station No. 1 4 . Month 0 9 . Day 0 8 . Year 1 9 6 6 .  
Day No. 2 5 1 . Calibration Time: hour (GMT) 0 1 . Minutes 0 8 .  
(to be recorded half way thru Y-factor measurements)

Antenna Coordinates: AZ 2 7 6 . 6 2 EL 8 7 . 0 5

Comments \_\_\_\_\_

---

Signal Generator on Freq. 2 Detector Bias, 4 mv 2 Filter, Normal 2  
Pre-Cal 1 Post Cal 2 Other 1  
Maser Gain GM (db) 4 0 . 0 Maser Gain GM (dB) if reset or peaked  
(Do not adjust on Post Cal or if gain down less than 1 dB from nominal)

Reflectometer Measurements: Ambient Load 3 9 . 8 db  
Antenna 3 1 . 4 db

Maser on-off, Yoo (db) 2 5 . 6 (Switch to ambient load. Measure before noise. Y-factors on pre-calibration and after noise. Y-factors on post-calibration.)

Ambient Temperature, T<sub>02</sub> 2 5 . 1 1 deg C. (To be recorded half way through Y-factor measurements)

Maser Temperature, T<sub>M</sub> 7 . 2 deg K.

Noise Temperature (ALL Readings, dB)

AMB

A<sub>0</sub>(I) 2 0 . 1 9 2 0 . 1 7 2 0 . 1 8 2 0 . 1 8 2 0 . 1 8

ANT

A<sub>A</sub>(I) 9 . 8 4 9 . 8 3 9 . 8 4 9 . 8 3 9 . 8 3

Fig. 3. Daily system temperature calibration data sheet

```

C   RECEIVING SYSTEM NOISE TEMPERATURE DAILY CALIBRATIONS
C   PROGRAM FOR DATA ONLY (NO PLOTS) CTS/20B
   DIMENSION AADB(5),AADB(5),YOADB(5),YOA(5),TSA(5),OP(20),MISS(20),
1  WTHR(20),FREQ(7),COMM(40),ND(50),TP(50),TS(50),TM(50),F(50),
2  AM(50),AN(50),G(50),D(50)
   COMMON M
   M=0
   IF(SENSE SWITCH 9)40,40
40  READ 1,OP,MISS,WTHR,FREQ
   READ 2,NO,MON,IDAY,IYR,NDAY,IHR,MIN,AZ,EL,COMM
   READ 3,ISIG,IDET,IFIL,IPRE,IPOST,IOTHER,GM,GMR,AMBL,ANT,YOO,TO2,
1  TEM
   DAY=NDAY
   HR=IHR
   DMIN=MIN
   M=M+1
   J=M
   TOK=TO2+273.16
   TF=(TOK+TEM)/(10.**(YOO/10.)-1.0)
   TR=TEM+TF
   READ 4,(AADB(I),I=1,5)
   READ 4,(AADB(I),I=1,5)
39  PRINT 71
   PRINT 72,NO
   PRINT 73,OP
   PRINT 74,MON,IDAY,IYR,NDAY
   PRINT 75,IHR,MIN
   PRINT 76,FREQ
   IF(IOTHER)34,34,36
34  PRINT 93,IPRE,IPOST
   GO TO 38
36  PRINT 92,IPRE,IPOST,IOTHER
38  PRINT 77,WTHR
   IF(AZ)51,52,51
51  IF(EL)53,54,53
52  IF(FL)56,55,56
54  PRINT 23,AZ
   GO TO 58
55  PRINT 25
   GO TO 58
56  PRINT 24,EL
   GO TO 58
53  PRINT 21,AZ,EL
58  IF(GMR)42,42,41
41  PRINT 18,GM,GMR
   PRINT 22,AMBL,ANT
   GO TO 43
42  PRINT 19,GM
   PRINT 22,AMBL,ANT
43  PRINT 82,YOO
   PRINT 83,TO2
   PRINT 84,TEM
   PRINT 85,COMM
   PRINT 11
44  DO 50 I=1,5
   N=I-1
   IF(AADB(I))50,70,50

```

Fig. 4. Daily system temperature IBM 1620 computer program

```

50 CONTINUE
N=5
70 PETO2=0.1
PETR=1.0
A=0.003
B=0.00354
EN=N
SUM=0.0
SYOA=0.0
DO 100 I=1,N
YOADB(I)=AODB(I)-AADB(I)
YOA(I)=10.** (YOADB(I)/10.)
TSA(I)=(TOK+TR)/YOA(I)
SUM=TSA(I)+SUM
SYOA=YOA(I)+SYOA
99 PRINT 12,AODB(I),AADB(I),YOADB(I),TSA(I)
100 CONTINUE
STSA=SUM/EN
YOAS=SYOA/EN
DBYOA=LOGF(YOAS)*4.3429448
STT=0.0
DO 200 I=1,N
STT=(STSA-TSA(I))**2+STT
200 CONTINUE
PEMI=0.6745*SQRTF(STT/(EN-1.))
PEM=PEMI/SQRTF(EN)
235 PEYQ=YOAS**2*(A**2+B**2*DBYOA**2)*.053018981
PETSQ=PEM**2+(PETO2**2+PETR**2)*(1./YOAS)**2+PEYQ*((TOK+TR)**2/
1 YOAS**4)
PETSQ=SQRTF(PETSQ)
TPS=STSA+PETSQ
TPM=STSA-PETSQ
238 PRINT 86,STSA
PRINT 87,TR
PRINT 88,TF
PRINT 89,PEMI
PRINT 90,PEM
PRINT 91,PETSQ
245 IF(SENSE SWITCH 9)255,40
255 CONTINUE
1 FORMAT(2X,3(20A1),7A1)
2 FORMAT(I4,1X I2,2X I2,1X I4,1X I3,2(1X I2),1XF6.2,F5.2,40A1)
3 FORMAT(6I1, F4.1,F6.1,F7.1,2F5.1,F6.2,F9.1)
4 FORMAT(5F10.0)
71 FORMAT(1H,8X40HSYSTEM NOISE TEMPERATURE PROGRAM CTS/20B)
72 FORMAT(1H ,8X11HSTATION NO.I3)
73 FORMAT(1H ,8X9HOPERATOR 20A1)
74 FORMAT(1H ,8X5HDATE I2,1H/I2,1H/I4,10H DAY,NU.I4)
75 FORMAT(1H ,8X9HTIME(GMT)I3,6H HOURS I3,8H MINUTES)
76 FORMAT(1H ,8X14HFREQUENCY(MC) 7A1)
77 FORMAT(1H ,8X7HWEATHER,1X20A1)
21 FORMAT(1H ,8X24HANTENNA COORD.(DEG.) AZ.F7.2,2X3HEL.F6.2)
25 FORMAT(1H ,8X24HANTENNA COORD.(DEG.) AZ.,9X,3HEL.)
24 FORMAT(1H ,8X24HANTENNA COORD.(DEG.) AZ.,9X,3HEL.F6.2)
23 FORMAT(1H ,8X24HANTENNA COORD.(DEG.) AZ.F7.2,2X3HEL.)
18 FORMAT(1H ,8X14HMASER GAIN(DB),F6.2/1H ,8X21HPEAKED MASER GAIN(DB)
1 F5.1)

```

Fig. 4 (contd)

```

19 FORMAT(1H ,8X14HMASER GAIN(DB),F6.2/1H ,8X23HPEAKED MASER GAIN(DB)
1 )
-----
22 FORMAT(1H ,8X23HREFL.MEAS.(DB) AMB.LOAD,F5.1,2X4HANT.F5.1)
-----
82 FORMAT(1H ,8X16HMASER ON-OFF(DB),F5.1)
-----
83 FORMAT(1H ,8X20HAMBIENT TEMP.(DEG.C),F6.2)
-----
84 FORMAT(1H ,8X18HMASER TEMP.(DEG.K),F5.1)
-----
85 FORMAT(1H ,8X9HCOMMENTS 3X30A1,/1H ,8X10A1)
-----
11 FORMAT(1H0,8X5HA0(I),4X5HAA(I),4X6HY0A(I),4X6HTSA(I))
-----
12 FORMAT(7XF7.2,2F9.2,F10.2)
-----
86 FORMAT(1H0,8X19HSYSTEM TEMP.(DEG.K),F9.2)
-----
87 FORMAT(1H ,8X21HRECEIVER TEMP.(DEG.K),F7.2)
-----
88 FORMAT(1H ,8X22HFOLLOW-UP CONT.(DEG.K),F6.2)
-----
89 FORMAT(1H ,8X39HPROB.ERROR SYSTEM TEMP.IND.MEAS.(DEG.K),F7.2)
-----
90 FORMAT(1H ,8X35HPROB.ERROR SYSTEM TEMP.MEAS.(DEG.K),F11.2)
-----
91 FORMAT(1H ,8X38HPROB.ERROR SYSTEM TEMP.OVERALL (DEG.K),F8.2)
-----
92 FORMAT(1H ,8X25HTEST CONDITIONS PRE-CAL,I2,2X8HPOST-CAL,I2,5X
1 I2HNON-STANDARD,I2)
-----
93 FORMAT(1H ,8X25HTEST CONDITIONS PRE-CAL,I2,2X8HPOST-CAL,I2,5X
1 I2HNON-STANDARD)
-----
END

```

Fig. 4 (contd)

```

SYSTEM NOISE TEMPERATURE PROGRAM CTS/20B
STATION NO. 14
OPERATOR N M KAKU
-----
DATE 9/ 8/1966 DAY NO. 251
TIME(GMT) 1 HOURS 8 MINUTES
-----
FREQUENCY(MC) 2297.6
TEST CONDITIONS PRE-CAL 1 POST-CAL 2 NON-STANDARD 1
WEATHER CLEAR
ANTENNA COORD.(DEG.) AZ. 276.62 EL. 87.05
-----
MASER GAIN(DB) 40.00
PEAKED MASER GAIN(DB)
-----
REFL.MEAS.(DB) AMB.LOAD 39.8 ANT. 31.4
MASER ON-OFF(DB) 25.6
-----
AMBIENT TEMP.(DEG.C) 25.11
MASER TEMP.(DEG.K) 7.2
-----
COMMENTS

```

AD(I)	AA(I)	YOA(I)	TSA(I)
20.19	9.84	10.35	28.25
20.17	9.83	10.34	28.32
20.18	9.84	10.34	28.32
20.18	9.83	10.35	28.25
20.18	9.83	10.35	28.25

```

-----
SYSTEM TEMP.(DEG.K) 28.28
RECEIVER TEMP.(DEG.K) 8.04
-----
FOLLOW-UP CONT.(DEG.K) .84
PROB.ERROR SYSTEM TEMP.IND.MEAS.(DEG.K) .02
PROB.ERROR SYSTEM TEMP.MEAS.(DEG.K) .01
PROB.ERROR SYSTEM TEMP.OVERALL (DEG.K) .25

```

Fig. 5. Daily system temperature print-out

Day No., 1966	$T_{S_1}$ , °K	$T_{F_1}$ , °K	$G_{M_1}$ , db	Zenith	Test conditions			Clear weather	Frequency, MHz	Comments
					Pretest	Posttest	Other			
203	21.3	0.34	41.2	X		X		X	2388	
203	21.0	0.37	45.1	↓	X			↓		
204	22.3	0.32	43.8	↓	↓			↓		
205	22.41	5.02	43.3	?	↓			↓		
206	22.4	5.23?	45.2	X	↓			X		
210	22.5	0.7	40.2	↓	↓			X		
210	21.3	0.6	39.8	↓	↓		X	No		
211	25.0	0.7	40.4	↓	X			↓		
213	21.0	0.5	40.4	↓	?	?		↓		
214	22.1	0.4	39.1	↓	↓			↓		
261	22.2	0.3	38.0	↓	↓			X		
264	22.2	0.4	39.9	↓	↓		X	X		
262	21.7	0.3	37.0	↓	↓			No		
263	21.1	↓	41.0	↓	↓			X		
265	22.4	↓	38.4	↓	↓		X	↓		
266	22.9	↓	40.8	↓	X			↓		
266	22.0	↓	37.2	↓	↓		X	↓		
267	22.6	↓	38.2	↓	↓		↓	↓		
268	22.0	↓	37.6	↓	↓		↓	↓		
269	21.1	↓	40.1	↓	X		↓	↓		
270	21.9	↓	40.5	↓	↓		X	No		
271	21.0	↓	40.0	↓	X			X		
272	20.9	0.4	40.9	↓	↓		X	No		
272	34.9	3.0	34.5	↓	X			↓		Rain on horn
273	21.6	0.3	40.1	↓	↓	?		↓		
274	21.3	0.4	40.1	↓	X			↓		
275	21.7	0.3	37.6	↓	↓			X		
276	22.0	0.4	37.4	No	↓			↓		
276	24.7	0.7	38.9	X	↓		X	↓		
277	21.7	0.4	37.5	↓	↓			↓		
277	27.1	0.6	40.0	↓	↓			↓	2297.6	Mariner IV
279	20.8	0.4	37.3	↓	X			No	2388	
279	24.5	0.1	48.8	↓	X			X	2297.6	Mariner IV
279	24.8	0.1	52.0	↓	↓	X		↓	2297.6	Mariner IV
280	21.6	0.5	37.5	↓	↓		X	↓	2388	
282	21.3	0.3	37.6	↓	↓		↓	↓		
283	22.3	0.6	39.2	↓	↓		↓	↓		
284	24.5	0.1	51.5	↓	X		↓	↓	2297.6	Mariner IV
286	21.9	0.5	39.7	↓	X		↓	↓	2388	
287	22.8	↓	39.8	↓	↓		X	↓		
288	22.6	↓	39.7	↓	↓		↓	↓		
290	23.7	↓	39.0	↓	↓		↓	↓		
291	24.2	0.1	53.0	↓	↓		↓	↓	2297.6	
292	23.0	0.5	39.0	↓	↓		↓	↓	2388	
293	23.8	↓	39.0	↓	X		↓	↓		
293	23.1	↓	39.0	↓	↓		X	↓		
294	22.1	0.4	39.7	↓	↓		X	↓		
295	20.3	0.5	39.7	↓	X		↓	↓		
296	21.9	0.4	39.1	↓	↓		X	↓		
297	22.1	0.5	39.0	↓	↓		X	↓		

Fig. 6. Tabulated results of the Venus station daily noise temperature calibrations

The principal results of the daily noise temperature calibration for the period July 12 (day No. 193) to October 24 (day No. 297), 1966 are tabulated in Figs. 6 and 7 for the Venus and Mars stations.<sup>1</sup> It is suspected that the

high followup contributions on days 194 and 234 at the Mars station and days 205 and 206 at the Venus station were due to making a maser on-off Y-factor measurement with the antenna switched to the antenna instead of the ambient termination, as required for proper data reduction. The average system noise temperatures and reported maser gains for this period are tabulated in Table 1.

<sup>1</sup>These data were taken by the Venus station personnel.

Day No., 1966	$T_{S,}$ °K	$T_{F,}$ °K	$G_{M,}$ db	Zenith	Test conditions		Clear weather	Frequency, MHz	Comments
					Pretest	Posttest			
193	26.1	0.4	40.1	No		X	X	2338	
194	27.2	0.4	40.0	X		X			
194	29.0	4.1	40.0	X	X				
201	45.5	0.6	40.0	No	X				
202	26.2	0.7	40.4	X		X			
204	24.7	0.7	42.5		X		No		
208	27.1	0.6	41.0	?	X		No		
209	27.3		40.5	X		X	X		
209	28.8		40.5		X		X		
210	45.3		40.2			X			
213	46.3	0.9	38.6		X		No		RF spur
232	28.3	0.6	40.4		X		X	2297.6	RF spur
233	27.9	0.6	41.3			X			
234	30.7	24?	39.8		X				
234	28.3	0.6	41.3						
244	29.5	0.8	40.4						
244	28.8	0.9	40.1			X			
250	34.4	0.9	40.0	No	X				
250	28.1	0.8	40.0	X	X				
251	28.3	0.8	40.0			X			
252	26.5	0.9	38.6		X		No		
253	24.8	0.9	38.3			X			
270	26.5	0.8	39.0		X			2388	
271	27.6	0.8	38.6			X			RF spur
278	43.5	0.4	39.0			X			
283	31.7	0.8	40.6	No	X			2297.6	
283	68.0	0.7	40.8	X		X			
284	36.3	0.8	40.5	No	X				2-way duplex mode
285	34.5	0.7	40.5	X		X			2-way duplex mode
285	33.8	0.9	38.8	X	X		X	2388	
285	29.7	0.8	40.4	No				2297.6	
285	34.7	0.7	39.5	No				2388	
286	28.6	0.8	40.0	X				2297.6	
286	27.7	0.7	38.8	X		X		2388	
287	37.7	0.9	38.6	?	X			2388	
287	28.9	0.8	40.2	X		X	No	2297.6	
288	28.2	0.8	39.6			X	X	2388	
290	28.9	0.7	40.0		X			2297.6	
291	31.9	0.8	39.4		X				
291	28.6	0.9	39.6			X			
291	35.0	0.9	40.0			X			2-way duplex mode
292	27.7	0.8	39.9		X				
293	27.5	0.8	39.9		X		No		
294	27.9	0.9	40.0			X	No		
294	25.5	0.7	39.3		X		X	2388	
294	26.2	1.0	37.6			X	No	2388	

Fig. 7. Tabulated results of the Mars station daily noise temperature calibrations

**Table 1. Summary of the system noise temperature and maser gain averages**

Station	Frequency, MHz	System temperature, °K	Maser gain, db
Venus	2297.6	25.0 ± 1.2 (1-σ variation) 5 data points	51.3 ± 1.8 (1-σ variation) 4 data points (excluding day No. 277)
	2388	22.2 ± 0.9 (1-σ variation) 32 data points	39.5 ± 2.0 (1-σ variation) 45 data points
Mars	2297.6	28.9 ± 1.2 (1-σ variation) 13 data points	40.2 ± 0.5 (1-σ variation) 23 data points
	2388	28.1 ± 2.4 (1-σ variation) 9 data points	39.5 ± 1.1 (1-σ variation) 23 data points

This is the first reported use of the Venus station R & D cone at 2297.6 MHz, since installation of the modified maser with broadband frequency tuning capability (SPS 37-40, Vol. III, p. 90). The system temperature averages were computed using only data which were acquired as follows:

- (1) Antenna at zenith.
- (2) Clear weather.
- (3) No RF spur in receiver pass band.
- (4) Not in two way duplex mode.

The maser gain averages were computed using all data points, except as noted. The maser gain was optimized (usually with magnet current or pump frequency), if the gain had dropped more than 1 db below nominal during this period. The maser gain variations have some effect on system temperature variations. The next series of measurements will be made to optimize the maser gain during each precalibration.

**N67 15910**

**C. Improved RF Calibration Techniques: Weekly Noise Temperature Calibrations, T. Y. Otoshi**

**1. Calibration Technique**

By the method described for daily calibrations in subsection B of this section, it was shown that system temperature can be determined to good accuracy using a single thermal noise standard (ambient load), even though the receiver temperature might be known only approximately.

To obtain an absolute calibration of receiver temperature, however, or to separate system temperature into its

antenna and receiver temperature components, it is required that a second thermal noise standard (cryogenic load) be used. The Y-factor calibration technique involving two thermal noise standards was discussed in detail in SPS 37-39, Vol. III, pp. 86-91, and also in SPS 37-40, Vol. IV, pp. 202-209.

For reference purposes the block diagram for the basic measurement system is shown in Fig. 8. The double-primed symbols indicate temperatures defined at the maser input reference flange; all single-primed symbols refer to temperatures defined at the antenna output reference flange. The double- and single-primed temperatures are related by the dissipative losses of the interconnecting transmission lines.

The notations used are defined as follows (the primes have been dropped for generality):

$T_c$  = cryogenic load effective temperature, °K

$T_R$  = receiver temperature, °K (includes the contribution of the receiver system following the maser)

$T_A$  = antenna temperature, °K

$T_{02}$  = physical and effective noise temperature of the ambient load, °K. (The physical temperatures of the transmission lines are also assumed to be at temperature  $T_{02}$ )

$T_E$  = excess noise temperature of the gas tube injected into the maser amplifier, °K

For this measurement system, the expression for system temperature, as defined at the maser input reference flange when switched to the antenna, is given as

$$T''_{SA} = T''_A + T''_R \quad (1)$$

Expressing the antenna and receiver temperatures in terms of their respective temperature components gives

$$T''_A = T'_A + T_L \quad (2)$$

and

$$T''_R = T''_M + T''_F \quad (3)$$

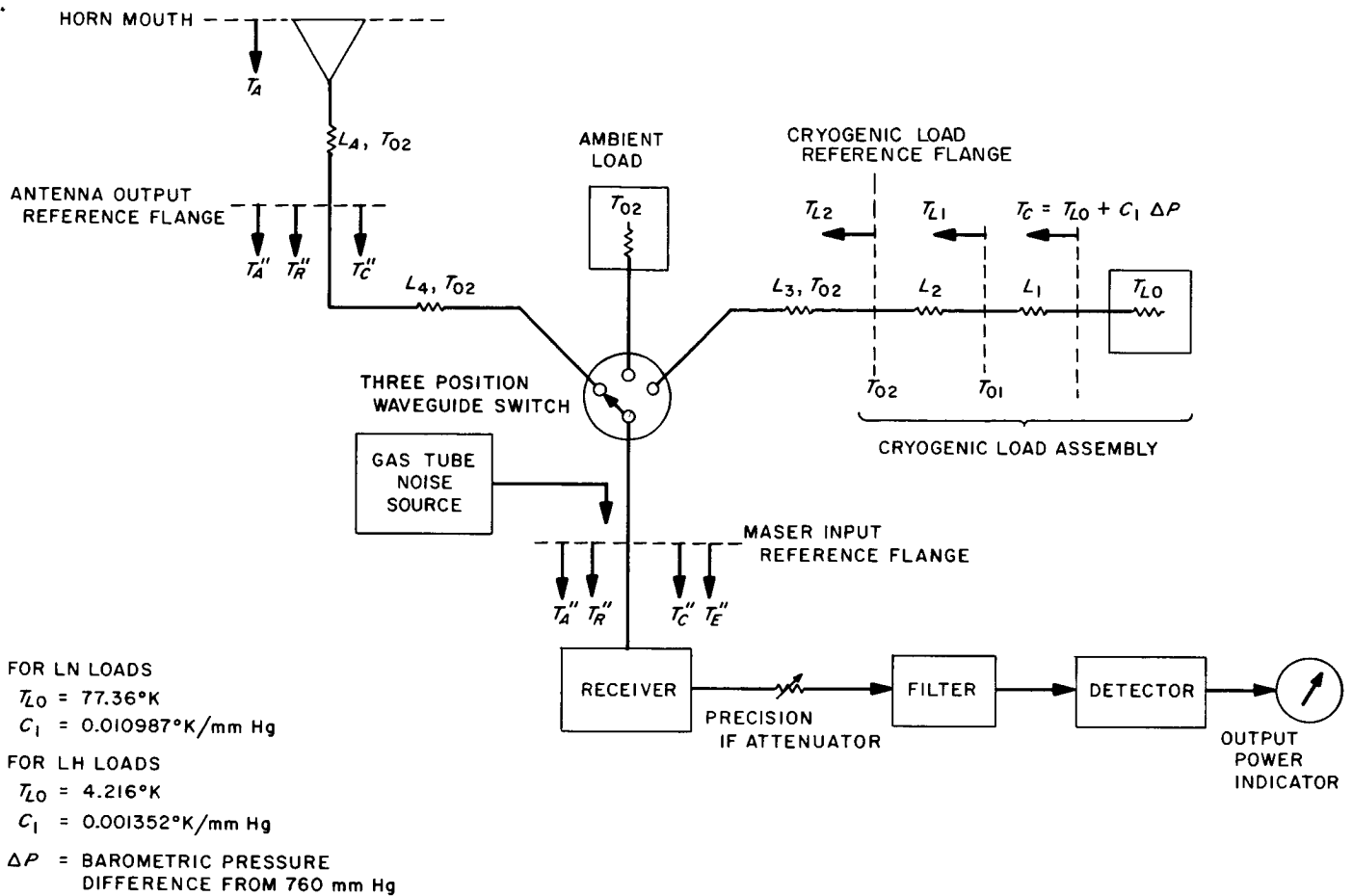


Fig. 8. Block diagram of basic noise temperature measurement system

where

$T'_A$  = antenna temperature defined at the antenna output reference flange,  $^\circ\text{K}$

$T_L$  = temperature contributed by the dissipative loss of the transmission line between the antenna output and maser input reference flanges,  $^\circ\text{K}$

$T''_M$  = maser temperature defined at the maser input reference flange,  $^\circ\text{K}$

$T''_F$  = follow-up receiver temperature contribution defined at the maser input reference flange,  $^\circ\text{K}$

Substitution of Eqs. (2) and (3) into Eq. (1) gives the following expression of antenna system temperature:

$$T''_{SA} = T'_A + T_L + T''_M + T''_F \quad (4)$$

The results of weekly noise temperature calibrations in the following section will be presented in terms of the components of system temperature given in Eq. (4).

## 2. Calibration Results

Periodic calibrations of the absolute receiver and antenna temperatures as well as calibrations of gas tube excess temperatures for the Mars Deep Space Station (DSS) and Venus DSS antenna systems have been continuing on a weekly basis.<sup>2</sup> Earlier weekly calibration work on these antenna systems has been reported in SPS 37-39, Vol. III, pp. 92-96 (for Mars DSS), and SPS 37-41, Vol. III, pp. 82-86 (for Venus DSS).

The antenna system being calibrated at Mars DSS consists of the 210-ft diameter paraboloid and a multifrequency cone (formerly called the listening cone). At Venus DSS, calibrations are being done on the antenna

<sup>2</sup>This work is being done by Venus DSS personnel.

system consisting of the 85-ft diameter paraboloid and the R&D cone. The type of cryogenic thermal noise standard being used to calibrate both of these antenna systems is a liquid nitrogen-cooled WR 430 waveguide load.

A plot of all weekly noise temperatures calibrated to date may be seen in Figs. 9 and 10 for the Mars and Venus DSS antenna systems, respectively. Each value represents an average obtained from 10 sets of Y-factor measurements. These figures show that problems are being encountered in these weekly calibrations. For instance, Fig. 9 shows that recent calibrated values have begun to fluctuate excessively. The Mars DSS calibrated antenna temperatures, as defined at the antenna flange, have been varying between maximum and minimum values of 12.5 and 3.4°K, while the calibrated maser temperature values have been fluctuating between 17.5 and 3.6°K. Antenna temperatures of 12.8 to 4.5°K and maser temperatures of 10.4 to 6.3°K have been calibrated for the Venus DSS antenna system.

Although the calibrated temperature fluctuations are not as severe for the Venus DSS antenna system, definite

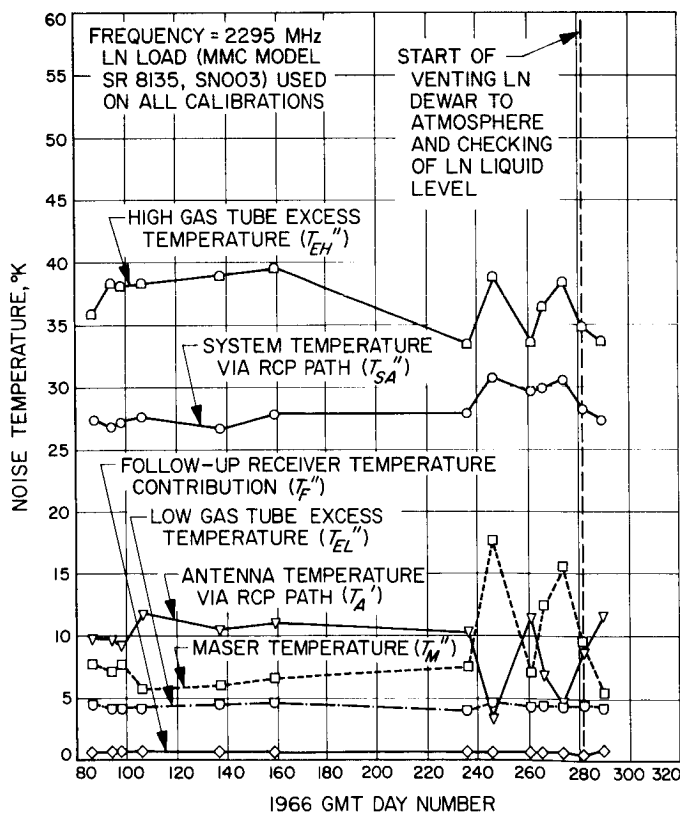


Fig. 9. Mars DSS advanced antenna system weekly calibrated noise temperatures

calibration problems appear to exist for both stations. It is suspected that the major cause of the inconsistencies in the calibrated data is the instability of the liquid nitrogen-cooled loads. This source of error is suspected because there does not appear to be similar types of fluctuations existing in the daily calibrations. A study has been in progress to determine several possible causes of errors in the weekly temperature calibrations. Some of the problems being investigated are:

- (1) Are the measured Y-factor ratios dependent upon the detector bias voltage setting?
- (2) What is the effect of not venting the cryogenic load dewar to the atmosphere?
- (3) Is the termination element of the liquid nitrogen-cooled load actually at the cryogenic liquid temperature?
- (4) Are the temperature fluctuations due to changing mismatch conditions of the thermal noise standards, antenna, or receiver?
- (5) Are the weekly calibrations being affected by system bias errors (such as external spurious signals or other noise contributions) not present in daily calibrations?

Special tests have been made to determine the effects of (1) changing detector bias voltage settings, (2) pressurizing and not pressurizing the liquid nitrogen load with helium gas, and (3) venting and not venting the cryogenic dewar to the atmosphere. A 1-psi increase in pressure on the liquid nitrogen fluid will raise the liquid nitrogen temperature by approximately 0.6°K. The results of the tests are summarized in Tables 2 and 3, and the effects of the various operating conditions on the calibrated temperatures can be noted. Each temperature value shown in the tables is the average obtained from 10 sets of Y-factor measurements. These special tests have established that the detector bias should be set at approximately 4.0 mv for linearity reasons, and the cryogenic dewar should always be vented to the atmosphere. The various problem areas will continue to be investigated.

Even with optimum operating conditions, a liquid nitrogen-cooled load may not provide the resolution and accuracy needed for the weekly calibrations. An analysis of probable errors and mismatches indicates that for calibration of low-noise receiver and antenna temperatures, it would be more accurate to use a waveguide liquid helium-cooled load rather than a liquid nitrogen-cooled load. However, a satisfactory field-type liquid helium

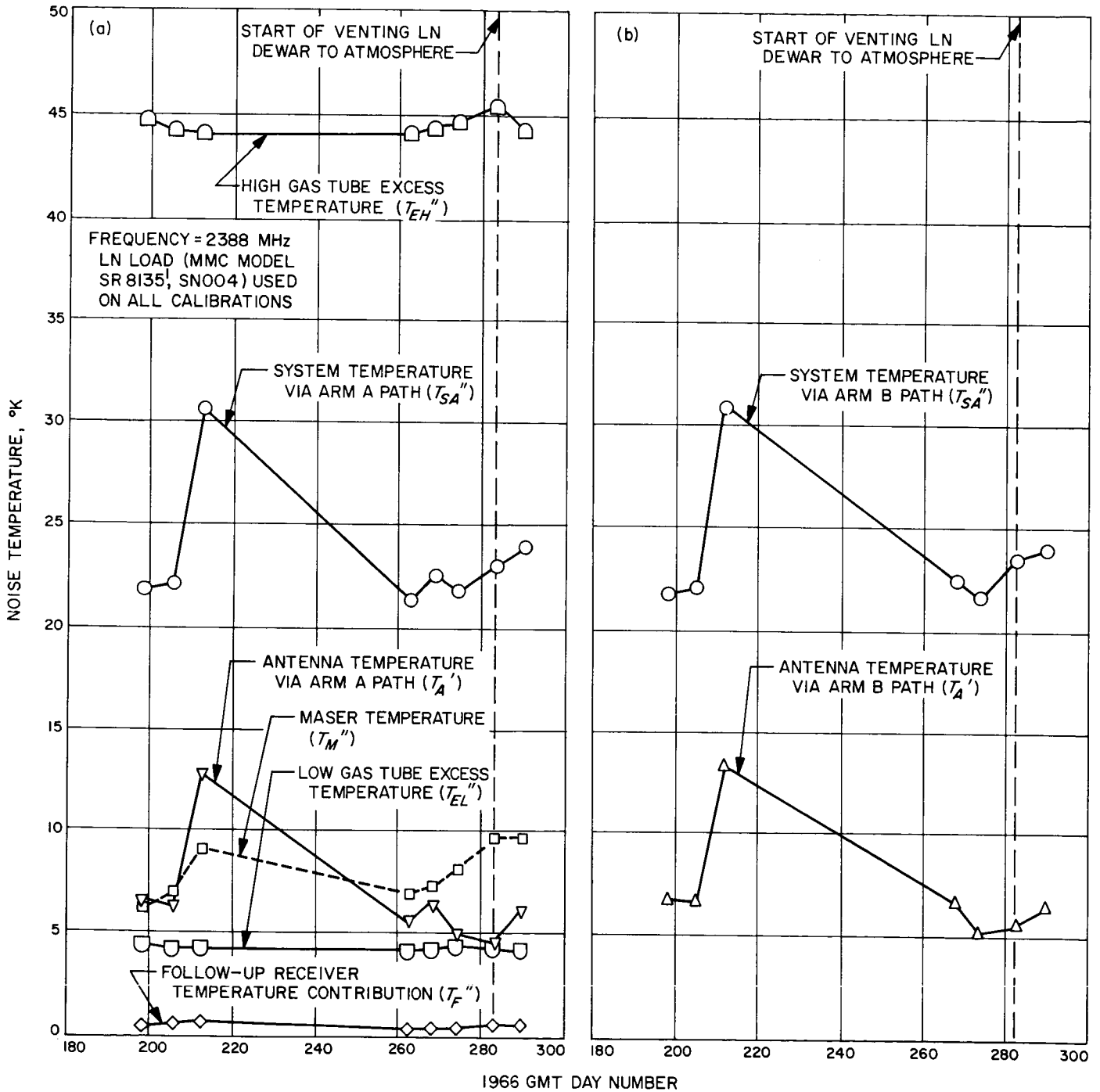


Fig. 10. Venus DSS antenna system weekly calibrated noise temperatures: (a) antenna and system noise temperatures are via Arm A path only; (b) antenna and system noise temperatures via Arm B path

**Table 2. Special noise temperature calibration tests on the Mars DSS advanced antenna system at 2295 MHz**

Part A. Detector bias voltage tests												
Description of test	1966 GMT day No.	GMT, hour and minutes	$T_A'$ via RCP path, °K	$T_M''$ , °K	$T_F''$ , °K	$T_{NA}''$ via RCP path, °K	$T_{EL}''$ , °K	$T_{RH}''$ , °K	Maser gain, db	Reflectometer readings, db		
										Antenna via RCP path	Ambient load	LN load
Sensitive detector used, 4-mv bias	159	1900	11.11	6.60	0.66	27.75	4.67	39.51	39.5	40.3	39.6	38.3
Less sensitive detector used, 4-mv bias	159	2015	10.83	6.20	0.66	27.12	4.40	38.99	39.8	40.9	41.1	38.2
Less sensitive detector used, 2-mv bias	159	2030	11.37	5.92	0.65	27.35	4.28	39.03	39.8	4.07	41.2	38.3
Part B. Liquid nitrogen load pressurization tests <sup>a</sup>												
LN load pressurized with He gas (normal procedure)	261	0415	11.45	7.11	0.67	28.59	4.30	33.57	40.2	30.8	33.9	41.0
LN load not pressurized	261	0530	10.90	7.35	0.66	28.27	4.18	33.48	40.2	30.7	33.9	43.4
Part C. Liquid nitrogen dewar pressurization tests												
LN dewar vented through slit in rubber tubing	282	0615	12.49	3.02	0.78	25.51	4.27	31.93	40.3	30.0	33.7	41.8
LN dewar vent tube open to the atmosphere	282	0830	8.70	9.61	0.51	28.16	4.50	34.82	41.7	30.0	33.4	41.7
LN dewar vented through slit in rubber tubing	289	2108	13.34	3.59	0.85	27.09	3.99	32.48	40.0	31.0	40.8	41.8
LN dewar vent tube open to the atmosphere	289	2150	11.67	5.48	0.88	27.42	4.31	33.69	40.1	31.4	40.9	40.6

<sup>a</sup> Reflectometer was retuned on day No. 172.

**Table 3. Special noise temperature calibration tests on the Venus DSS antenna system at 2388 MHz**

Liquid nitrogen dewar pressurization tests												
Description of test	1966 GMT day No.	GMT, hour and minutes	$T_A'$ via Arm A path, °K	$T_M''$ , °K	$T_F''$ , °K	$T_{NA}''$ via Arm A path, °K	$T_{EL}''$ , °K	$T_{EH}''$ , °K	Maser gain, db	Reflectometer readings, db		
										Antenna via Arm A path	Ambient load	LN load
LN dewar vented through slit in rubber tubing	283	0402	3.35	10.39	0.51	22.66	4.24	45.8	38.8	35.7	48.4	53.4
LN dewar vent tube open to the atmosphere	283	0429	4.53	9.57	0.51	22.99	4.31	46.4	38.5	35.3	47.3	56.9
LN dewar vented through slit in rubber tubing	290	1000	5.11	8.07	0.46	21.81	4.23	44.5	38.5	36.0	44.8	38.7
LN dewar vent tube open to the atmosphere	290	1056	6.13	9.67	0.46	23.92	4.22	44.2	38.8	36.0	41.4	42.0

waveguide load has not yet been developed. It is suggested that a good operational liquid helium load be developed and used on a trial basis for absolute temperature calibrations now being performed on the antenna systems at Goldstone.

**N67 15911**

**D. Efficient Antenna Systems: Calculated Gain of the Advanced Antenna System, A. C. Ludwig**

The gain of a 210-ft diameter antenna with uniform aperture illumination at 2295 MHz is 63.75 db. Expected gain of the real antenna is computed by evaluating the effect of deviations from the ideal antenna. Losses occur due to (1) nonuniform aperture illumination and spillover, (2) aperture shadowing or blockage by the subreflector and its support structure (quadripod), and (3) deviations of the reflecting surfaces from a perfect paraboloid or hyperboloid, including misalignment or defocusing of the feed and subreflector.

**1. Nonuniform Aperture Illumination and Spillover**

The primary feed for this antenna is a modified dual mode horn (Ref. 2 and SPS 37-36, Vol. IV, pp. 249-251).

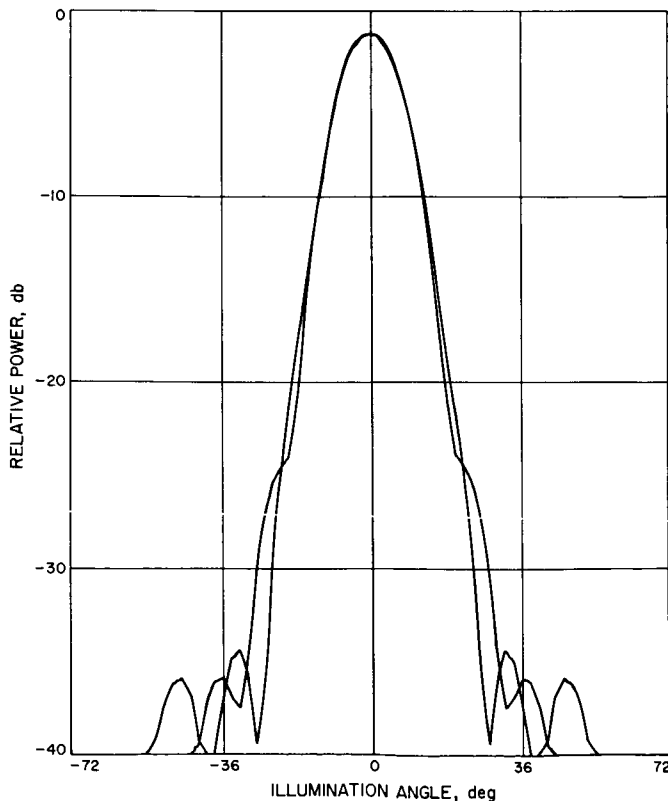


**Fig. 11. Primary feed pattern**

Experimental principal plane patterns, which are sufficient to completely determine the radiation of this type of feed (SPS 37-26, Vol. IV, pp. 200-208), are shown in Fig. 11. The phase patterns, which are not shown, are virtually flat over the region of interest. The subreflector, which consists of a hyperboloid with a conical flange (Ref. 3), subtends  $\pm 14^\circ 39.3'$  of the feed pattern, resulting in 7.44% forward spillover.

The scattered pattern from the subreflector (main reflector illumination) is shown in Fig. 12. This pattern was computed numerically using a computer program (Ref. 4) that has demonstrated outstanding agreement with experimental results for similar situations.<sup>3</sup> The illumination efficiency of this pattern was evaluated with a second computer program (Ref. 4) that solves an exact integral for efficiency, and also divides the net loss into several components, some of which are approximate (SPS 37-26, Vol. IV, pp. 200-208). These losses<sup>4</sup> are shown in Fig. 13 along with other losses, discussed shortly. The net loss due to nonuniform aperture illumination and spillover past the subreflector and main reflector is 1.15 db.

**2. Aperture Blockage**

The aperture blockage due to the subreflector and quadripod is illustrated in Fig. 14. (The antenna shown is a scale model of the 210-ft diameter antenna.) The outline of the structure blocks 7 1/2% of the aperture. However, since the quadripod is not a solid structure, one may assume an opacity factor to more accurately approach the true blockage.

Fig. 15 shows a projection of the quadripod structure, as seen by a ray from the focus reflected by the inner portion of the reflector (inside the quadripod structure). Optically, the projection is 71% opaque. A similar projection shows that for a ray coming directly from the focus towards the outer portion of the reflector, the structure is optically 47% opaque (approximately). After weighting by energy and area distributions, the effective average optical opacity is found to be approximately 60%.

The exact relation between optical and RF opacity is not known. An estimate of RF opacity of 80% was taken

<sup>3</sup>A. C. Ludwig and W. V. T. Rusch, Digital Computer Analysis and Design of a Subreflector of Complex Shape (a JPL Technical Report to be published).

<sup>4</sup>The loss due to nonuniform amplitude illumination is fairly high because the feed system was designed for optimum figure-of-merit rather than optimum gain. Illumination efficiency was sacrificed to obtain extremely low spillover past the main reflector, to reduce antenna noise temperature (SPS 37-34, Vol. IV, pp. 239-241).

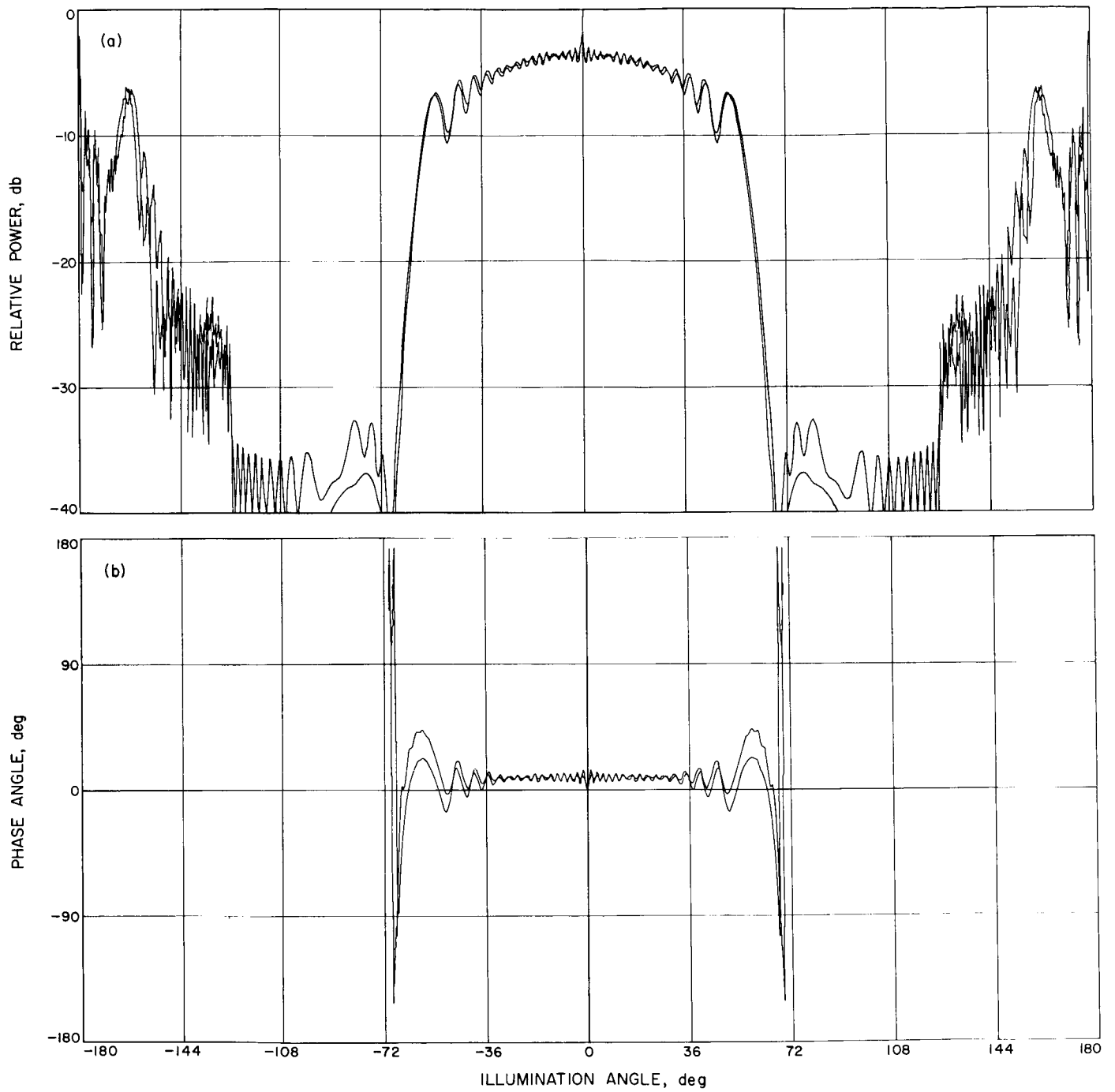


Fig. 12. Subreflector scattered pattern: (a) amplitude; (b) phase

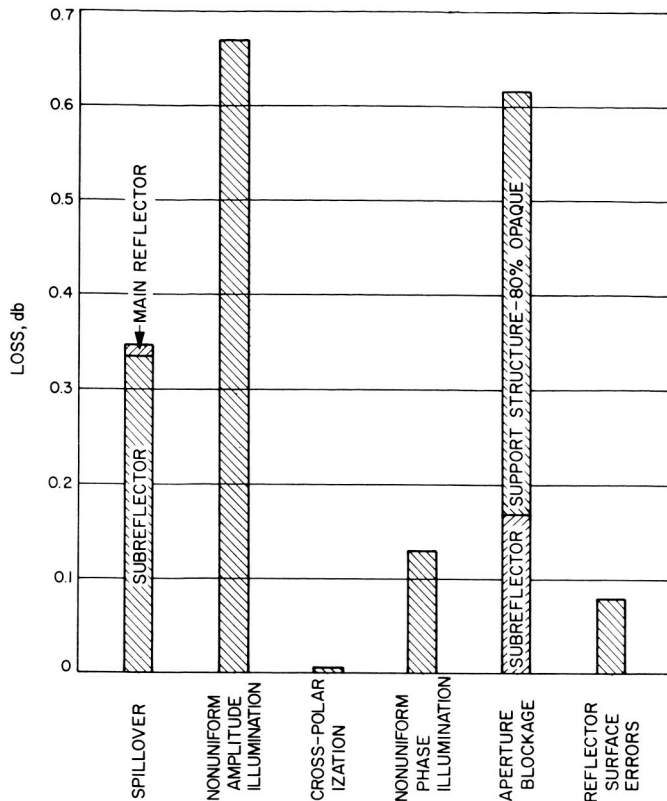


Fig. 13. Gain loss factors

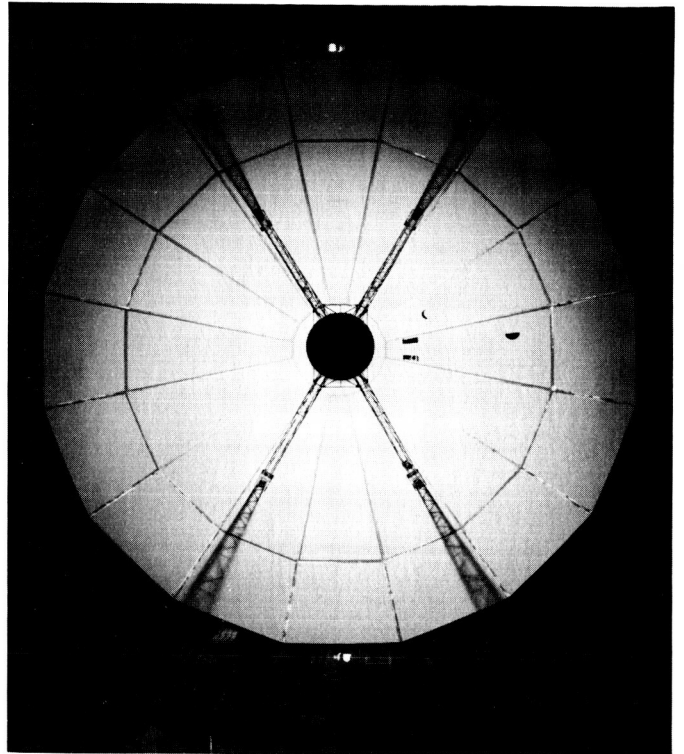


Fig. 14. Aperture blockage

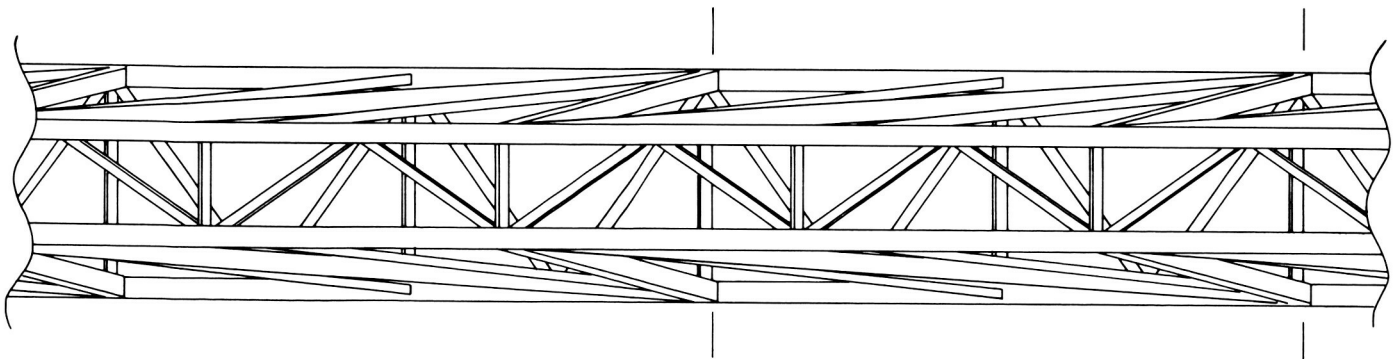


Fig. 15. Projection of quadripod structure onto aperture of the antenna

as nominal. (The uncertainty in this estimate is discussed under error analysis, presented later in this article.) The subreflector was taken to be 100% opaque. On this basis, loss due to blockage, as shown in Fig. 13, is 0.62 db.

### 3. Structural Deviations

A structural analysis of this antenna has been considered in detail previously.<sup>5</sup> The resulting errors have an rms value of  $\leq 0.057$  in., under very ideal conditions (no

<sup>5</sup>M. S. Katow, private communication, 1966.

wind or thermals, approximately 45-deg elevation angle). Although components of this error do not have a strictly normal distribution, direct aperture integration indicates close agreement with the value calculated with the method formulated by Ruze (Ref. 5). This value is a loss of 0.080 db.

### 4. Error Analysis and Predicted Gain

The ground rule adopted for this error analysis is to make estimates for each loss component that is believed

to have a 95% probability of bracketing the true value. For normal distributions, this would represent the  $2\sigma$  deviation of these quantities. Total error is computed as the square root of the sum of the squares of individual errors. Although some errors are neither strictly normal nor totally independent, this is believed to be the most reasonable evaluation.

Error estimates are shown in Fig. 16. By far the dominant uncertainty is due to blockage, a result of the uncertainty in the opacity factor as discussed earlier. The tolerance shown corresponds to opacity factors of 50 to 100%. The total tolerance in loss factors is  $+0.17, -0.19$  db.

The sum of the loss factors in Fig. 13 is 1.85 db. Combining this with the gain for the ideal case, the resulting predicted gain is  $61.90 +0.19, -0.17$  db, under ideal environmental conditions as mentioned earlier. Note that the tolerances listed apply only to the factors considered in the loss computations.

Although every effort was made to make the analysis thorough, it is conceivable that a loss factor could have been omitted. Therefore, in a strict sense, the above tolerance is not necessarily the overall tolerance on the pre-

dicted value versus the true value. Ultimately, this uncertainty can be removed only by a good experimental gain measurement.

## N67 15912

### E. Efficient Antenna Systems: X-Band Gain

Measurements, D. A. Bathker, and G. S. Levy

#### 1. Summary

In ideal antennas the gain increase is proportional to the frequency squared; however, in real antennas aperture phase errors, due to surface tolerance effects, do not permit the realization of this gain-frequency relationship. When the frequency rate of change of gain loss due to surface effects is equal and opposite to the  $f^2$  law rate of change of gain, the antenna is said to be at gain limit. An experimental program has been undertaken to investigate the behavior of the DSIF antennas as they approach gain limit. Gain measurements have been made in the past at S-band, and the next step is measurements at X-band.

An X-band 85-ft antenna cassegrainian cone has been built and will be used to measure gain at the Venus station. Celestial radio sources will then be observed, and

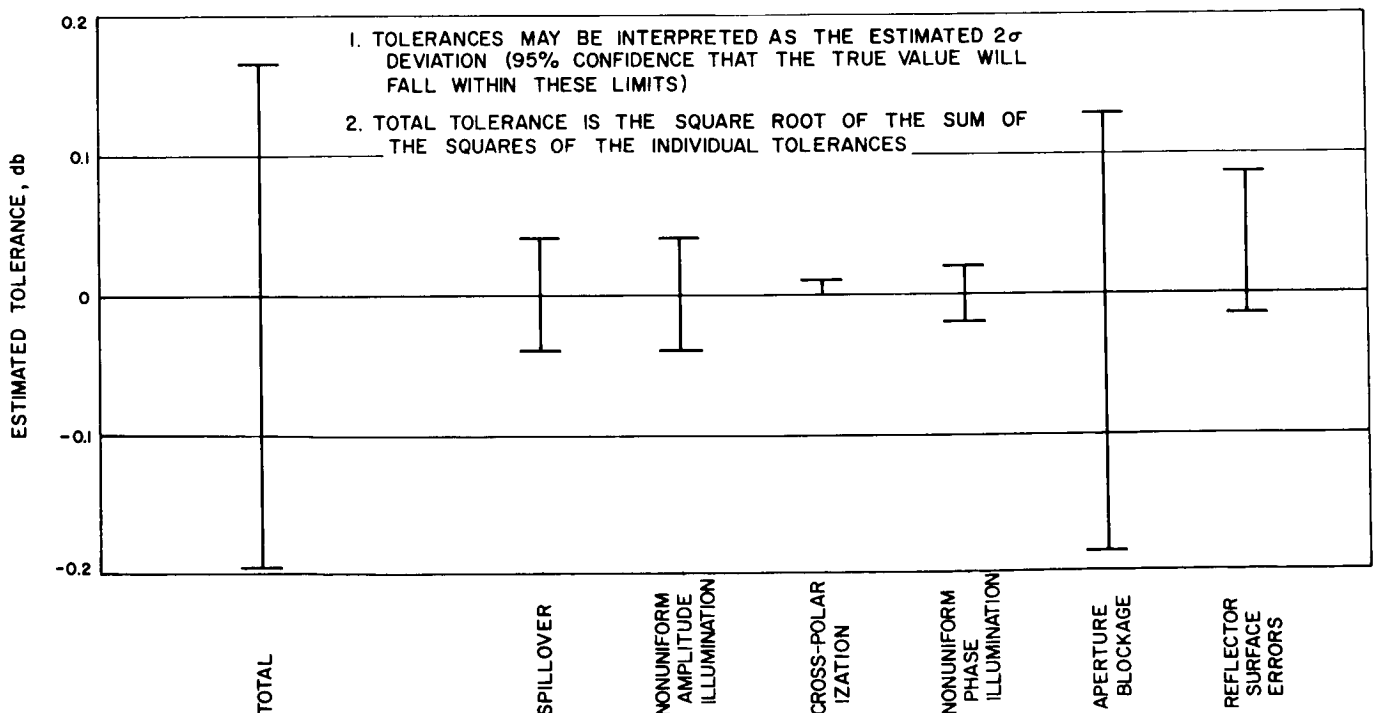


Fig. 16. Estimated tolerances on gain loss factors

the flux density will be determined. The next step will be to measure the gain of the 210-ft advanced antenna system at X-band, using the same cassegrainian cone. Ultimately it is planned to repeat this procedure at C- and K-bands.

## 2. Introduction

In Ref. 6 the tradeoffs involved in optimizing large antennas for space communications are discussed. The concept of gain limit, which is the maximum gain a given antenna can achieve, is introduced.

An ideal antenna's gain is proportional to the square of operating frequency. However, in real antennas the performance of an antenna is deteriorated by surface imperfections. The loss in gain is given by  $G/(G_0) = \exp - [(4\pi\sigma)/\lambda]^2$ , where  $\lambda$  is the free space wavelength, and  $\sigma$  is the rms RF path length error due to surface deviations (Ref. 7). At some given frequency the derivative of the gain loss due to surface imperfections cancels the  $f^2$  gain increase; this is said to be gain limit. Fig. 1 of Ref. 6 shows gain versus frequency for the DSIF 85- and 210-ft antennas for two ratios of rms surface deviation to paraboloid diameter.

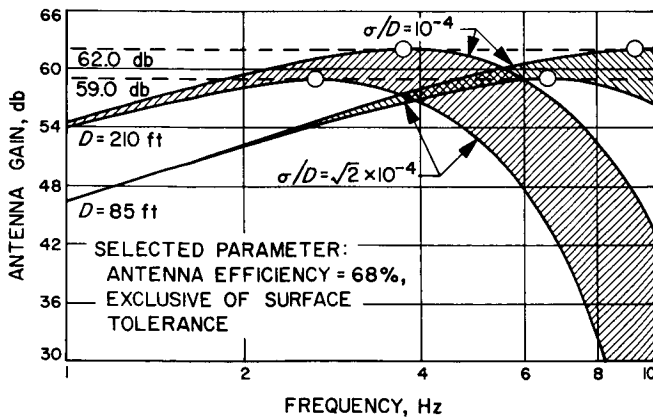


Fig. 17. Gain vs frequency, size, and surface tolerance for one ground antenna

Measurements well below the gain limit have been made at S-band on the 85-ft dishes (Ref. 8), but there are very few experimental data in the region near and above gain limit. An experimental program has been started to measure the 85- and 210-ft antennas at X-band. There are plans to repeat these measurements at C- and K-band.

## 3. X-Band Measurement

An X-band feed system has been designed to fit in a standard DSIF cassegrainian support cone. This feed system can be used on either the 85-ft Venus station antenna or on the 210-ft advanced antenna system.

The first 8448 MHz tests will be conducted at the Venus station, where antenna gain and pattern measurements can be made using the Mount Tiefert collimation station. Measurements will also be made of the antenna

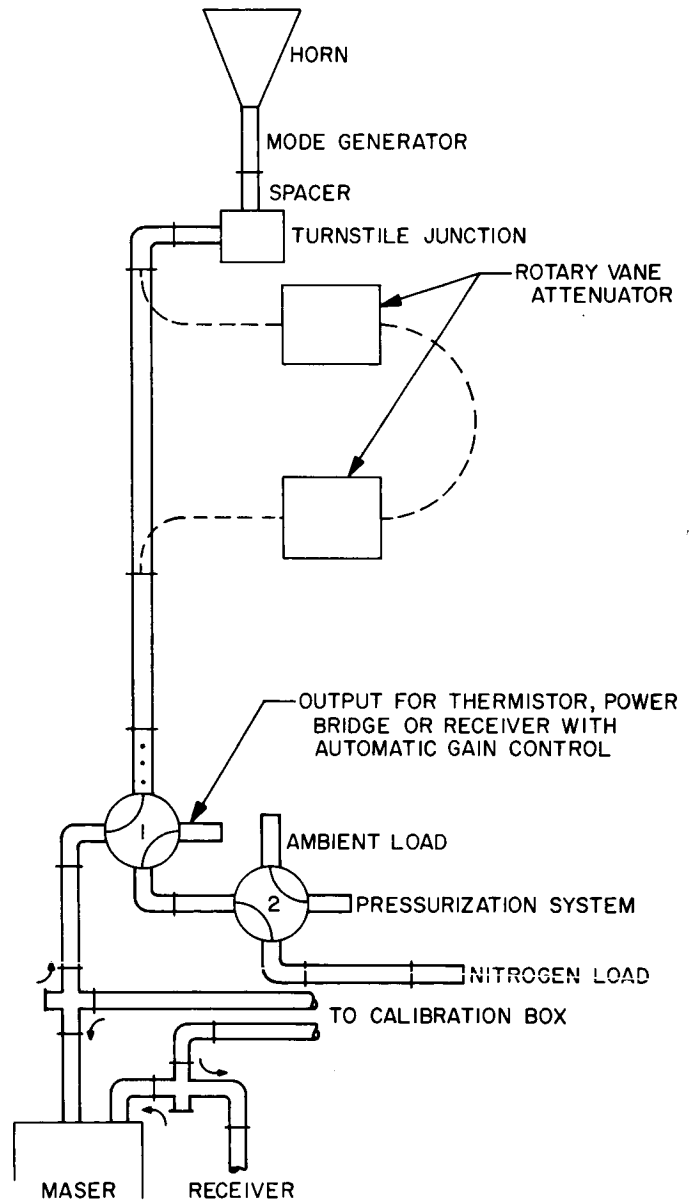


Fig. 18. Diagram of feed and waveguide in the X-band cone

temperature before and after installation on the 85-ft paraboloid to determine the spillover contribution. Measurements of celestial source temperature will be made, and these data will then be used in conjunction with the gain data to obtain absolute source flux density.

Fig. 18 is a diagram of the feed and waveguide system in the X-band cone. A dual mode horn, which is a scaled version of the Venus station radar feed (Ref. 7), is employed. The feed will use circular polarization generated by the turnstile junction and fed through the mode generator. A section of waveguide below the turnstile junction is replaceable with two rotary vane attenuators to be used for antenna pattern calibrations. Waveguide switch 1 will permit either the maser and radiometric receiver or the crystal mixer receiver with automatic gain control (AGC) to look at either the antenna or the precision terminations. The maser, radiometric receiver, and precision loads will be used for antenna temperature and radio source measurement and are discussed elsewhere in this report. The AGC receiver will be used for antenna pattern measurements and can be replaced by a thermistor and power bridge for gain measurements.

The hyperboloid, flange, and vertex plate used in this experiment will be S-band devices. Ludwig (SPS 37-41, Vol. III, p. 90) has computed the perturbations caused by using the S-band devices at X-band, and these corrections will be used in determining gain. It was decided that construction of vertex plate and flange for X-band would not be desirable with regard to cost and station time.

After completion of the Venus station experiment, it is planned to use this feed-cone at the Mars station. The same celestial sources will be examined, and by using the Venus station values of flux density, the gain can be measured for the 210-ft dish at X-band.

# N67 15913

## F. Low Noise Receivers: Microwave Maser Development, S. M. Petty, and R. C. Clauss

### 1. Summary

A traveling wave maser (TWM) has been constructed for use at 8448 MHz. It provides a net gain of 41.5 db when installed in a closed-cycle helium refrigerator operating at 4.4°K. The maser provides more than 30 db net gain over a tunable range of 140 MHz. An equivalent input noise temperature of approximately 18°K has been measured.

### 2. Maser Structure Description

The maser structure (Fig. 19) accepts both signal and pump waveguides at one end. Transitions from rectangular to ridged waveguide are used to reduce the maser diameter. The slow-wave comb structure is folded, resulting in 4 in. of active length in 2 in. of uniform magnetic field. The end loop, which couples the halves of the maser, is shown in Fig. 20.

Loading of the comb structure is shown in Fig. 21. The maser material is ruby (0.05% Cr<sub>2</sub>O<sub>3</sub>). C-axis orientation of the ruby with respect to the DC magnetic field is 54° 44', which allows push-pull pumping. Ten thin disks of polycrystalline yttrium iron garnet (YIG), spaced uniformly throughout the comb structure, provide sufficient isolation to ensure stable amplification. Additional loading to give the desired center frequency and electrical length is provided by alumina strips. Beryllium copper shims 0.005-in. thick secure the alumina and ruby in place.

In Fig. 22, the disassembled maser structure is shown. All parts are oxygen-free, high-conductivity copper, and pure indium sheeting is placed in all joints to prevent RF leakage and to improve heat transfer across these joints.

### 3. Package Description

The maser structure is shown installed in a closed-cycle helium refrigerator developed at JPL (SPS 37-39, Vol. III, p. 79) (Fig. 23). The signal waveguides are 0.010-in. wall stainless steel, copper plated with a gold flash. Commercial mica pressure windows provide the vacuum seal.

Fig. 24 shows the complete maser package. The welded aluminum frame and the Alnico-5 magnet (modified to provide a 3800-gauss field for 8448-MHz operation) are the same as those used in existing S-band masers at the Mars and Venus stations. The pump package contains a Varian VA-282 klystron and provides 200 mw of pump power at 21.85 GHz.

During laboratory testing, maser gain changes occurred when changing input terminations. These changes were found to be not a function of the match at the signal frequency (the maser being very insensitive to input or output VSWR changes), but a function of reflected pump energy which behaves in an unpredictable manner in the signal waveguides. Gain changes as large as 1 db occurred, even though the maser appeared well saturated with pump power. A low pass waveguide filter (15 GHz cutoff frequency) was installed at the maser input (Fig. 24).

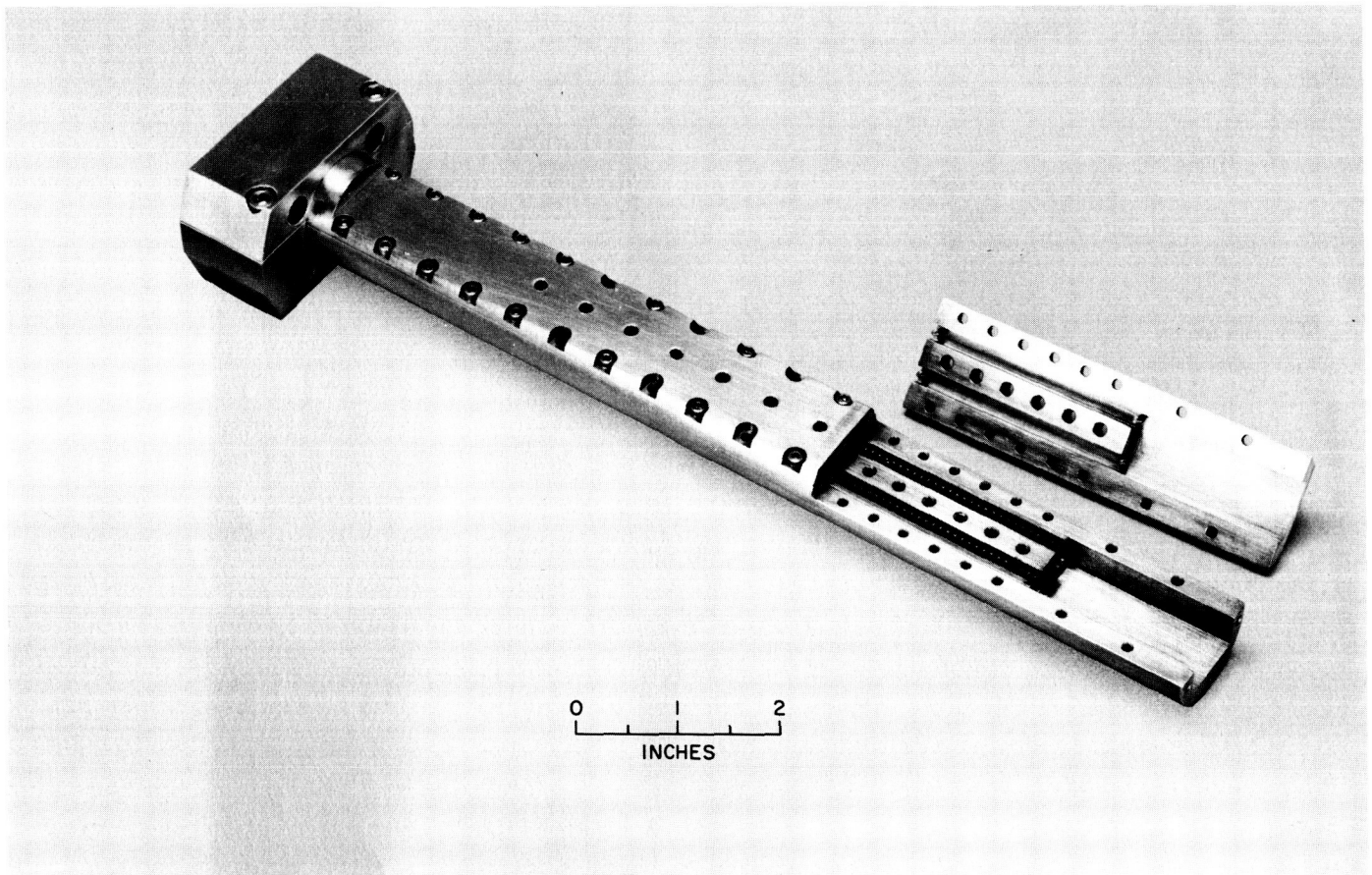


Fig. 19. Maser structure partially disassembled

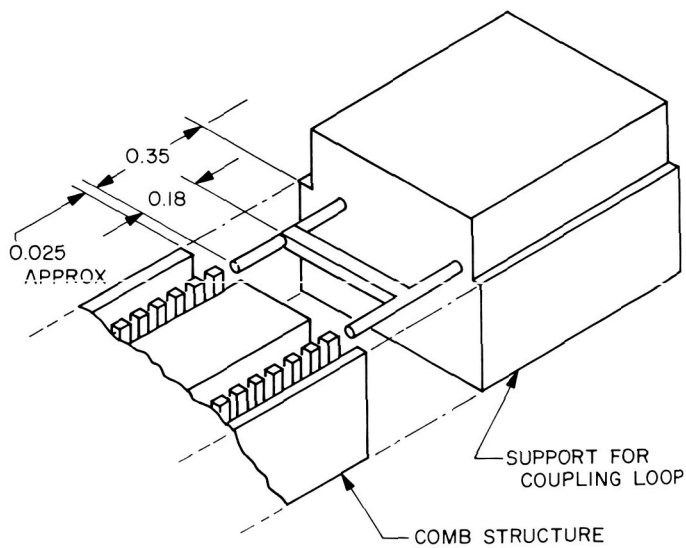


Fig. 20. End coupling loop in position behind comb structure

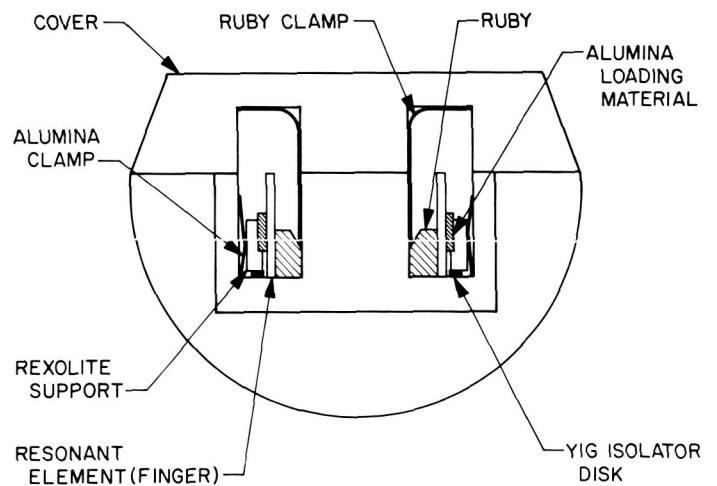


Fig. 21. End view of maser structure

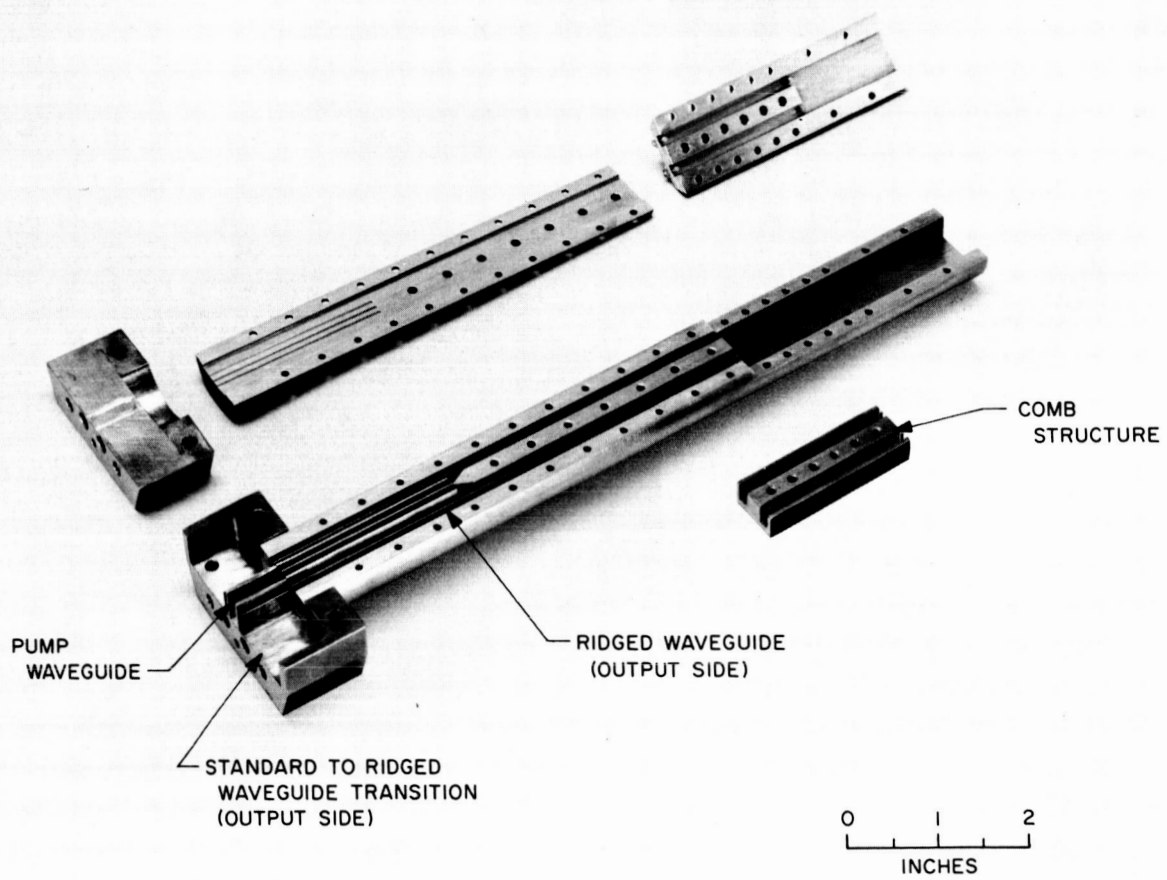


Fig. 22. Maser structure disassembled

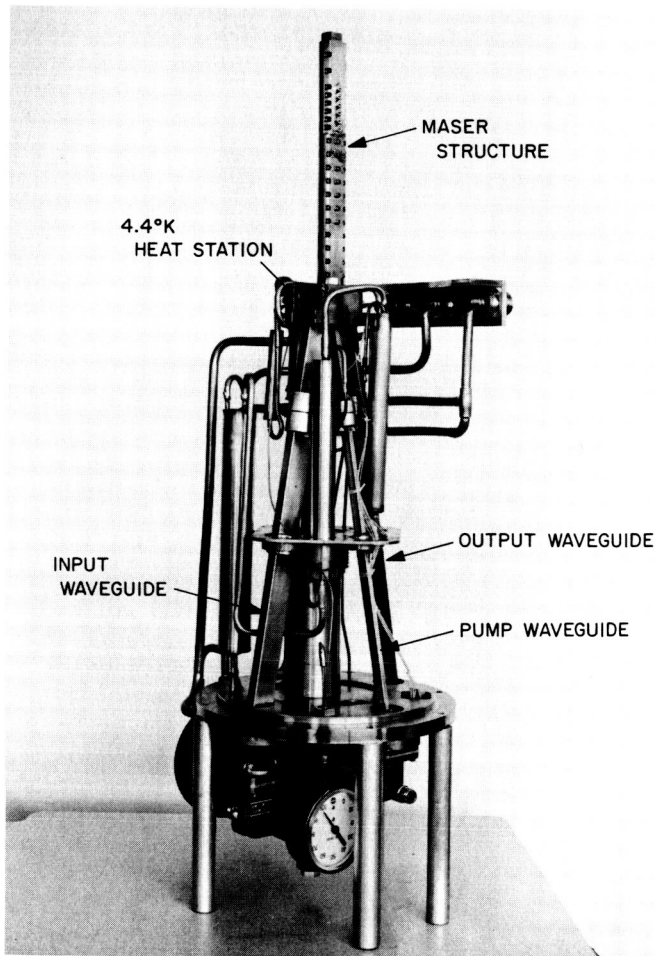


Fig. 23. Maser in closed-cycle refrigerator

This filter has greater than 40-db rejection at the pump frequency and 0.042 db insertion loss at 8448 MHz. Gain changes due to input load changes are now less than can be measured with existing test equipment.

Table 4. Maser performance at 8448 MHz

Signal frequency	8448 MHz
Net gain	41.5 db
Magnetic field	3800 gauss
Bandwidth (3 db)	17 MHz
Forward loss	18.5 db
Electronic gain	60 db
Measured inversion ratio	2.8
Pump frequency	21.85 GHz
Measured equivalent input noise temperature	18°K

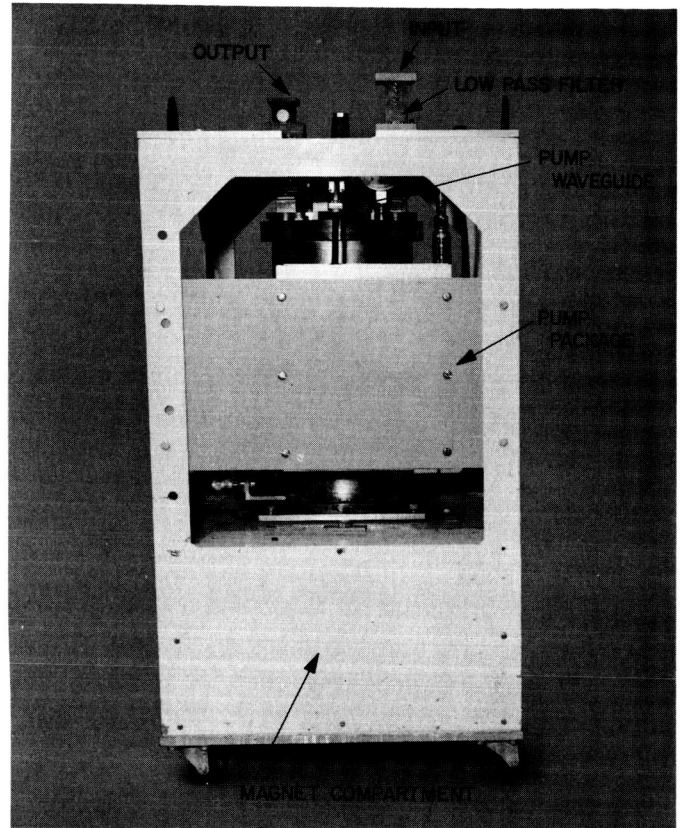


Fig. 24. Complete maser closed-cycle refrigerator package

#### 4. Performance

Table 4 summarizes the electrical characteristics of the TWM at 8448 MHz. The net gain of the maser (41.5 db) has a short term stability (minutes) better than 0.1 db, but

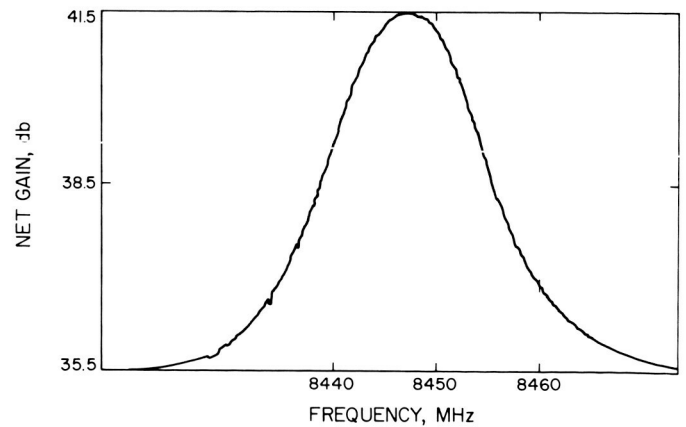


Fig. 25. Bandpass characteristic of TWM at 8448 MHz

the long term stability is seriously impaired by temperature variations affecting the magnet. The gain and bandwidth at 8448 MHz are shown in Fig. 25. The measured equivalent input noise temperature of 18°K is higher than the predicted value (based on insertion loss measurements of input waveguide components, and the calculated maser noise temperature).

The maser can be tuned over a 140-MHz range with net gain exceeding 30 db. This is shown in Fig. 26. Cool down time of the closed-cycle refrigerator with this maser is 4.6 hr (no liquid nitrogen precooling) and 2.4 hr with precooling.

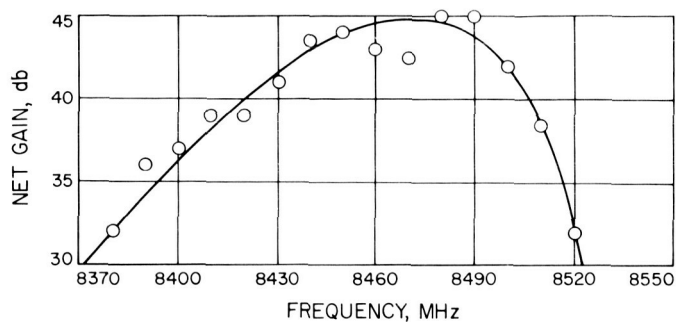


Fig. 26. Net gain as a function of frequency

**N67 15914**  
 G. X-Band Cone RF Instrumentation, C. T. Stelzried

The X-band cone RF instrumentation is described. This cone is immediately adaptable to the Goldstone Venus and Mars stations antennas and will be used to provide operational performance data of these antennas at 8448 MHz. A total power radiometer, using a maser amplifier and precision waveguide terminations, will be used for the necessary noise temperature calibrations.

The experimental X-band 8448 MHz cone can be used with either the JPL Goldstone 85-ft Venus station antenna or the 210-ft Mars station antenna. It will be used to provide information about antenna performance at this frequency. The first installation will be at the Venus station.

Preliminary noise temperature calibrations of the receiving system using the horn, maser, (see section III.F, this SPS) and monitor receiver have been made on the roof of Building 238 (Fig. 27). This equipment was used in a total power radiometer configuration with precision cryogenic waveguide terminations.

Results of the system temperature measurement will be presented at a future time. The difference between the

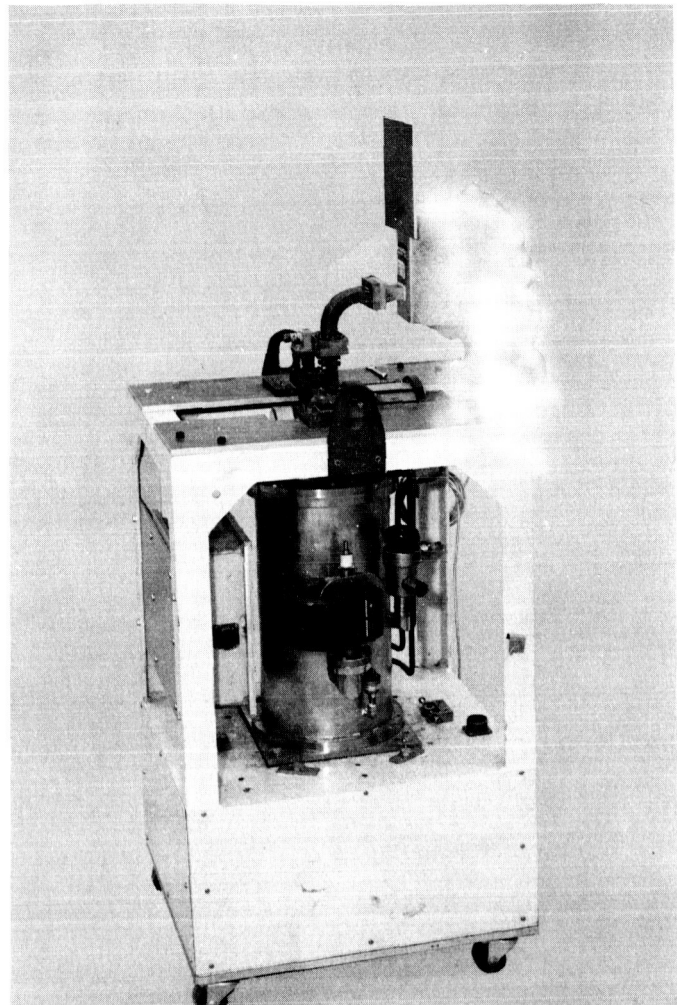


Fig. 27. Photograph of 8448-MHz maser with liquid nitrogen cooled termination used in noise temperature calibrations on the roof of Bldg. 238

system temperature measured with the horn connected directly to the maser input and that measured in the cone with the normal waveguide installation will provide a measure of the transmission line losses and a cross check on the normal waveguide insertion loss measurements.

A block diagram of the complete instrumentation is shown in Fig. 28. Provisions are made for measuring the horn, ambient and cryogenic wave guide termination VSWR's, maser gain, noise temperature and for monitoring the receiver local oscillator frequency. Fig. 29 shows the waveguide system undergoing laboratory insertion loss and VSWR measurements. Fig. 30 is a photograph of the initial phase of the cone installation. Figs. 31, 32, and 33 show the monitor receiver, noise box, and rack instrumentations for the cone and control room.

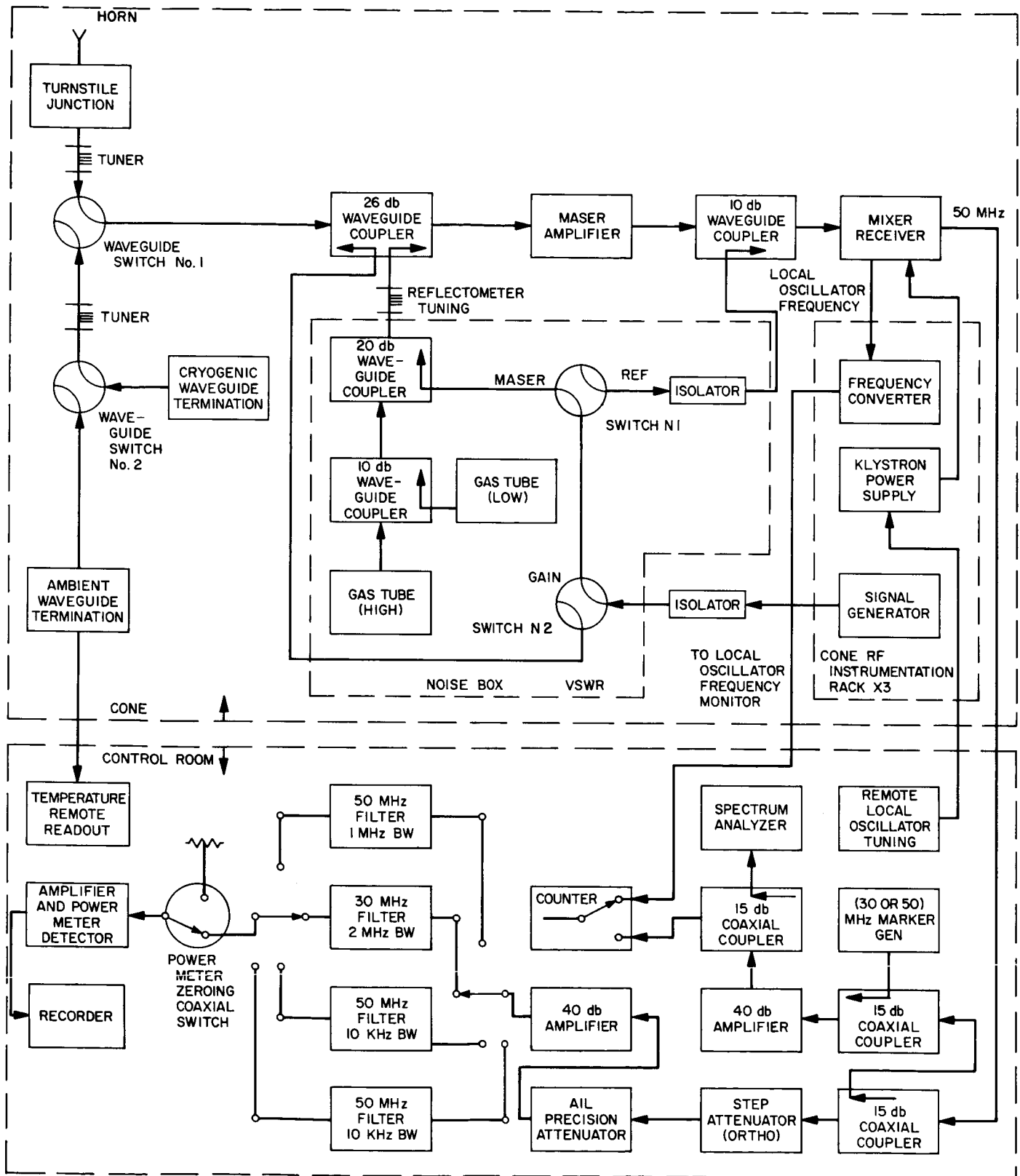


Fig. 28. Block diagram of 8448-MHz cone and control room RF instrumentation

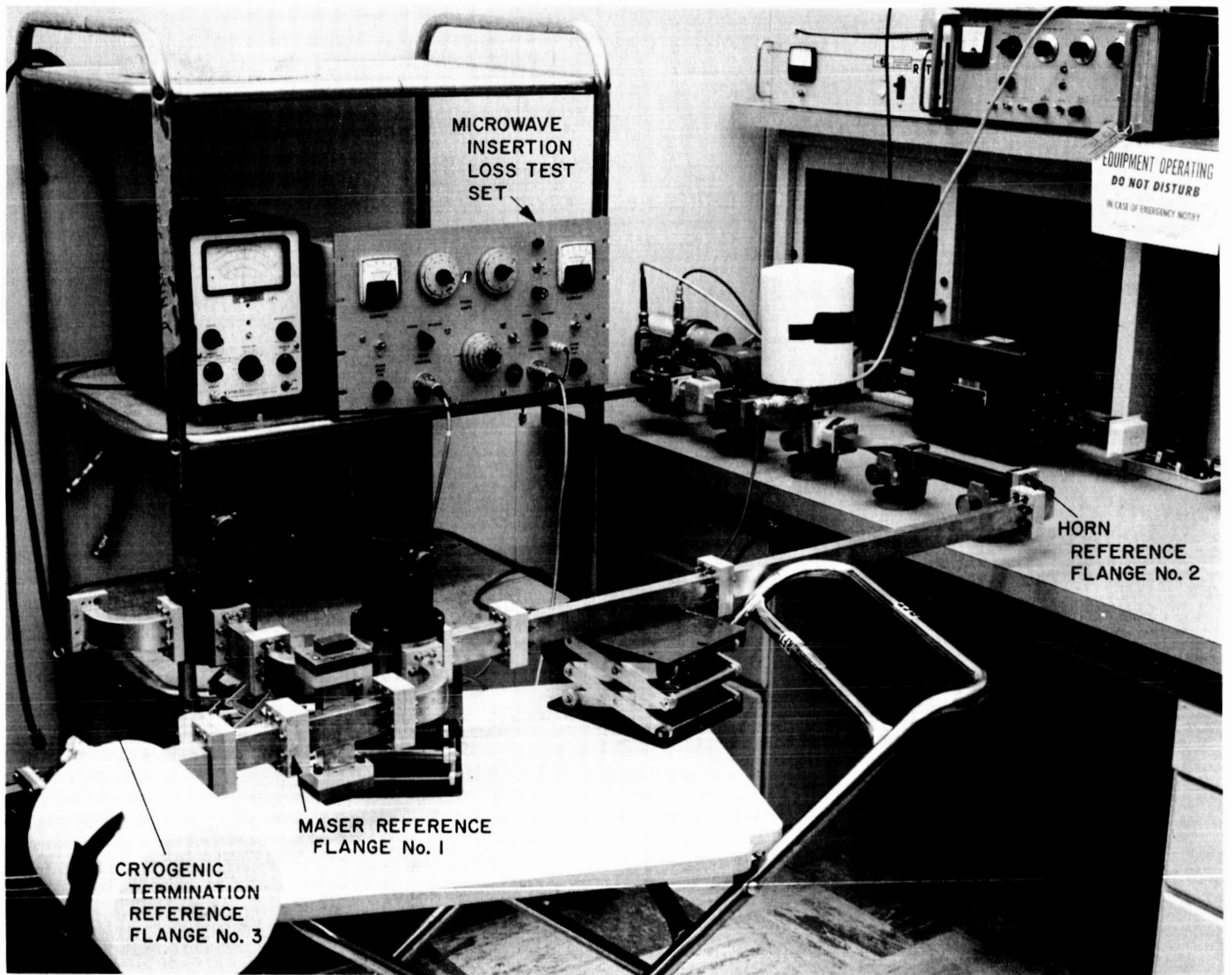
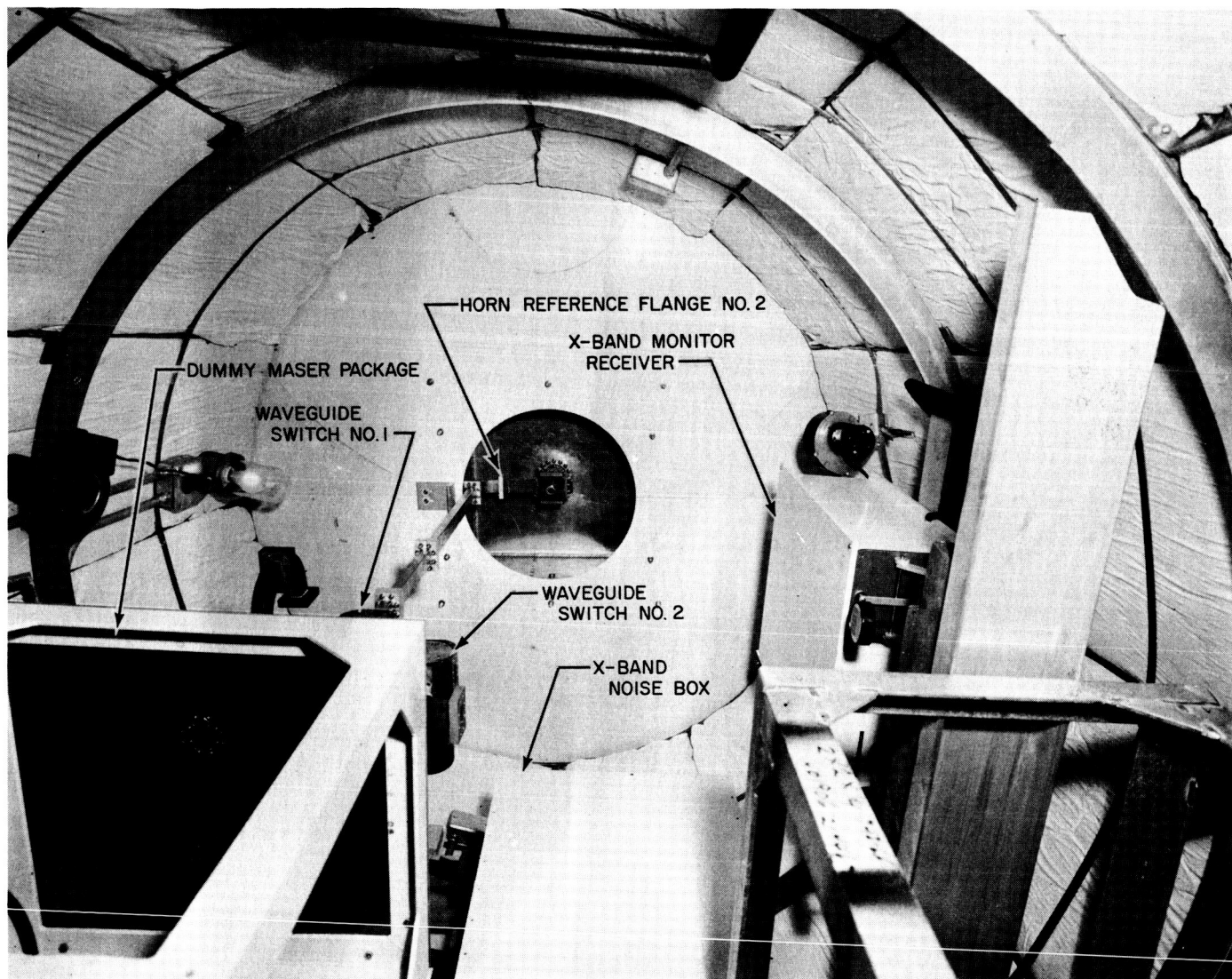


Fig. 29. X-band cone waveguide undergoing insertion loss and VSWR measurements in the laboratory



**Fig. 30. X-band cone interior during initial phase of component installation**

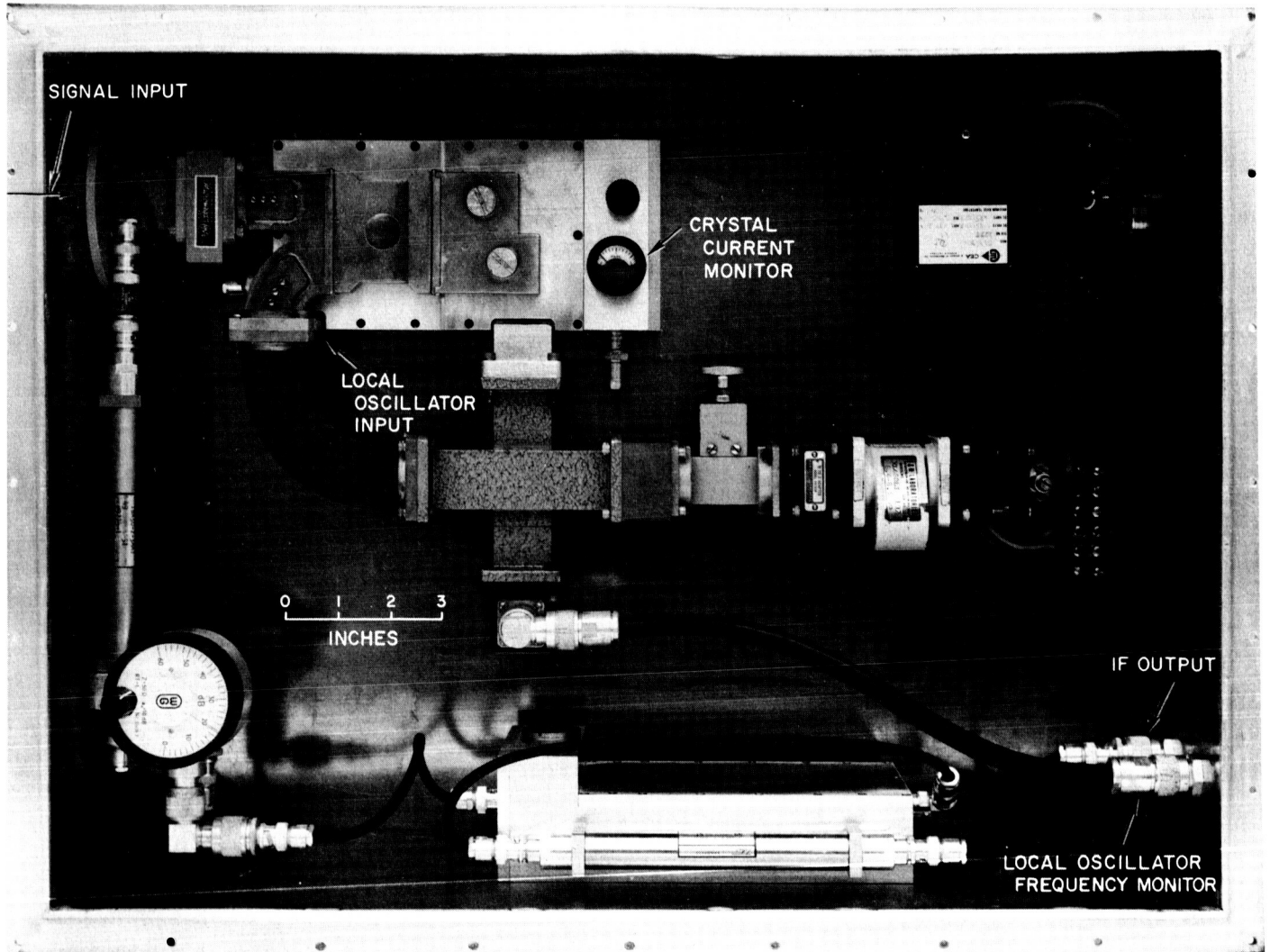
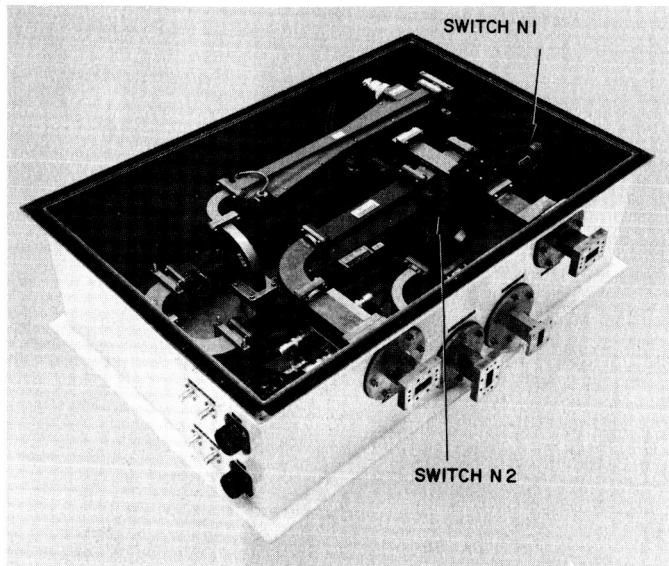
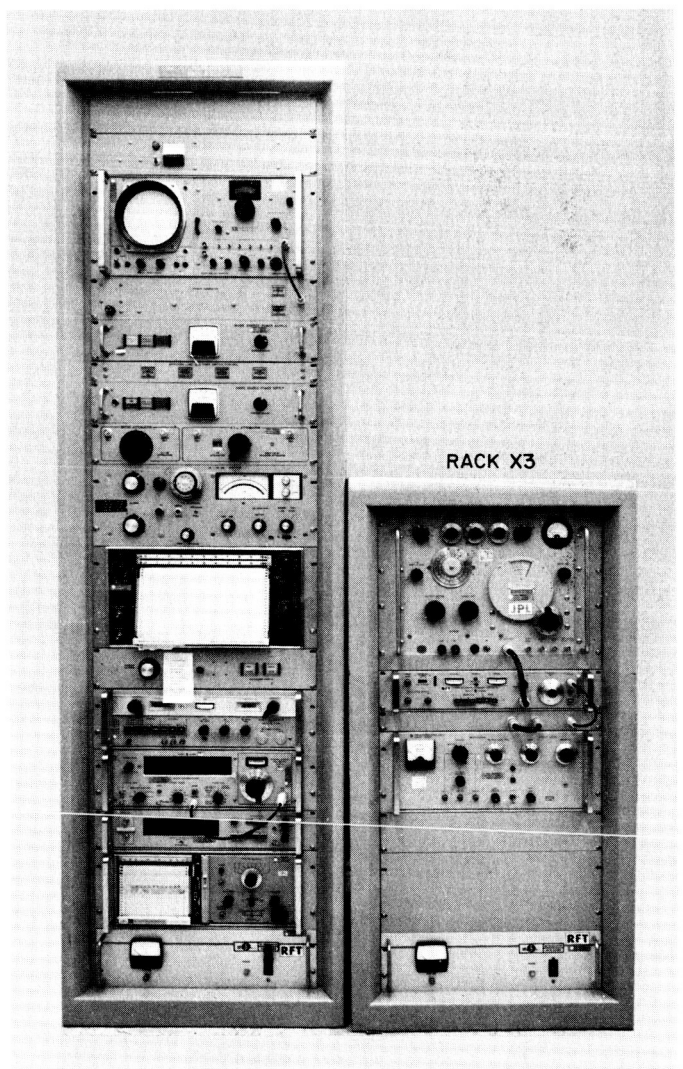


Fig. 31. Photograph of X-band monitor receiver



**Fig. 32. Photograph of X-band noise box**



**Fig. 33. Photograph of Venus station RF instrumentation rack X2 and the X-band cone instrumentation rack X3**

## H. Digital Communication and Tracking: Ranging Measurement, R. C. Tausworthe

### 1. Ranging the Mariner Venus 1967 Spacecraft

*a. Introduction.* In June 1966, NASA's Office of Space Science and Applications approved ranging as a part of the celestial mechanics experiment of the *Mariner Venus 67* mission. Inasmuch as plans had already been made to equip the spacecraft with a turnaround transponder, it remained only to provide a ground system capable of extending measurements out to planetary distances.

The ranging measurements to be made can be taken in two parts:

- (1) The first part consists of ranging the first few million miles of the mission, during which time range measurements can be taken from any of the assigned tracking stations using standard DSIF equipment. This kind of ranging data is of value in improving orbit determination, and thus guidance, and in providing actual system checks with the ranging technique to be used later in the flight when the DSIF standard ranging system thresholds.
- (2) The second part of the ranging mission is to be conducted from Goldstone by R&D personnel and equipment to supplement the DSIF. In addition to improving the tracking accuracy during the latter part of the mission, the ranging data will be very valuable in two other ways: On the one hand, ranging will extend more precise and deep results to the celestial mechanics experiment, for while doppler and range are certainly related, the relationship depends on the details of the gravitational field—the area to be explored. Stating it in another way: doppler and range provide different ways of looking at the situation, and having both permits greater insight. At present, for instance, compatible range/range-rate ephemerides of the planets are non-existent.

The second way in which ranging data is helpful is as a probe of the intervening interplanetary medium. Ranging will provide additional information here because, while doppler measurements are related to the carrier, and thus the *phase* velocity of the signal, ranging is related to modulation, and thus to the *group* velocity of the signal. In a vacuum, the two are supposedly the same, and equal to the speed of light. In a dispersive medium, such as an ionosphere, the two are not the same. Therefore, having

both provides a sensitive way of measuring the dispersive effect, and compensating for it in translating time of flight or doppler into true range.

The experiment will require the 210-ft Mars DSS antenna fitted with a 20-kw transmitter plus a supplement to the existing receiver. It is probable that at least 1 to 1½ hr per pass at DSS 14 will be necessary during the pre-encounter period. Measurements immediately prior to encounter, and as near post-encounter emergence as feasible, are of extreme value in determining the astronomical unit.

This report describes the ranging system in detail, and the ground system mechanization in particular. In summary, however, there is a simple straightforward extension of present ranging techniques which will enable precise turnaround ranging of a spacecraft at planetary distances.

*b. Expected signal and noise parameters near encounter.* Based on an  $80 \times 10^6$  km communications distance along with the nominal transmitter-receiver parameters given in Tables 5 and 6, the spacecraft carrier tracking loop will be operating at about 21.9 db margin, giving about 11 or 12 deg RF phase jitter, and the ground receiver carrier tracking loop will have about 25.7 db margin, or about 7 or 8 deg of jitter. Also as for the ranging sidebands, the S/N into the transponder will be about -19 db and the ground-received ranging power about -172 dbm, giving a total-ranging-power-to-noise-density ratio  $S/N_0$  equal to about 9.6 db.

*c. The ranging equipment.* The R&D receiver ranging supplement consists of two correlation channels and a stored program signal processor, as depicted in Fig. 34. The correlation channels are constructed from modules much like, or the same as, modules in the GSDS receivers. In order to provide IF stability required for the narrow bandwidths involved, the usual free-running reference oscillator in the GSDS receiver is replaced by an atomically derived reference. All the reference frequencies indicated in Fig. 34 are coherently related to an atomic standard, the frequency and timing system (FTS).

The signal processor consists of an SDS-920 general-purpose computer with analog/digital and digital/analog interfaces, supplemented by a number-controlled oscillator (NCO), various digital phases detector, counters, etc.

The automatic feature of the programmed device makes it possible to effect code acquisition and range tracking in

**Table 5. Analysis of a turnaround ranging system**

Uplink		
Ground transmitter	73.0 dbm	20 kw
Transmitting antenna gain	59.5 db	210-ft dish at 2115 MHz
Ranging modulation suppression	- 0.6 db	87% of power in code
Space loss	-256.8 db	80 × 10 <sup>6</sup> km at 2115 MHz
Receiving antenna circuit gain	3.8 db	Low gain at encounter
Spacecraft received ranging power	<hr/> -121.1 dbm	
Receiver noise density	-164.3 dbm/Hz	2700°K noise temperature
Transponder noise bandwidth	62.2 db Hz	3.3 Mc -1.65 MHz baseband
Total spacecraft receiver noise	<hr/> -102.1 dbm	
S/R into transponder	- 19.0 db	
Downlink		
Spacecraft transmitter power	40.0 dbm	10 w
Transmitter circuit loss	- 1.8 db	
Transmitter antenna gain	18.5 db	
Ranging modulation suppression	- 11.0 db	
Limiter suppression	- 21.0 db	P(ranging)/P(limiter output)
Space loss	-258.0 db	80 × 10 <sup>6</sup> km at 2298 MHz
Receiving antenna circuit gain	61.3 db	210-ft dish at 2298 MHz
Ground received ranging power	<hr/> -172.0 dbm	
Receiver noise density	-181.6 dbm	50°K maser
S/N <sub>0</sub> of ranging signal	9.6 db	
Effective tracking bandwidth	- 17.0 db Hz	0.02 Hz
S/N in tracking bandwidth	26.6 db	
Code tracking jitter after acquisition	5.0 m	

the most effective way. For example, minute gain offsets in each channel can be compensated for by switching codes and channels back and forth periodically.

There are seven steps to the acquisition process: (1) the clock is acquired and the clock-tracking loop locked, (2) through (6) each component is acquired, and (7) the entire code is tracked.

**Table 6. Carrier-tracking loop analysis**

Uplink		
Ground transmitter	73.0 dbm	20 kw
Transmitter antenna gain	59.5 db	210-ft dish at 2115 MHz
Carrier suppression	- 8.9 db	13% of power in carrier
Space loss	-256.8 db	80 × 10 <sup>6</sup> km
Receiving antenna circuit gain	3.8 db	Spacecraft low gain at encounter
Spacecraft received carrier power	<hr/> -129.4 dbm	
Receiver noise density	-164.3 dbm/Hz	2700°K noise temperature
Spacecraft receiver design bandwidth	13.0 db Hz	20 Hz
Receiver threshold	<hr/> -151.3 dbm	
Spacecraft carrier loop margin	21.9 db	
Downlink		
Spacecraft transmitter power	40.0 dbm	10 w
Transmitting circuit loss	- 1.8 db	
Transmitter antenna gain	18.5 db	
Carrier suppression	- 5.1 db	
Space loss	-258.0 db	80 × 10 <sup>6</sup> km at 2298 MHz
Receiving antenna circuit gain	61.3 db	210-ft dish at 2298 MHz
Ground received carrier power	<hr/> -145.1 dbm	
Receiver noise density	-181.6 dbm/Hz	50°K maser
Carrier loop design bandwidth	10.8 db Hz	12 Hz
Ground receiver threshold	<hr/> -170.8 dbm	
Ground carrier loop margin	+ 25.7 db	

There are two different tracking modes: the first is an early-late correlation-and-subtraction mode to produce an S-curve, as shown in Fig. 35, used in steps (1) and (7) only. The other mode is RF doppler-aided track during steps (2) through (6). Briefly, it operates as follows:

Both the transmitted frequency and the clock frequency are accurately known, as both are developed from the atomic standard. With the carrier loop locked, the RF doppler detector provides an exact measurement of the incoming clock doppler (except for the slight effects of a dispersive medium), when multiplied by the clock-to-transmitter frequency ratio. It is thus possible, once the

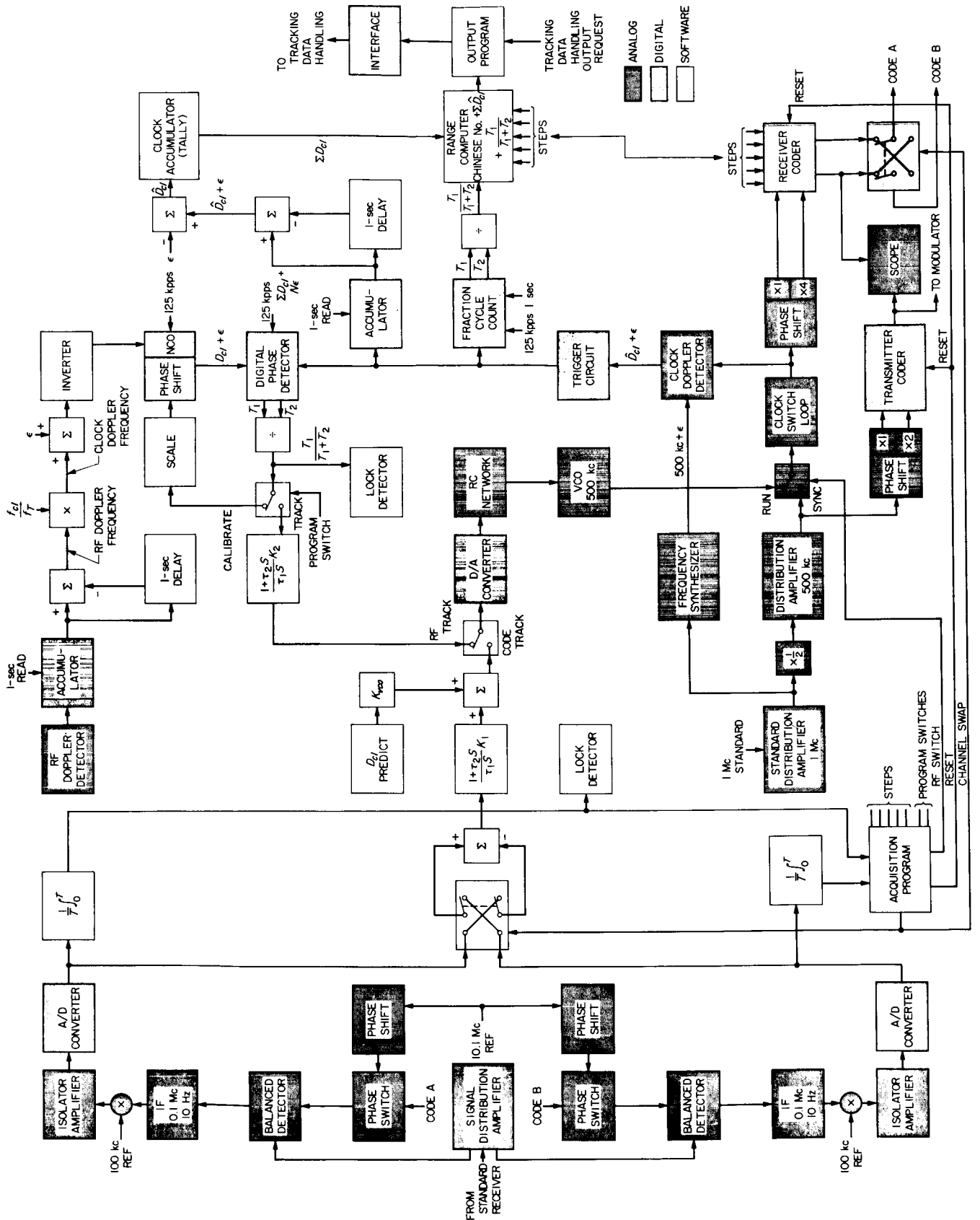


Fig. 34. Mariner 67 Venus ranging equipment

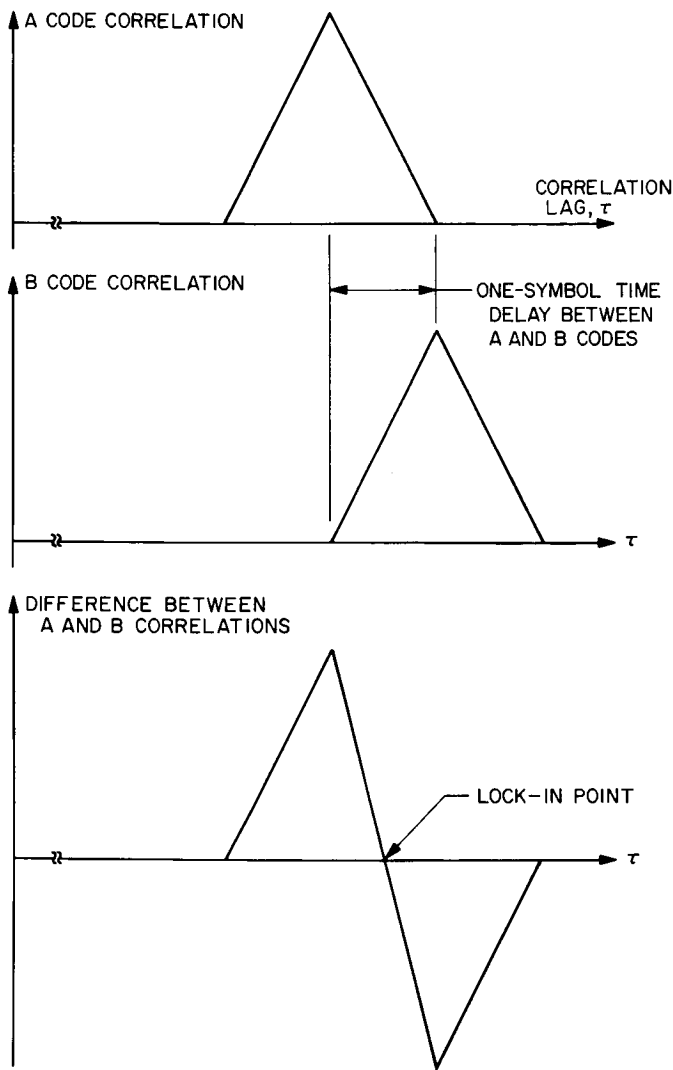


Fig. 35. Early-late correlate-and-subtract scheme to create tracking S-curve

clock component is locked, to cause the receiver clock to vary exactly as it should by making it follow the RF doppler, properly scaled. Charged-particle effects and imprecise  $f_{ci}/f_r$  ratios cause a slight receiver clock drift which can be readjusted periodically as needed by reverting to tracking of the first type.

However, one notes that steps (2) through (6) are accomplished with both early and late channels free for correlation with the incoming code, speeding component acquisition by a factor of two over the one-correlation-channel Mark I system.

The RF doppler can be used during steps (1) and (7) to reduce the steady-state phase error in the code tracking

loop produced by a doppler acceleration, by merely programming the VCO to remove (measured) doppler effect.

During steps (2) through (6), it is necessary to generate a waveform at the correct (computed) clock doppler offset, to which the measured clock doppler can be compared and thus be made to follow. Generation of the clock doppler offset frequency is conveniently done by a number-controlled oscillator (i.e., one whose frequency is set by a number put into it); but there is a practical limit on the lowest frequency it can generate. To eliminate this difficulty at zero and low doppler offsets, a clock doppler bias frequency ( $\epsilon$  in Fig. 34) is coherently inserted, both as an analog frequency into the clock doppler detector and as a known number into the NCO.

*d. Range code components.* The transmitted ranging code is a six-component composite code of the same general type used in the Mark I system. The first of the components is a period-2 series of alternating 0's and 1's, which we hereafter refer to as the clock component. The remaining five components are pseudonoise sequences of length 7, 11, 16, 19, and 23, generated by the recursions listed in Table 7. These are inserted into a majority-vote Boolean function in which tie votes are resolved to produce a balance of 1's and 0's. This balance is necessary to minimize the DC component of the transmitted code. A majority-vote logic is known to maximize the sum of correlations between the transmitted code and each component, and tie votes can then be resolved in such a way as to make these correlations be approximately proportional to the periods of the components, to minimize range acquisition time.

Receiver component codes are duplicates of those transmitted, generated at a rate set by a VCO programmed to track the incoming code rate as described in part c.

During steps (1) through (6) of the acquisition procedure, adjacent phases of the component sequences themselves are inserted into the correlation channels; step (1)—clock acquisition—thus proceeds by early-late tracking as described. At the end of step (1), bit transitions of the incoming transmitted code and those of the clock are displaced 90 deg. During steps (2) through (6), the receiver clock VCO is programmed over 90 deg so that bit transitions are aligned to give the most effective detection. At step (7) the 90 deg shift is removed, and the system again is put into the early-late correlation tracking mode.

*e. Initial range acquisition.* At the start of a run, both the transmitter coder and the receiver coder are run from the atomic-standard 1-Mc code rate, and all code components are synchronized together. Then the receiver coder is switched to its own VCO. From the time this switch occurs until clock acquisition (lock), the two sets of codes may separate in phase in an undetermined manner; however, by monitoring the clock doppler counter (and removing the bias) the exact amount of slip is recorded and thus accounted for. At the end of step (1) (clock acquisition), the receiver coder VCO frequency is the same as that of the incoming code; at the beginning of step (2), there is a fixed integral number of phase-steps separating events of the incoming code with those corresponding ones in the receiver components. Step (2) is thus concerned with correlating the incoming stream with each of the seven possible phases of the second component. This could be accomplished serially by averaging at the first phase for a time  $T$ , recording the value, stepping to the second phase, and repeating the procedure until all seven correlations are obtained. That phase number  $m_2$  having the largest correlation value is regarded as the most probably correct choice, so this component is shifted then  $m_2$  steps to bring the second component into alignment. This could be repeated with all successive components to align all components. With two channels available for correlation, however, the process can be speeded somewhat by obtaining two averages simultaneously.

At the end of acquisition we have, by manipulating each component, moved the code an equivalent of  $M$  steps; we have stored five numbers  $m_2, \dots, m_6$ . At any subsequent time we have available in the computer the accumulated clock doppler count, which indicates the integral number of steps in addition to  $M$ , separating the transmitted and received codes, and we also have the fractional number of clock cycles as a vernier to the clock doppler counter.

*f. The computation of range.* At any desired time after acquisition the integers  $m_i \equiv M \pmod{p_i}$ , the clock doppler count, and the fractional doppler cycle count (or vernier) are available to compute the range. The range in light microseconds is thus given by

$$R = M + \text{doppler count} + \text{vernier}$$

Table 7 shows how  $M$  is computed from each of the numbers  $m_i$ :  $M$  is the linear combination of each  $m_i$  with the coefficients (called "Chinese" numbers because they are a result of the Chinese Remainder Theorem of Num-

Table 7. Ranging code components

Component	Period	Code	Logic
1	2	10...	$x_2 = \bar{x}_1$
2	7	1110010...	$x_4 = x_2 \oplus x_1$
3	11	11100010110...	$x_6 = \bar{x}_2 \bar{x}_5 + \bar{x}_1 \bar{x}_4$ $+ x_1 x_2 \bar{x}_3$
4	15	111100010011010...	$x_5 = x_2 \oplus x_1$
5	19	1111010100001101100...	$\bar{x}_8 = x_1 \bar{x}_2 x_3 + \bar{x}_1 x_2 \bar{x}_3$ $+ x_1 x_3 \bar{x}_4 + \bar{x}_1 \bar{x}_3 x_4$ $+ x_2 x_4 x_5$
6	23	11111010110011001010000...	$\bar{x}_8 = \bar{x}_2 x_3 x_5 + \bar{x}_2 x_4 \bar{x}_5$ $+ x_2 x_4 x_7 + \bar{x}_1 x_3 x_7$ $+ x_1 x_2 \bar{x}_3$
Sum of periods = 77			
Product of periods = 1,009,470			
Chinese Numbers: let total range measurement be $M$ , and $M \equiv m_i \pmod{p_i}$ then $M \equiv 504,735m_1 + 721,050m_2 + 642,390m_3 + 134,596m_4 + 850,080m_5$ $+ 175,560m_6 \pmod{1,069,470}$			

ber Theory) listed. It is interesting to note that, because of the way the clock is acquired,  $m_1$  is always zero in the computation for  $M$ .

## N67-15916 Digital Communication and Tracking: Ranging Subsystem Acquisition Probabilities, R. Diddy

### 1. Introduction

The Mark I ranging subsystem now in use in the Deep Space Network has been previously described (SPS 37-20 through 37-24 and 37-27, Vol. IV). Briefly, the system provides range measurements by detecting the phase shift between a modulating signal generated on the ground and the same signal after return from a vehicle being tracked. Detection of the phase of the received signal is accomplished by correlation techniques. The signals used are binary pseudonoise sequences chosen to have a long period (thus permitting unambiguous measurement of large distances) and yet to have characteristics which allow rapid acquisition (detection).

It is, of course, essential to be able to test the system, and one technique for so doing is based on the behavior of the probability of error in acquisition as a function of the signal to noise ratio (S/N) and the integration time used in correlation. An error occurs when excessive noise causes a particular (wrong) phase position to appear to have the highest correlation of all possible positions, and

thus the occurrence of an error is related to the S/N. The test procedure consists of adjusting the S/N to a desired value, then attempting to acquire the signal from an object at a known range (a collimation tower, for example). A certain number of trials are made, and from the number of successes, the probability of correct acquisition on each trial can be placed within some range. If enough trials are performed, this range is small enough so that this technique provides an adequate measure of the system's performance.

## 2. Acquisition probabilities

To use such a testing procedure, first of all we need to find the relationship between the probability of correct acquisition and the other system parameters. Using the result presented by Viterbi (Ref. 9, p. 120) we have the expression

$$P(\text{correct acquisition}) = P_c = \int_{-\infty}^{\infty} \left[ \frac{\exp(-\mu^2/2)}{(2\pi)^{1/2}} \right] \times \left[ \int_{-\infty}^{\mu + (2ST/N_0)^{1/2} \frac{\exp(-v^2/2)}{(2\pi)^{1/2}} dv} \right]^{M-1} d\mu$$

for an orthogonal, single component code. In this expression,  $S$  is the signal energy,  $T$  is the integration time per phase position,  $N_0$  is the noise power single-sided spectral density, and  $M$  is the period of the code. Since in the case we wish to analyze we do not have an orthogonal code, we must alter this expression. The nonorthogonality of the code we are using results in smaller changes in the correlation levels obtained, so the effective signal power is decreased by a factor of the square of the difference in the maximum and the minimum correlation observed. Making this substitution, and using the definition

$$\operatorname{erf}\left(\frac{x}{(2)^{1/2}}\right) = \int_0^x \frac{1}{(2\pi)^{1/2}} e^{-t^2/2} dt$$

the expression reduces to

$$P_c = \int_{-\infty}^{\infty} \frac{\exp(-\mu^2/2)}{(2)^{1/2}} \times \left\{ \frac{1}{2} \left[ 1 + \operatorname{erf}\left(\frac{\mu + \left(\frac{2ST}{N_0}\right)^{1/2} (C_{max} - C_{min})}{(2)^{1/2}}\right) \right] \right\}^{M-1} d\mu$$

where  $C_{max}$  and  $C_{min}$  are the appropriate values of the correlation. Making the substitution  $x = \mu/(2)^{1/2}$  we obtain

$$P_c = \frac{1}{(\pi)^{1/2}} \int_{-\infty}^{\infty} e^{-x^2} \times \left\{ \frac{1}{2} \left[ 1 + \operatorname{erf}\left(x + \left(\frac{ST}{N_0}\right)^{1/2} (C_{max} - C_{min})\right) \right] \right\}^{M-1} dx.$$

This expression may be evaluated given the value of  $ST/N_0$  and the characteristics of the code.

In the Mark I subsystem there are two different codes: (1) the normal (or long) code and (2) the short code. Each of these is of the form

$$xcl + \bar{x}[(ab + bc + ac) \oplus cl],$$

where  $x$ ,  $a$ ,  $b$ , and  $c$  are pseudonoise sequences with specified periods and  $cl$  clock is a component of 2-bit length. The clock component is acquired by locking the receiver loop, and does not enter into the correlation process. To discover the overall probability of correct acquisition it is necessary to compute the product of the probability of correct acquisition for each component. The effect of the different receiver codes generated by the different program states (Ref. 10) is taken into account by the values used for the maximum and minimum correlations.

These calculations have been made for both the long and the short code, using an IBM 1620 computer. Curves of probability of error ( $=1 - P_c$ ) versus  $ST/N_0$  (where  $T$  is the integration time per code component phase position) are shown in Figs. 36 and 37. The results obtained are believed to be correct to four significant figures, and this limit is imposed only because rather large intervals were used in the numerical integration. Using more computer time, more precise answers could easily be obtained, since the rest of the computation is accurate to six significant figures. The values used for  $C_{max}$  and  $C_{min}$  were taken from Ref. 11, p. 19.

By performing a suitable mapping, it is possible to obtain curves of the total acquisition time versus  $S/N_0$  (sideband power-to-noise-density ratio) with the probability of error as a parameter. For example, from Fig. 36 we note that for  $P(\text{error}) = 0.001$ ,  $ST/N_0 = 374$ . Thus, a plot of  $T$  (time per phase position) versus the ranging

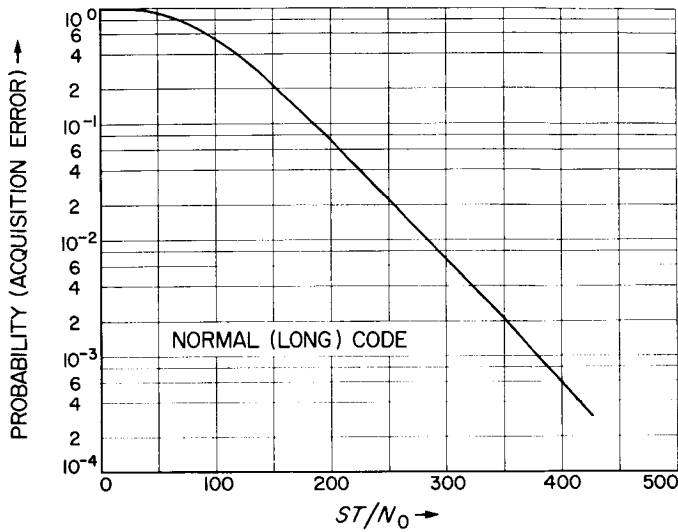


Fig. 36. Probability of error in acquisition for long code

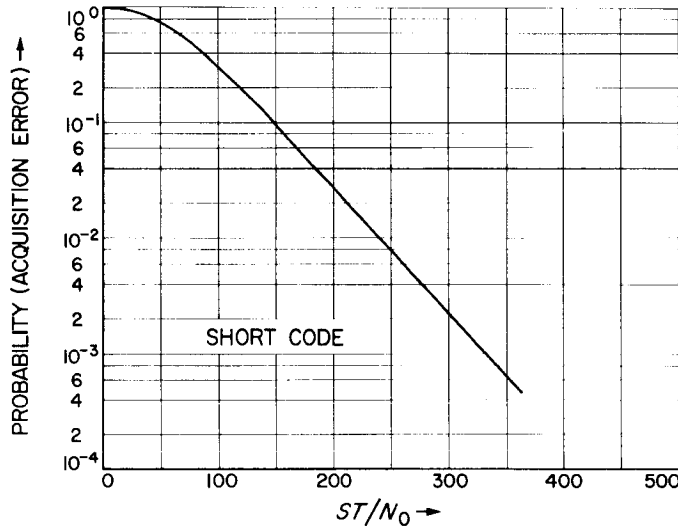


Fig. 37. Probability of error in acquisition for short code

signal-to-noise-density ratio is the hyperbola (or straight line on a log-log plot) given by  $(S/N_0) = 374/T$ . Total acquisition time for the normal code is calculated from  $T$  as  $232 \times T + 1.59$  sec, since there are 232 (the sum of the component periods for the long code) phase positions, and there is a 1.59-sec period required for the system to operate (Ref. 12, pp. 26-28). Plots obtained by this technique are shown for various probabilities of error for both the long code (Fig. 38) and the short code (Fig. 39). Given the signal-to-noise ratio, from these plots it is possible to determine the time required for acquisition with a particular probability of error.

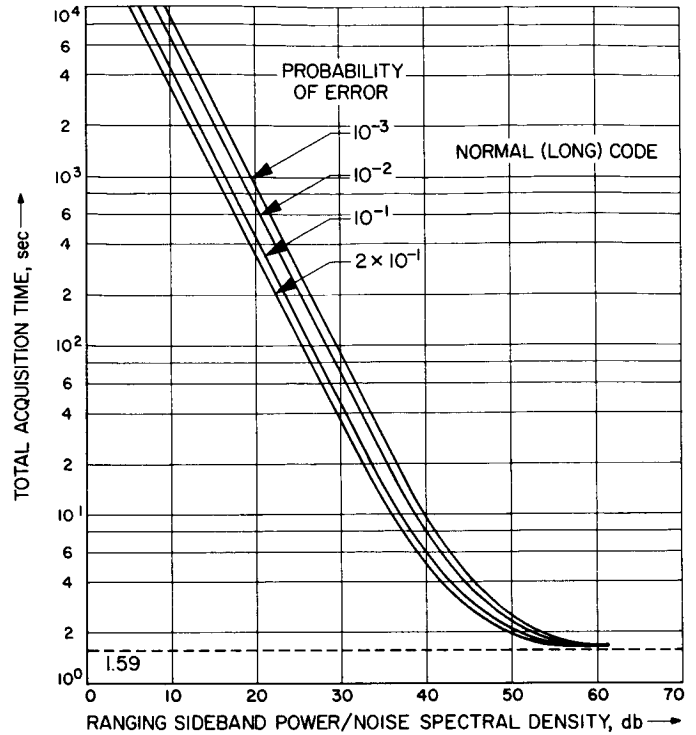


Fig. 38. Long code acquisition time

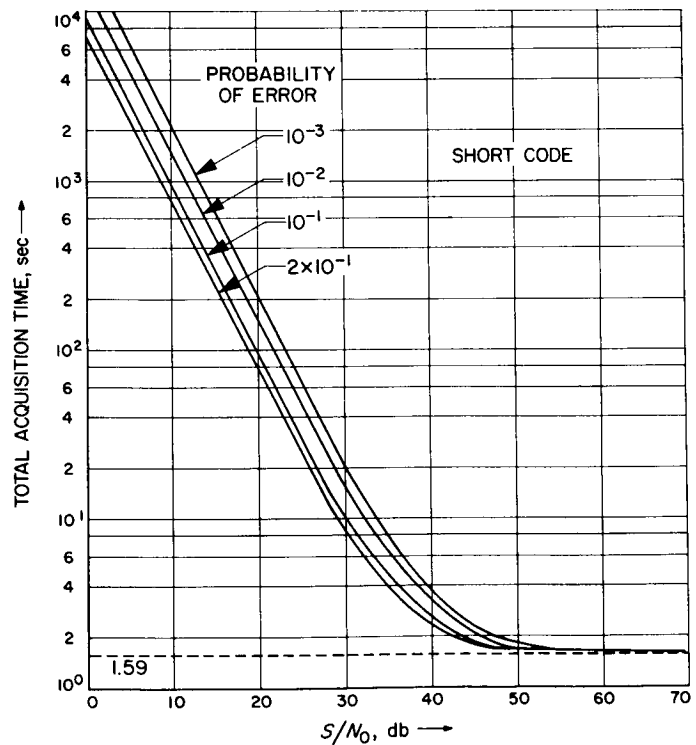


Fig. 39. Short code acquisition time

### 3. Estimation of P (correct acquisition)

Next, we wish to be able to relate a certain number of successes in a given number of trials to a range of values which probably includes the actual probability of correct acquisition on each trial. That is, we wish to find a confidence interval on  $P_c$ , the probability of correct acquisition. To do this, we note that the number of successes in  $n$  trials is governed by the binomial distribution, that is, the probability of  $k$  successes in  $n$  trials given that the probability of success on each trial is  $P_c$ , is

$$\binom{n}{k} (P_c)^k (1 - P_c)^{n-k} = \frac{n!}{k!(n-k)!} (P_c)^k (1 - P_c)^{n-k}.$$

However, our problem is somewhat the inverse of this. What we wish to know is some estimate of the value of  $P_c$  given that  $k$  successes were observed. Specifically, we wish to find some  $P_1$  and  $P_2$  so that

$$P \{P_1 < P_c < P_2\} = 0.95.$$

We can do this by forcing  $P_1$  and  $P_2$  to satisfy the requirements

$$P \{k \leq k_0 | P_1\} = 0.025$$

$$P \{k \geq k_0 | P_2\} = 0.025$$

where  $k_0$  is the number of successes actually observed in the total number of trials (Ref. 13).

We know the distribution of  $k$  given  $P_1$ , so we can write these two expressions explicitly as

$$\sum_n^k \binom{n}{k} (P_1)^k (1 - P_1)^{n-k} = 0.025$$

$$\sum_{k=k_0}^n \binom{n}{k} (P_2)^k (1 - P_2)^{n-k} = 0.025.$$

Solutions for various values of  $k_0$  are accomplished by use of tables of the binomial distribution (Ref. 14). A table of the results for one case of interest ( $n = 10$  and  $k_0 = 6, 7, 8, 9, 10$ ) is shown in Table 8.

These limits on  $P(\text{error in acquisition})$  may be mapped onto the curves of Figs. 38 and 39 to produce a chart which is of use in testing the ranging system. A sample of such a plot, done for 8 successes is shown in Fig. 40.

Table 8. Acquisition confidence testing

Number of successes observed in 10 trials	95% confidence limits on $P(\text{correct acquisition})$		Limits on $P(\text{error in acquisition})$	
6	0.2650	0.8786	0.1214	0.7350
7	0.3475	0.9336	0.06640	0.6525
8	0.4439	0.9752	0.02480	0.5561
9	0.5548	0.9965	0.00346	0.4452
10	0.6914	1.0	0.0	0.3086

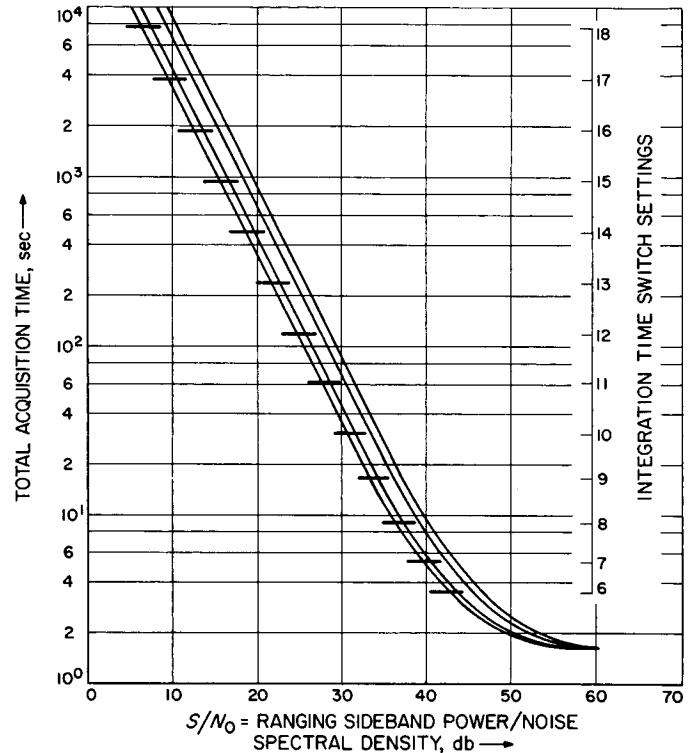


Fig. 40. Operating regions (95% confidence) for eight successes observed in ten trials

The proper interpretation of this graph is that given a particular time switch setting, and given that 8 correct acquisitions were observed out of ten trials, then the probability is 0.95 that the system is operating within the interval (bar) shown. This interval represents about an order of magnitude change in the probability of error but corresponds to only 3 or 4 db in  $S/N_0$ . Thus, the operating point is fairly well specified.

One method of using a curve such as this would be to select a time switch setting (thus fixing the total acquisition time), and then attempt to acquire an object at known range after causing  $S/N_0$  to assume some desired

value. For instance, suppose we had selected time switch setting 10, had caused the signal-to-noise ratio to be 30.8 db, and had obtained 8 successes. We would note from Fig. 40 that with 95% confidence, the operating point of the system is in the interval shown (which runs from  $S/N_0 = 28.83$  to 32.87 db). We would conclude in this case that the system is functioning properly. If we had obtained some other number of successes, a plot similar to Fig. 40 would have been used to determine if the system seemed to be operating in the proper region.

#### 4. Remarks and Summary

Briefly, a technique has been developed which allows quick computation of the probability of correct acquisition in a ranging system. Information concerning the transmitter and receiver codes must be obtained in the form of length of the period of each component and the change in correlation before and after that code has been acquired. Using these probability functions, it is possible to determine if a particular system is operating properly by making a number of trials under known conditions of signal-to-noise ratio and range. Although the results presented here are specifically for the Mark I ranging subsystem, the programs used to obtain these results are general enough to allow similar results to be quickly obtained for future ranging codes.

in which  $m$  is the receiver margin above loop design signal power level  $P_0$ ,  $\rho_0$  is the SNR in the receiver pass-band  $w_{L_0}$  Hz wide at this power level,  $\rho_0 = P_0/kT w_{L_0}$ ,  $w_{L_0}$  is the two-sided *linear theoretic value* of loop bandwidth at design point,  $w_{L(eq)}$  is the actual equivalent loop bandwidth,  $\Gamma$  is a limiter performance factor, and  $\gamma^2$  is a parameter relating to nonlinear operation of the loop. Both  $w_{L(eq)}$  and  $\gamma^2$  are functions of the parameter  $a^2$ , so Eq. (1) is transcendental. The program uses Newton's method to find solutions for  $a^2$  both in the carrier and clock loops. For the clock loop,  $\gamma^2$ ,  $w_{L(eq)}$ , etc. are functions of  $a^2_{carr}$  which is thus determined first.

Once the  $a^2$  are found, they are related to the phase error variance by an approximate formula

$$\sigma^2 = \frac{\pi^2}{3} \left\{ 1 - \exp \left[ - \frac{3a^2}{\pi} (1 + 0.13a^2) \right] \right\}. \quad (2)$$

The remainder of the loop performance parameters follow by mere substitution (Ref. 9).

#### 3. The Program

The program was FORTRAN-compiled, using SDS series 900 FORTRAN II from which a paper tape dump was made, suitable for either the SDS 930 or SDS 920 without further modification. It would be a simple matter to recompile and dump to provide an SDS 910 program. The tape is entered into the machine by a "standard fill."

Upon completion of the fill, control is automatically given to the program, causing the typewriter output

TYPE OUT ANALYSIS — CARRIER LOOP,  
CLOCK LOOP, OR BOTH

whereupon the operator responds *CARRIER*, *CLOCK*, or *BOTH*. The computer then asks for the computer configuration in carrier and clock loops, and for the type numerical data to be given it. The last can be either *DESIGNED*, *MEASURED*, or *THEORETIC* parameters.

#### 4. Parameters

Values called for by the analysis are:

$WLO = W_{L_0}$ , loop linear theoretic  
two-sided bandwidth at  
design point, Hz

$$a^2 = \frac{1}{2\rho_0 m} \left( \frac{w_{L(eq)}}{w_{L_0}} \right) \left( \frac{\Gamma}{\gamma^2} \right) \quad (1)$$

67 15917

### J. Digital Communication and Tracking: a Phase-Locked Receiver Analysis Program, R. C. Tausworthe

#### 1. Introduction

A receiver analysis program to present a profile of a receiver's phase noise and loop parameters under operating conditions was reported in *SPS 37-38*, Vol. III, pp. 29-33. In *SPS 37-40*, Vol. IV, pp. 219-225, a method was presented for the cascade analysis of Mark I ranging system clock loop jitter. The present article describes a program operable on an SDS-920 or SDS-930 for analysis or design of either or both of the carrier-tracking and clock-tracking loops of a DSIF receiver.

#### 2. Loop model

The nonlinear theory of loop operation which this program embodies is developed in Refs. 8 and 9; the more interested reader is referred to these for detailed information. Basically, the program solves an equation

$DAMPFAC(LIN) = \xi_0$ , the loop linear theoretic damping factor at design point

$T2 =$  numerator time constant of loop filter, sec  
 $= \tau_2$

$T1 =$  denominator time constant of loop filter, sec  
 $= \tau_1$

$BH =$  predetection one-sided bandwidth, Hz  
 $= w_H/2$

$MARGIN =$  starting value of analysis, db  
 $= m$

$\Delta MARGIN =$  difference in margin between steps, db

$TMP =$  noise temperature, °K

$P/PTOT =$  ratio of power in carrier (clock) channel to total power, db

$PO/KTWLO = \rho_0$ , the design point SNR, db

$LOOP\ GAIN = \begin{cases} K & (1/v\text{-sec, simple loop}) \\ K_a K_{vco} MF & (1/sec, limiter loop) \end{cases}$

$CORR\ MAX =$  value of clock-loop correlation when a particular component is acquired (absolute)

$CORR\ MN =$  value of clock-loop correlation when that particular component is unacquired (absolute)

## 5. Output

A typical computer run is shown in Fig. 1. Most of the quantities are self explanatory. The phase error is printed in degrees, radians and radians-squared, both actual value, and linear-theoretic value. The limiter performance factor ( $LIM.PER.FAC$ ), or  $\Gamma$ , is shown, and the limiter suppression factor  $\alpha$  is also given.

## 6. Cautions

To eliminate as much operator failure as possible, several error checks were put into the program. Some things of note are:

- (1) False input characters recognized:

[BOTF]  
NOT ACCEPTABLE RESPONSE, MESSAGE IGNORED

- (2) To restart, put machine in *IDLE*, press *START*, then *STEP-IDLE-RUN*. Also can be done by manual branch to cell 03507.

- (3) Only the first four letters of assignment words are recognized, although nominally these are given as: *INCLUDED*, *EXCLUDED*, *SIGNAL*, *NOISE*, *DESIGN*, *MEASURED*, *THEORETIC*, *CARRIER LOOP*, *CLOCK LOOP*, *BOTH*.

- (4) When analyzing the carrier loop only, at the end *ANALYSIS COMPLETE* is typed. If *BKPT 1* is *down*, the entire program is reinitiated. If *BKPT 1* is *up*, the program only asks for a new set of parameters.

- (5) When analyzing the clock loop, the computer asks for a new *CORR MAX* and *CORR MN*, to complete the ranging profile. Only the clock loop performance is printed subsequently.

**N67 15918**

## K. Digital Communication and Tracking: Time Synchronization Experiment, W. Martin

### 1. Introduction

The following article discusses the results of time synchronization experiments conducted with several DSN stations. Over a two-day period the Mark I ranging system accurately measured time offsets between paired stations. The resulting clock errors were later verified when the Naval Observatory independently calibrated the stations' clocks.

### 2. Experiment

Orbit calculations for the *Lunar Orbiter* spacecraft placed stringent requirements on the timing accuracy of the DSN. Whereas previously it had been adequate to synchronize two stations to within 10 msec, now it became necessary to calibrate the station clock offset to better than 50  $\mu$ sec.

A new synchronization method was devised for which a tabulation of possible error sources showed the worst-case uncertainties to be substantially below 10  $\mu$ sec (Ref. 17). The new idea utilized the existing Mark I ranging system and a spacecraft, thereby realizing substantial cost savings over competing methods.

Time synchronization tests were conducted on August 16 and 17, 1966. Three stations participated in the experiment: DSS 12, DSS 41, and DSS 61. Each test consisted

SECOND-ORDER PHASE-LOCKED RECEIVER ANALYSIS

CARRIER LOOP WITH LIMITER, SIGNAL VARIATION  
 CLOCK LOOP WITHOUT LIMITER, NOISE VARIATION

INITIAL PARAMETER VALUES

CARRIER LOOP--

T1,SEC	= 5.351E 02	WL0,CPS=	1.200E 01	KTWL0,DBM	--170.821
T2,SEC	= 1.249E-01	BH,CPS	= 2.000E 03	P0/KTWL0,DB=	.000
LOOP GAIN	= 1.000E 06	R0	= 1.999E 00	IF SNR,DB	= -22.219
ALPHA0 OR A0=	6.852E-02	T2/T1-Z=	2.335E-04	P/PTOT,DB	= -3.000
TEMP, DEG K	= 5.000E 01			KT,DBM/CPS	--181.612

CLOCK LOOP--

T1,SEC	= 1.482E 02	WL0,CPS=	1.000E 00	KTWL0,DBM	--181.612
T2,SEC	= 1.482E 00	BH,CPS	= 2.000E 03	P0/KTWL0,DB=	.000
LOOP GAIN	= 5.084E 12	R0	= 1.979E 00	IF SNR,DB	= -33.010
ALPHA0 OR A0=	2.627E-11	T2/T1-Z=	1.000E-02	P/PTOT,DB	= -3.000
MX CORR VAL	= 1.000E 00	MN CORR=	.000E 00		

RECEIVER PERFORMANCE

CARRIER LOOP--10.000

SIGNAL LEV,DBM--	160.821	WL[LIN],CPS	= 2.901E 01	ERR[ACT],DEG=	2.201E 01
LOOP MARGIN,DB=	10.000	WL[ACT],CPS	= 2.726E 01	ERR[ACT],RAD=	3.841E-01
P/KTWL[ACT],DB=	6.437	DAMPING[LIN]=	1.250E 00	ERR[ACT],RSQ=	1.475E-01
P/KTWL[LIN],DB=	6.166	DAMPING[ACT]=	1.206E 00	ERR[LIN],RSQ=	1.209E-01
IF SNR, DB	= -12.219	LIM.PER.FAC.=	1.129E 00	ALPHA OR A	= 2.142E-01

CLOCK LOOP--10.000

SIGNAL LEV,DBM--	181.612	WL[LIN],CPS	= 1.000E 00	ERR[ACT],DEG=	4.604E 00
LOOP MARGIN,DB=	19.206	WL[ACT],CPS	= 9.695E-01	ERR[ACT],RAD=	8.035E-02
P/KTWL[ACT],DB=	19.324	DAMPING[LIN]=	7.070E-01	ERR[ACT],RSQ=	6.456E-03
P/KTWL[LIN],DB=	19.336	DAMPING[ACT]=	6.867E-01	ERR[LIN],RSQ=	5.825E-03
IF SNR, DB	= -13.805	LIM.PER.FAC.=	1.000E 00	ALPHA OR A	= 2.627E-11

CARRIER LOOP--15.000

SIGNAL LEV,DBM--	155.821	WL[LIN],CPS	= 4.722E 01	ERR[ACT],DEG=	1.505E 01
LOOP MARGIN,DB=	15.000	WL[ACT],CPS	= 4.577E 01	ERR[ACT],RAD=	2.626E-01
P/KTWL[ACT],DB=	9.186	DAMPING[LIN]=	1.643E 00	ERR[ACT],RSQ=	6.897E-02
P/KTWL[LIN],DB=	9.051	DAMPING[ACT]=	1.615E 00	ERR[LIN],RSQ=	6.222E-02
IF SNR, DB	= -7.219	LIM.PER.FAC.=	1.070E 00	ALPHA OR A	= 3.702E-01

Fig. 41. Phase-locked receiver analysis program output

of measuring the time offset between two of these stations. Three tests provided experimenters<sup>5</sup> with sufficient data to compute an "error of closure," providing a validity measurement on the system.

The paired stations made two sets of ten measurements, one set with each station transmitting. A uniform set, based on consistency, was culled from each original set of twenty. Corresponding readings from each station were examined to determine the measured time difference between the two stations and the spacecraft. This result was compared with the expected time difference as computed by the Orbit Determination Program. Results are found in Figs. 42, 43, and 44 and represent the time offsets between the respective station clocks.

Improper setting of the counter trigger level at DSS 61 during the tests caused a small time measurement

<sup>5</sup>W. Martin and F. Borncamp.

bias. DSS 61 personnel set their counter to start on the trailing-edge of the 1-sec time tick rather than on the desired leading edge. The problem is illustrated in Fig. 45. During the first half of the DSS 61 and DSS 41 tests the threshold level control was set on a relatively steep part of the trailing edge. A change in this setting prior to the second half caused the counter to be started earlier, where the change of voltage with time was not so great. The effect can be seen as a larger variation in the measured time during the latter set of data (Fig. 42). This is understandable when one remembers that the counter is started when a specific voltage is reached. Thus, a lower rate of change of voltage with time affords more opportunity for noise to influence the measurement.

The effect is further illustrated in Fig. 43 (the DSS 41 and DSS 61 tests). Here the counter's threshold was set on a relatively steep part of the timing pulse. The result was highly consistent data whose RMS variation was less than 0.3  $\mu\text{sec}$ .

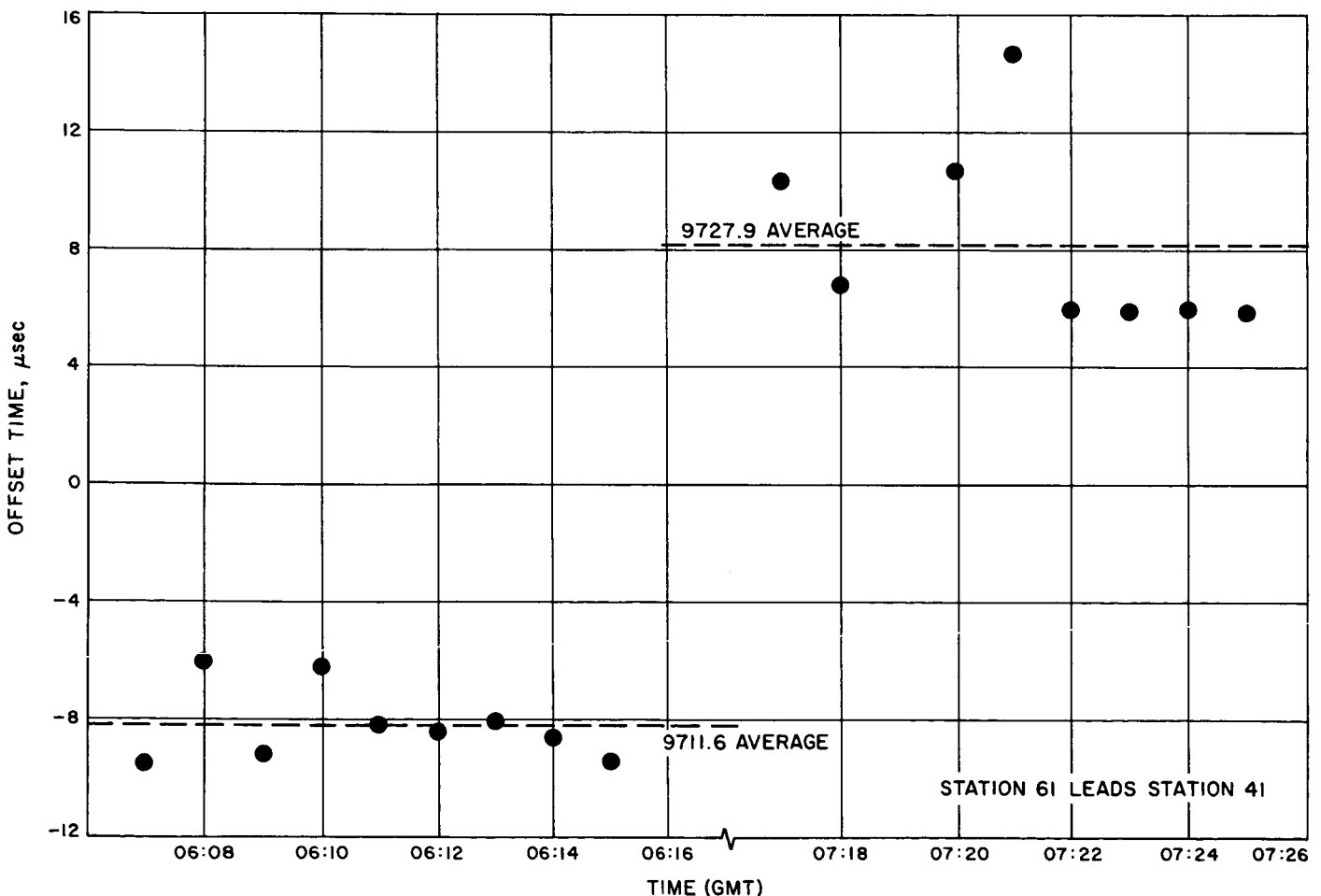


Fig. 42. Time synchronization Stations 41 and 61, August 16, 1966

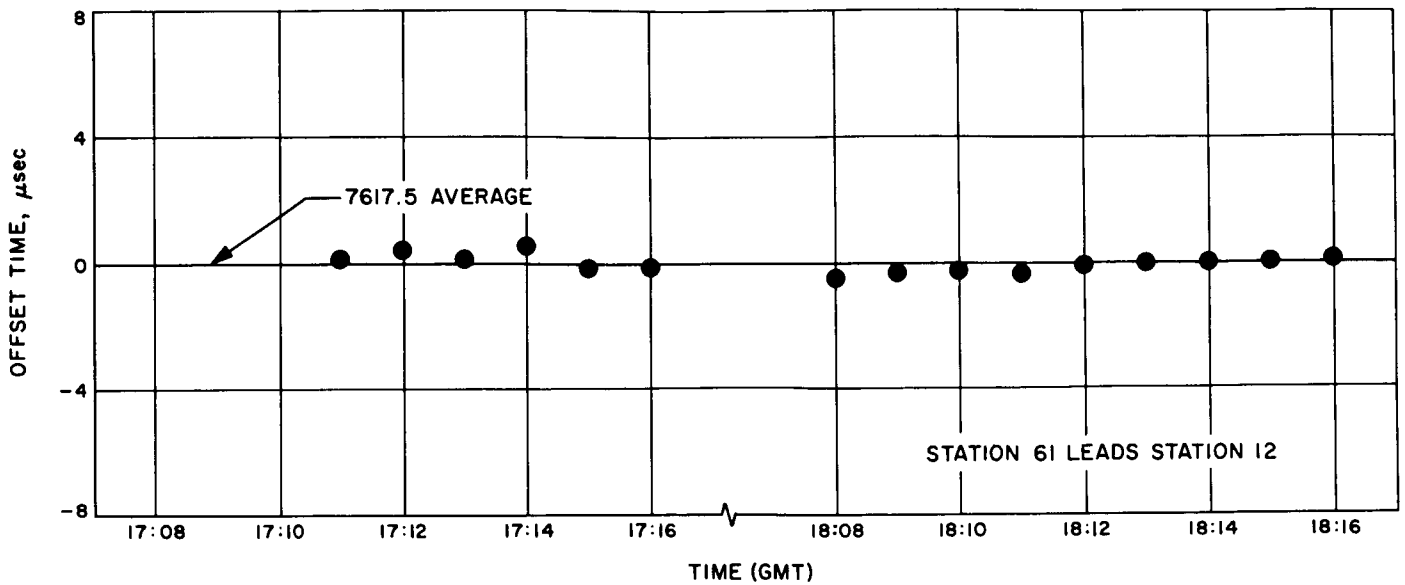


Fig. 43. Time synchronization Stations 12 and 61, August 16, 1966

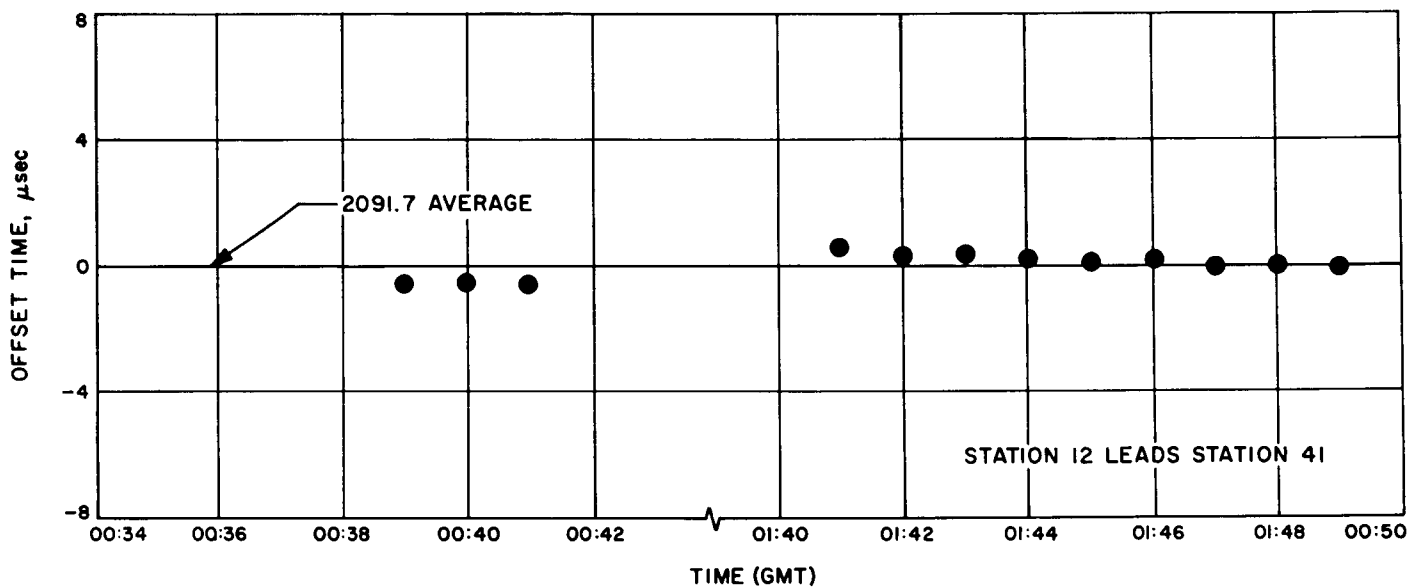


Fig. 44. Time synchronization Stations 12 and 41, August 17, 1966

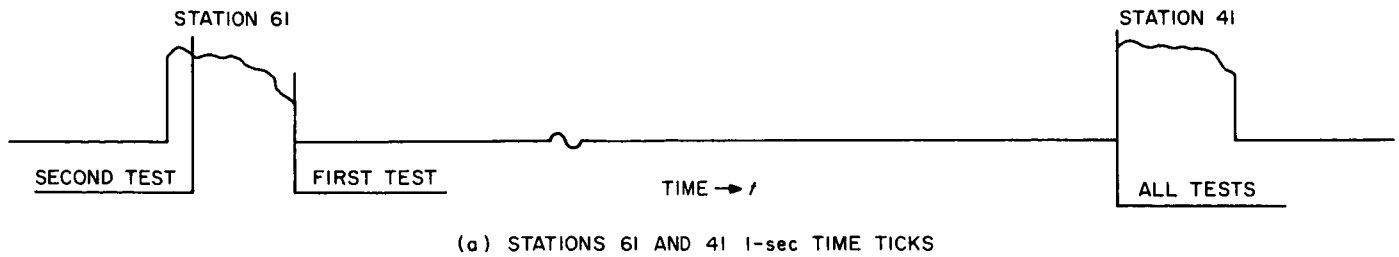
Figs. 44 and 45 represent more typical sets of data. From these it is obvious that the time synchronization scheme can produce results which are consistent to better than  $0.5 \mu\text{sec}$ . Possible instrumentation biases notwithstanding, the data suggests that the technique is very accurate.

Clock offsets together with RMS variations are shown in Table 9 for the three experiments. Due to frequency

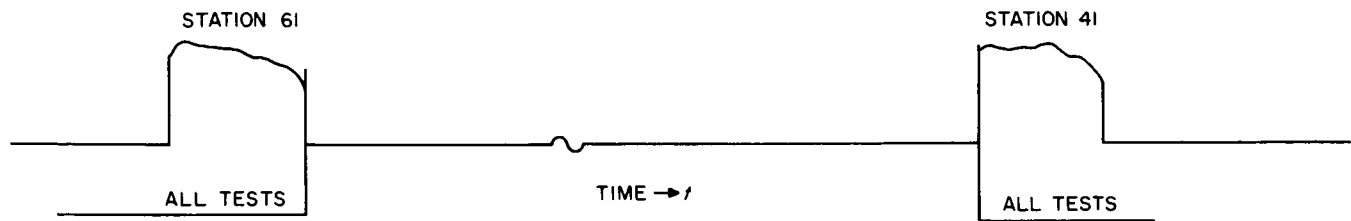
Table 9. Ranging time synchronization test results

Day	Time, GMT	Stations	Time offset, $\mu\text{sec}$	RMS variation, $\mu\text{sec}$
228	07:00	41 and 61	9731.6 <sup>a</sup>	1.27
228	18:00	61 and 12	-7637.5	0.28
229	01:00	12 and 41	-2091.7	0.39

<sup>a</sup> Correction based on first (trailing edge) measurement.



(a) STATIONS 61 AND 41 1-sec TIME TICKS



(b) STATIONS 61 AND 12 1-sec TIME TICKS

**Fig. 45. Counter starting points**

drifts in the rubidium standards, these offsets are valid only at the stated times and cannot be used to compute the "error of closure" (a matter to be considered later). In the cases where DSS 61 participated, the time differences have been corrected to the value that would have been obtained had the counter been triggered properly. The correction is based upon pulsewidth information supplied by the station.

Considering the variation in the data (Table 9) the ranging time synchronization scheme should produce resolutions well below  $1 \mu\text{sec}$ . This level should be attainable when the procedure becomes more familiar to the operators. Thus, the only uncertainties in the computed offsets should be due to differences in the ground equipment's signal processing time. Even the most pessimistic estimates of the delay time difference place this figure well below a microsecond.

One can test the validity of the synchronization scheme by summing the measured time offsets between stations throughout the DSN. A correction must be applied to the measurements in Table 9 to compensate for frequency drifts in the stations' master oscillators. These corrections are equivalent to adjusting all synchronization measurements to a common time (18:00 GMT on Day 228). Data relevant to oscillator drift was supplied by the Naval Observatory in an independent, but concurrent, time synchronization experiment.

Table 10 shows the required corrections together with the adjusted offsets. Algebraically summing these time offsets yields an "error of closure" of  $0.5 \mu\text{sec}$ . One's enthusiasm for the result must be tempered by a knowledge of the uncertainty in the DSS 61 data. However, it seems probable that the offsets are accurate to within a few microseconds.

**Table 10. Adjusted ranging time synchronization test results**

Day	Time, GMT	Stations	Correction, $\mu\text{sec}$	Time offset, $\mu\text{sec}$
228	18:00	41 and 61	-1.6	9730.0
228	18:00	61 and 12	0	-7637.5
228	18:00	12 and 41	+1.3	-2093.0
Error of closure				-0.5

A further check on the ranging time synchronization experiment was provided by an independent station clock calibration. The Naval Observatory, acting under contract to the *Lunar Orbiter* Project, circulated a cesium clock throughout the DSN immediately following the ranging tests. Both time and frequency errors were measured relative to the primary cesium standard. Frequency measurements were made over a period of several hours

**Table 11. Station clock calibration by Naval Observatory**

Day	Time, GMT	Station	Time synchronization error, $\mu\text{sec}$	Frequency error	Drift rate, $\mu\text{sec/day}$
229	12:00	12	157.4 lags	$1.74 \times 10^{-11}$ fast	1.50
232	19:40	61	7482.9 leads	$3.02 \times 10^{-11}$ fast	2.61
237	09:00	41	2189.7 lags	$7.00 \times 10^{-11}$ fast	6.04

to eliminate short-term variations in the cesium clock. Test results are summarized in Table 11.

To facilitate a comparison with the ranging data, the Naval Observatory measurements have also been adjusted to 18:00 GMT on Day 228 (Table 12). The right-most column in Table 12 indicates the discrepancy between the Naval Observatory and the ranging time synchronization calibrations. In each case the ranging method produced larger offsets. There appear to be three reasons for the differences: (1) the basic uncertainties as outlined in Ref. 17; (2) the irregularity in the DSS 61 measurements; (3) the assumption that the rubidium clock's drift rates are constant, in adjusting both sets of data to a common time. This is unlikely, particularly in the case of DSS 41, where the drift rate is large and the adjustment interval long (almost nine days). Past experience with rubidium vapor oscillators together with the literature (Ref. 18) indicates that the frequency stability of these units is on the order of 1 part in  $10^{11}$ . Thus, both the time separating the calibrations and the frequency variation could account for a large part of the discrepancy.

### 3. Data Processing

A computer program has been written for reducing the time synchronization data. This program is capable of accepting inputs from up to three stations simultaneously. In addition to computing the offset between paired stations, the program also corrects for inaccuracies in the counter time base oscillator and for the nonuniform arrival of the code marker pulses.

A simple calibration procedure was devised to measure the frequency error in the counters' time base oscillator. The internal standard is counted between two 1-sec time ticks generated by the station's frequency and timing system. Were the frequency correct, the resulting number would be precisely 10,000,000. To the extent that it

differs from that amount the error is known. Present plans call for this measurement to be made at each station just prior to a time-synchronization experiment. The counter calibration number is processed along with the data and is used to individually correct the time-interval measurements from each station.

Range predicts are available at 1-min intervals from the Orbit Determination Program. Since these are valid only on the minute, a range correction must be made for the arrival time of the code-marker pulse. In some cases this delay can be as much as 2.5 sec. Failure to make an adjustment can cause serious errors in the predicted time difference between stations. The error's magnitude will be determined by the code-marker pulse arrival time and the station-spacecraft geometry.

Lagrange's interpolation formula is used to compute the correct range (Ref. 19).

$$R(t) = R_j + r(\Delta R_j) + \frac{r(r-1)}{2!} (\Delta^2 R_j) + \frac{r(r-1)(r-2)}{3!} (\Delta^3 R_j)$$

where

$$r = \frac{u}{k} \text{ will generally lie in the range } (1 < r \leq 2)$$

and

$u$  = time interval from first predict to arrival of code marker pulse

$k$  = predict time interval

$R(t)$  = interpolated range at time  $t$

$R_j$  = range corresponding to earlier of four predict times

$\Delta R_j$  = first difference between earliest pair of predicts

$\Delta^2 R_j$  = second difference between first three predicts

$\Delta^3 R_j$  = third difference between all four predicts

Four range predicts are required for each interpolation. To minimize errors, the program selects a pair on either side of the desired time. These adjusted ranges form the basis for computing the difference in signal arrival times between the various stations.

**Table 12. Adjusted Naval Observatory time synchronization results**

Day	Time, GMT	Stations	Time offset, $\mu\text{sec}$	Difference ranging—Naval Observatory, $\mu\text{sec}$
228	18:00	41 and 61	9714.1	15.9
228	18:00	61 and 12	-7630.7	6.8
228	18:00	12 and 41	-2083.4	9.6

The program is presently being run on an SDS 930 computer. Required inputs are the predicted station-spacecraft range, the time interval measurements, and the counter oscillator correction number. Entry is made via punched cards each of which includes the date, station identification number, and time. In addition to the clock synchronization error the printout includes the data, station ID numbers, time, corrected range predict (both range and time), and the measured time interval.

#### 4. Summary

On the basis of experimental evidence, there seems little doubt that the ranging time synchronization scheme is both practical and accurate. The data confirms an improvement in accuracy of approximately 1000 times over previous methods. Uncertainties of less than 10  $\mu\text{sec}$  appear to be easily obtainable, and the character of the data suggests that these may be reduced further to the 1- $\mu\text{sec}$  range. As station personnel become familiar with the procedure, the 1- $\mu\text{sec}$  accuracy should become a reality.

N67 15919

### L. Frequency Generation and Control: VCO Noise Measurement and Optimum Tracking Filters,

C. Cooper

#### 1. Introduction

This article describes a technique for measuring the phase noise spectral density function of a VCO and presents some experimental results obtained through the use of this technique. The accuracy obtained with these measurements seems acceptable. Using the measured spectral density function of the VCO noise, the optimum tracking filter is determined, using the method of R. C. Tausworthe in Ref. 20. Experimental results are then presented which confirm that the tracking filter so determined is actually the optimum.

## 2. Spectral Density Function Measurement

The basic equipment used in measuring the spectral density function of noise  $n$  is shown in Fig. 46. The output of our equipment is the time average of  $n_1^2$ ; and this is equal to the area under the curve of  $S_{nn}$ , the noise spectral density, versus  $f$  from  $-B_f$  to  $+B_f$ . By measuring the output of the equipment in Fig. 1 for low-pass filters with several different values of noise bandwidth  $B_f$ , the curve of  $S_{nn}$  versus  $f$  may be found.

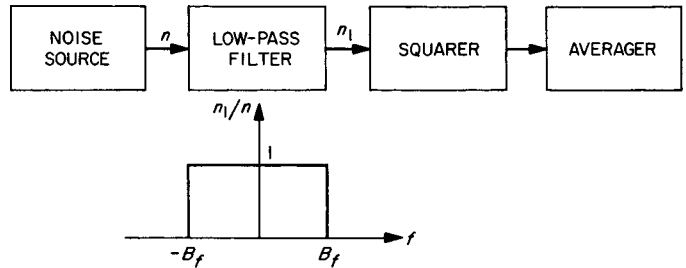


**Fig. 46. Equipment for measuring the spectral density function of a noise source**

## 3. VCO Phase Noise Spectral Density

Fig. 47 shows the linearized model of a phase-locked loop. The symbols appearing here are defined as

$\theta$  = input phase process

$\hat{\theta}$  = output phase process

$n$  = input noise process heterodyned to baseband

$n_v$  = VCO phase noise process, referred to the input of a unity gain VCO

$A$  = RMS input signal voltage

$K$  = open-loop gain

$F(s)$  = tracking filter transfer function

$L(s)$  = closed-loop transfer function

The effect of  $n$  and  $n_v$  upon  $\hat{\theta}$  may be expressed as

$$\hat{\theta}(t) = L(p) \frac{n(t)}{A} + \frac{1 - L(p)}{p} n_v(t) \quad (1)$$

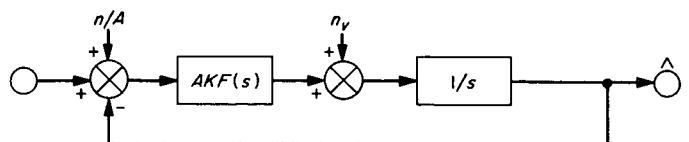


**Fig. 47. Linearized model of a phase-locked loop**

Let us now define  $n_o(t)$  as the VCO phase noise process referred to the VCO output. For frequencies above the loop bandwidth,  $n_o(t) \simeq n_v(t)/p$ . Setting the input signal  $\theta(t)$  equal to zero, the phase detector output  $\phi(t)$  is

$$\phi(t) = [1 - L(p)] \frac{n(t)}{A} - [1 - L(p)] n_o(t) \quad (2)$$

Let us now consider  $L(j\omega)$ , the Fourier Transform of  $L(p)$ . For frequencies well above the closed loop bandwidth,  $L(j\omega) \simeq 0$ , thereby causing  $\phi$  to be approximately

$$\phi(t) = \frac{n(t)}{A} - n_o(t) \quad (3)$$

Assuming that  $n(t)/A$  and  $n_v(t)$  are uncorrelated, the spectral density function of  $\phi$  is

$$S_{\phi\phi}(j\omega) = S_{\frac{n}{a}}(j\omega) + S_{n_o n_o}(j\omega) \quad (4)$$

We will assume that

$$S_{n_o} S_{n_o}(j\omega) \gg S_{\frac{n}{a}}(j\omega) \quad (5)$$

$$S_{\phi\phi}(j\omega) \simeq S_{n_o n_o}(j\omega)$$

We will later show some evidence which justifies this assumption for the particular experimental configuration upon which tests were made.

$S_{\phi\phi}(j\omega)$  can be measured by the technique discussed previously. Let us suppose that this has been done for frequencies above the loop bandwidth. Once an experi-

mental formula for  $S_{n_o n_o}(j\omega) \simeq S_{\phi\phi}(j\omega)$  has been found, we can deduce what  $S_{n_v n_v}(j\omega)$  should be. Set  $\theta$  and  $n/A$  equal to zero in Fig. 47 and observe that

$$n_o(t) = \frac{\frac{1}{p}}{1 + \frac{1}{p} AK F(p)} n_v(t) \quad (6)$$

Taking the Laplace Transform of the expression in the differential operator  $p$ ,

$$\frac{\frac{1}{s}}{1 + \frac{1}{s} AK F(s)} = \frac{1}{s + AK F(s)}$$

Examine the low-frequency asymptote of this transformed expression.

$$\lim_{s \rightarrow 0} \frac{1}{s + AK F(s)} = \frac{1}{AK}$$

The low-frequency limit holds for frequencies appreciably less than the closed loop bandwidth. Therefore  $n_o(t) = n_v(t)/AK$  for frequencies of the range in which VCO noise has its greatest effect upon the phase-locked loop's performance. The spectral densities are related as

$$S_{n_v n_v}(j\omega) = (AK)^2 S_{n_o n_o}(j\omega) \quad (7)$$

Usually, some of the effective gain  $AK$  appears as a phase detector constant and some as a VCO constant. In this case,  $AK$  in the above spectral density equation is replaced by the VCO gain.

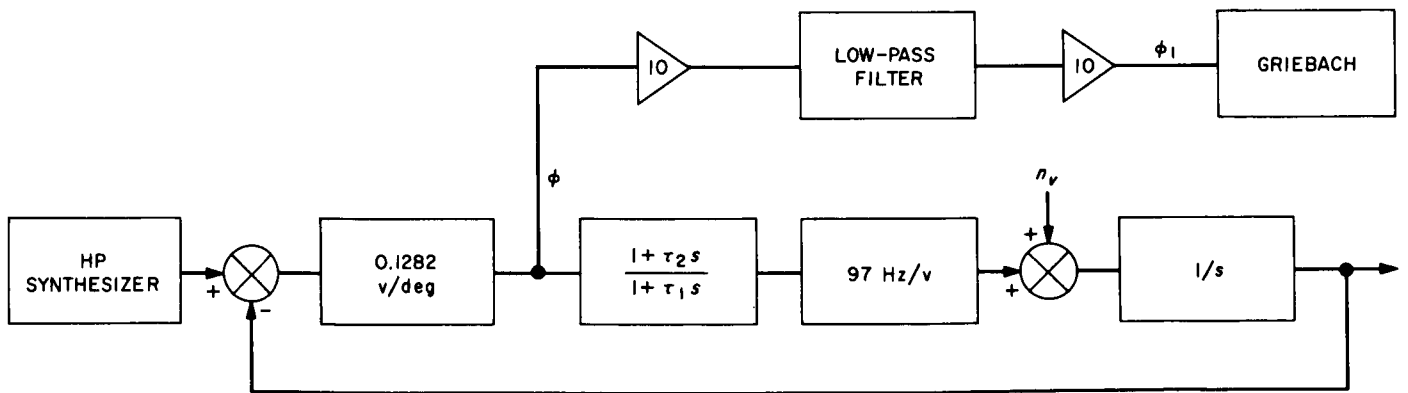


Fig. 48. Experimental apparatus for measuring the spectral density function of the VCO in the 35.2-MHz loop of the central frequency synthesizer

#### 4. Results

The equipment used in making the experimental measurements is shown in Fig. 48. The spectral density function of the phase detector output  $\phi(t)$  will now be measured. The Hewlett Packard (HP) frequency synthesizer supplies a pure tone to the phase-locked loop which is equal to the VCO center frequency. Two Fairchild AOO-6 low-noise amplifiers are used as shown to minimize loading on the outputs of the phase detector and the low pass filter. They also provide a combined gain of 100 in order to make the signal of interest more easily observable. The low-pass filter consists of a passive RC network. No use was made of sharp cutoff active filters, because they introduce an excessive amount of noise. The filtered noise is read on a Griebach voltmeter, a passive instrument which indicates the true RMS value from DC up to 100 kHz.

The Griebach possesses a damping time constant of several seconds, which is insufficient to average the very-low-frequency components present in the phase detector output. In order to obtain the average value of the square of the filtered noise, about 100 readings of the Griebach were taken at fixed time intervals. These readings were first squared and then averaged to obtain the mean square value of the filtered noise which appears on the left-hand side of Eq. (1). A computer program was written to perform this computation, and also to determine the standard deviation of the mean square value so obtained.

Fig. 49 shows some recordings of the phase detector output before and after filtering and squaring. The squared signal was obtained from a square law detector in the Griebach meter.

Table 13 shows two sets of data obtained in this manner. The second data set was obtained by bucking out the DC offset voltage before measuring with the Griebach and by taking a larger number of readings for each filter.

The data in this table was analyzed in the manner indicated by Eq. (1). The spectral density function should be of the form (Ref. 20)

$$S_{\phi\phi}(j2\pi f) = N_o + \frac{N_1}{|f|} \quad (8)$$

Table 13. Measurements of noise voltage

Measurement technique	Noise bandwidth of filter, $B_f$ , Hz	Mean of squares, volt <sup>2</sup>	Standard deviation of mean of squares, volt <sup>2</sup>
Normal data set	0.191	113.8991	3.4898
	1.844	116.5746	3.5718
	20.34	116.4412	4.9303
	209.31	115.2425	3.6107
Data using bucking voltage	0.407	1.6746	1.0058
	0.787	1.8763	.7996
	1.966	2.4063	1.1470
	19.46	2.5634	1.8008

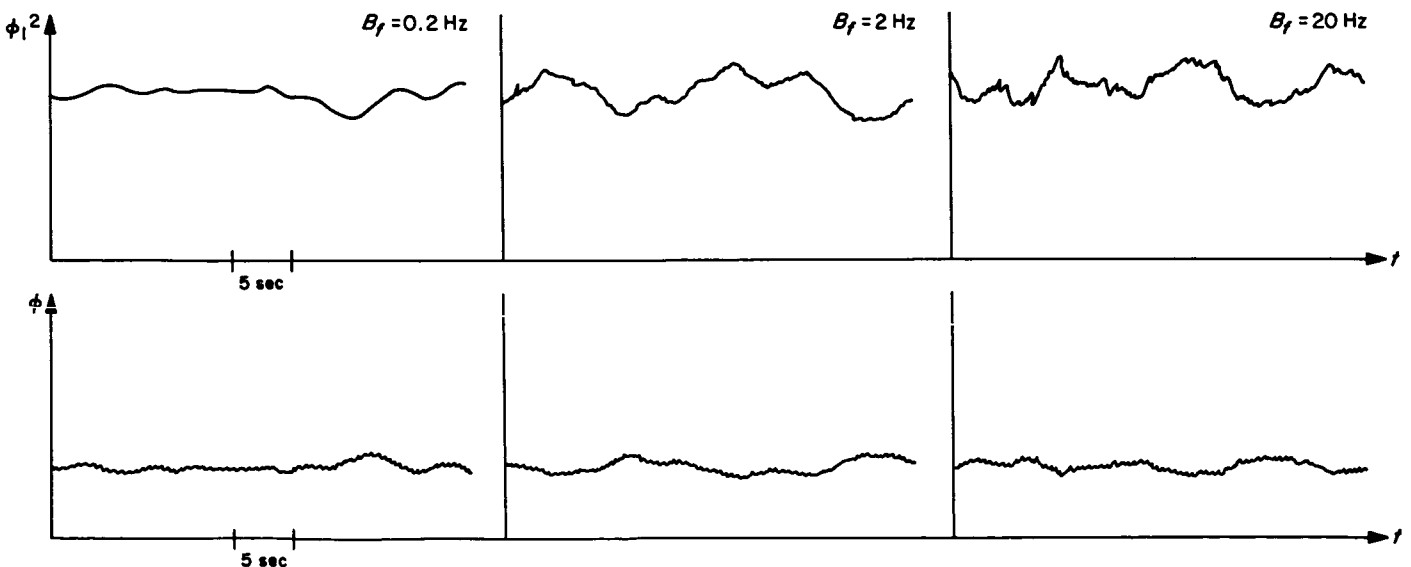


Fig. 49. Recordings of the phase detector output  $\phi$  and  $\phi^2$ , the filtered and squared phase detector output, for various low-pass filter noise bandwidths

Analysis of the above data indicates that no  $N_o$  term is present to within the accuracy limits of this experiment. Both sets of data obtained seem to indicate that  $S_{nn}(j2\pi f)$  may be somewhat more steeply sloped than  $1/f$ , perhaps more like  $1/f^2$ . This can be partially explained, however, by the fact that the rather low cutoff rate of the low-pass filters will accentuate the rate of decrease of a decreasing function when this measuring technique is used.

Table 14 shows the derivation of the best fit values of  $N_1$ . The average  $N_1$  for the first data set is

$$N_1 = 40.7 \times 10^{-6} \text{ v}^2$$

$$\sigma = 144.0 \times 10^{-6} \text{ v}^2$$

The average  $N_1$  for the second data set is

$$N_1 = 50.2 \times 10^{-6} \text{ v}^2$$

$$\sigma = 25.4 \times 10^{-6} \text{ v}^2$$

There is fairly good agreement between the average values of  $N_1$  for each set; but the variances show that the second set is much more reliable. If an appreciable  $N_o$  were present in  $S_{\phi\phi}(j2\pi f)$ ,  $N_1$  would increase with increasing  $B_F$ . Examination of Table 14 shows that this is definitely not the case. On the basis of this data, it is safe to say that

$$N_o < 5 \times 10^{-6} \text{ v}^2$$

The assumption made in Eq. (5) can now be verified. Starting with

$$S_{\phi\phi}(j2\pi f) = \frac{50.2 \times 10^{-6} \text{ v}^2}{|f|}$$

we find that

$$S_{n_o n_o}(j2\pi f) = \frac{30.5 \times 10^{-4} \text{ deg}^2}{|f|}$$

Integrating  $S_{n_o n_o}(j2\pi f)$  from 1 Hz to 100 Hz (and doubling to get the single-sided equivalent) gives  $0.028 \text{ deg}^2$ . W. F. Gillmore (Ref. 22) presents a phase noise spectral density curve for the HP frequency synthesizer against its driver. Integrating graphically from 1 Hz to 100 Hz gives  $0.003 \text{ deg}^2$ . Hence  $\frac{S_{n_n}(j2\pi f)}{a^2} \ll S_{n_o n_o}(j2\pi f)$  as assumed.

Finally, Eqs. (5) and (7) yield

$$S_{n_v n_v} = \frac{0.473(\text{Hz})^2}{|f|}$$

### 5. Verification of Optimum Filter Selection

Let the tracking filter transfer function be

$$F(s) = \frac{1 + \tau_2 s}{1 + \tau_1 s}$$

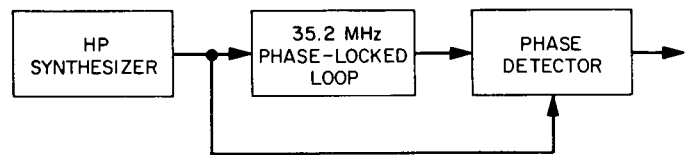


Fig. 50. Experimental apparatus for measuring phase noise variance

Table 14. Derivation of best fit values of  $N_1$

Measurement technique	$B_F$ , Hz	$\Delta \frac{\text{mean squares}}{2}$ , unscaled, volt <sup>2</sup>	$\Delta \frac{\text{mean squares}}{2}$ , scaled, volt <sup>2</sup>	$\ln \frac{BF_2}{B_F}$	$N_1$ , volt <sup>2</sup>
Normal data set	0.191	1.3377 -0.0667 -0.5993	$535.0 \times 10^{-6}$ $-26.6 \times 10^{-6}$ $-239.7 \times 10^{-6}$	2.266 2.400 2.331	$236.0 \times 10^{-6}$ $-11.0 \times 10^{-6}$ $-102.8 \times 10^{-6}$
	1.844				
	20.34				
Data using bucking voltage	209.31	1.009 0.2650 0.0785	$43.6 \times 10^{-6}$ $114.5 \times 10^{-6}$ $33.9 \times 10^{-6}$	0.657 1.648 2.291	$63.3 \times 10^{-6}$ $69.4 \times 10^{-6}$ $14.7 \times 10^{-6}$
	0.407				
	0.787				
	1.966				
	19.46				

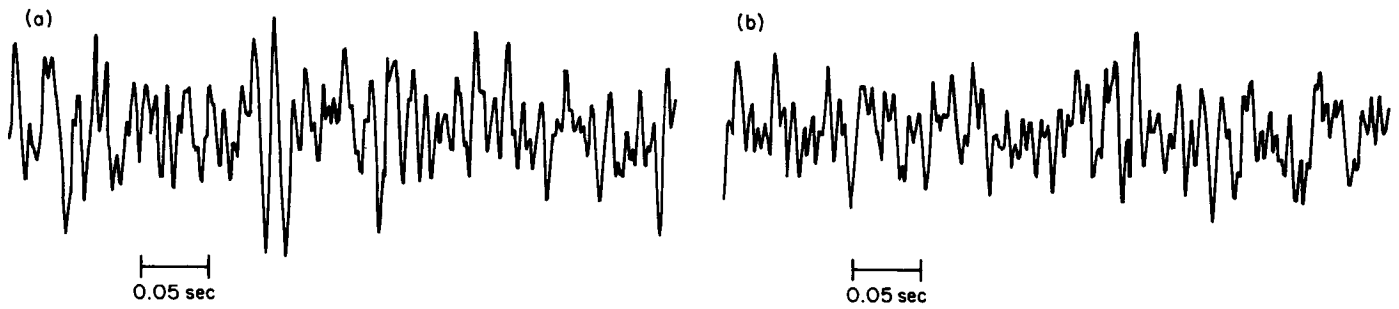


Fig. 51. Phase noise for (a) present tracking filter ( $r = 2, B_L = 0.5$  Hz), (b) optimum tracking filter ( $r = 7, B_L \cong 2$  Hz)

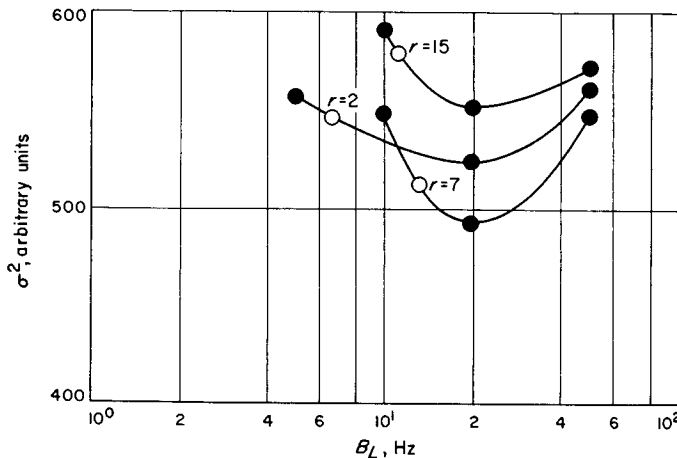


Fig. 52. Phase noise variance for tracking filters with various values of  $r$  and  $B_L$

The closed loop bandwidth  $B_L$  and a damping factor  $r$  can be defined as

$$B_L = \frac{r + 1}{4\tau_2} \quad r = \frac{AK\tau_2^2}{\tau_1}$$

Tausworthe has shown that in order to minimize that part of the output phase variance due to noise, the optimum value of  $r = 7$  and the optimum value of  $B_L$  is the solution of

$$B_L^2 - 0.143 \left( \frac{A^2 N_{ov}}{KT} \right) B_L - 0.774 \left( \frac{A^2 N_{1v}}{KT} \right) = 0 \quad (9)$$

where  $k$  is Boltzmann's constant. For the 35.2-Mc loop,  $A = 1.17$  v mean square and  $T = 290^\circ\text{K}$ , using the measured values  $N_{1v} = 0.473(\text{Hz})^2$  and  $N_{ov} = 0$  yields

$$B_L = 2.7 \text{ cps}$$

The equipment in Fig. 50 is used to verify that the optimum values of  $r$  and  $B_L$  are actually as predicted. The

phase detector output is recorded and  $6\sigma$  is taken to be that length which includes 99% of the peak to peak jitter. This method is used to find  $\sigma^2$  for a number of tracking filters with different values of  $r$  and  $B_L$ . Fig. 51 shows recordings made in this manner for both the optimum tracking filter and for the tracking filter presently in the loop. Fig. 52 shows  $\sigma^2$  for tracking filters with various values of  $r$  and  $B_L$ . A definite minimum of  $\sigma^2$  occurs at  $r = 7, B_L = 2$  Hz, which is close to the predicted optimum. The optimum filter yields approximately a 10%, or 1 db, improvement over the filter presently used in the loop, which has  $r = 2, B_L = 0.5$  Hz.

N67 15920

### M. Frequency Generation and Control: S- and X-Band Central Frequency Synthesizer, G. U. Barbani

#### 1. Introduction

The central frequency synthesizer (CFS) has been in operation at DSS 13 since May 3, 1966. In *SPS 37-40*, Vol. III, pp. 57-61 a description is given of the addition of a  $\times 4$  frequency multiplier (1- to 4-MHz) and a 4-MHz distribution amplifier. The CFS block diagram shown in Fig. 53 has been updated to include these modifications. A general report on CFS performance and the results of an investigation of the 35.075-MHz VCO static phase error are given in this report.

#### 2. Static Phase Error

The 35.075-MHz phase-lock loop experienced a static phase error  $> 0.5$  v for a period of about 4 wk. This error actuated the yellow (warning) condition lamp in the voltage vigilant system (VVS) which monitors all four phase-lock loops simultaneously (*SPS 37-39*, Vol. III, p. 66). Investigation of loop parameters such as phase detector drift, tracking filter components, in-lock detector, VCO frequency adjust and bias, etc., all proved

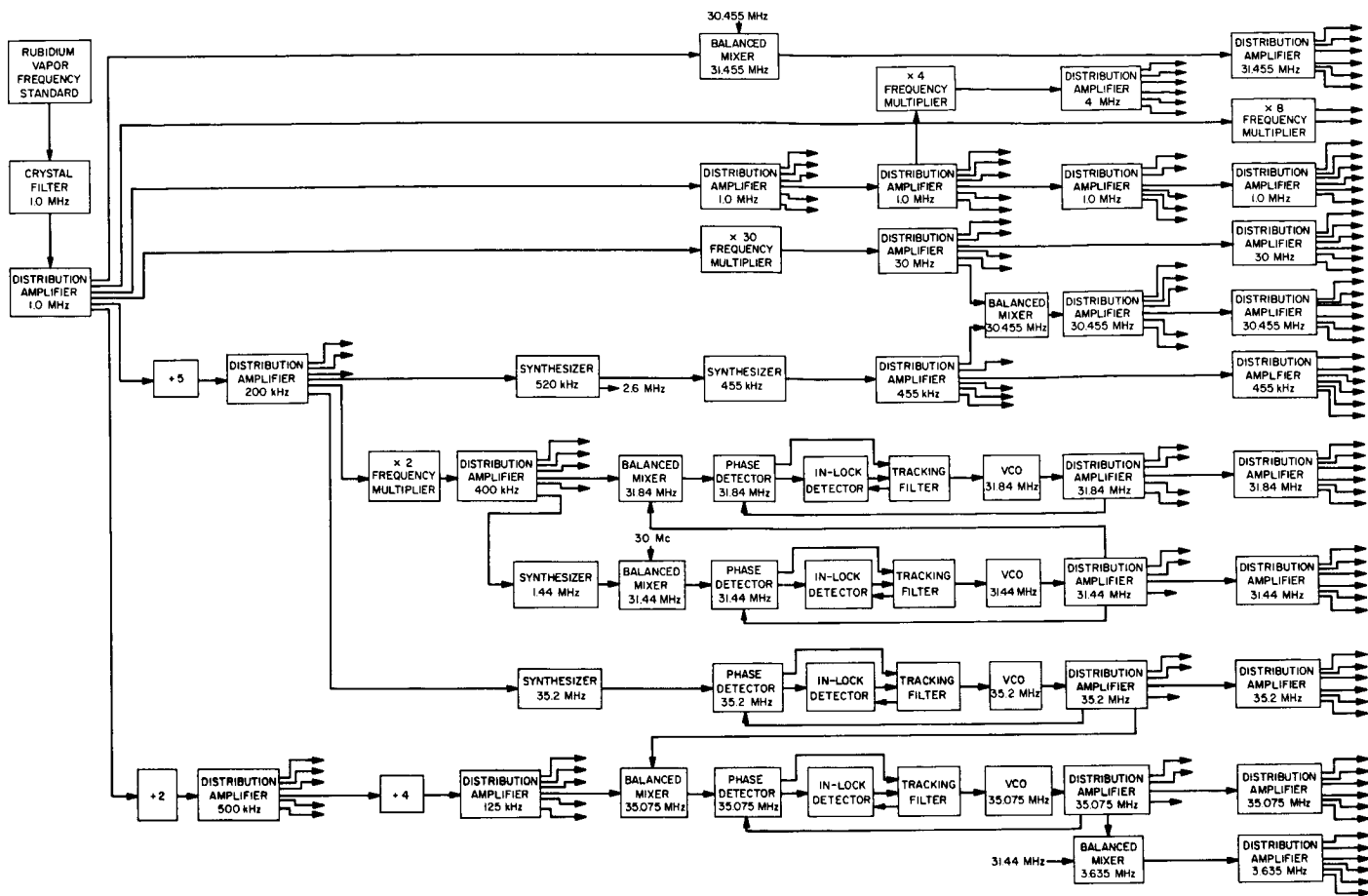


Fig. 53. Central frequency synthesizer Mod I block diagram

satisfactory. A reverse leakage current was discovered in the varicap circuit of the 35.075-MHz VCO which was causing the excessive static phase error. Replacement of the varicap with a new ultra-low leakage unit restored the circuit to correct operation. The circuit was monitored for the next 4 wk, and was found to be satisfactory (SPS 37-40, Vol. III, p. 61).

### 3. CFS Performance

The CFS has completed 9,423 continuous hours of operation as of October 2, 1966. During this quarter, monthly preventative maintenance schedules were performed and system data was taken. Of the systems monitored, the phase noise measurement and VCO frequency drift are the most important. Figs. 54 and 55 show the four VCO aging rates, or drift, at 30-day intervals, and they compare very well with the crystal manufacturer's tolerance for 90 days. It should be noted that all the RF components of the VCO within the +55°C oven are aging together and that the manufacturer's aging curve

is for the quartz crystal only. Fig. 54 shows both 31.44- and 31.84-MHz VCO aging rates to be within the manufacturer's stated limits, and Fig. 55 shows that the 35.075-MHz VCO has exceeded its limit during the July-August period. This relative increase could be due to the leakage current in the varicap circuit, as previously described.

Very good correlation is obtained between the aging rate and leakage current of the varicap, because the aging rate falls below the manufacturer's limits with the replacement of the faulty varicap. This data point is not shown on Fig. 55 because of the interruptions in oven stability and the replacement of the varicap in the 35.075-MHz VCO only. Although the 35.2-MHz VCO aging curve exceeded the early limits (faster aging rate), it has returned to specification during the 90-day period (Fig. 55).

The phase noise characteristics of all four phase-lock loops are shown in Figs. 56 and 57 which show the

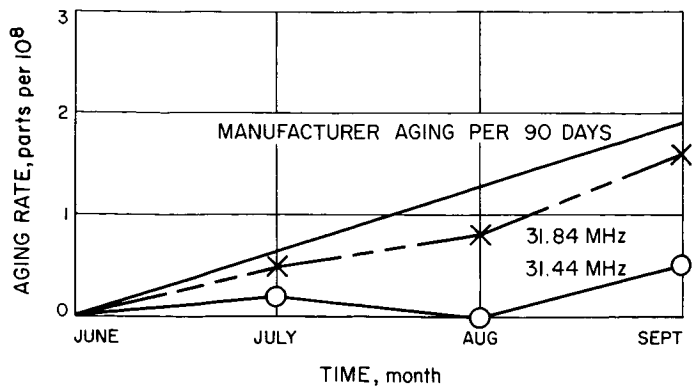


**Fig. 54. Frequency aging characteristics for 31.44- and 31.84-MHz VCO**

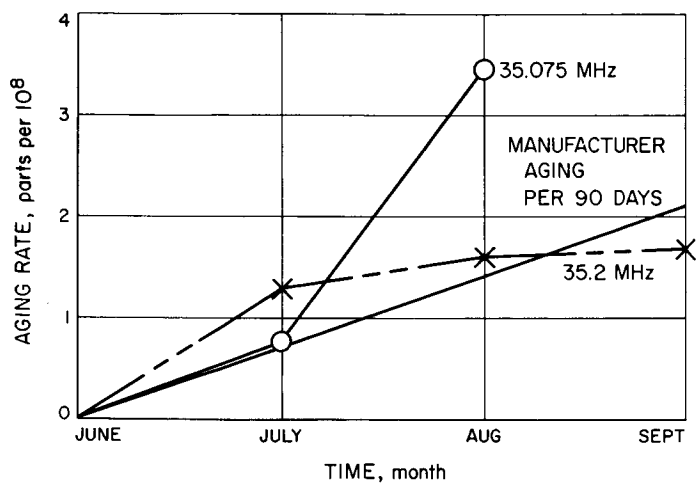


**Fig. 55. Frequency aging characteristics for 35.075- and 35.2-MHz VCO**

standard deviation  $\sigma$  for a three-month period. The variations in phase noise appear to be random, and two phase lock loops follow no particular trend. The 31.44-MHz phase-lock loop noise curve is not very meaningful, because the data point for the month of August was not available; however, a trend here may be possible (Fig. 56). The 31.84-MHz phase-lock loop seems also to be following the same trend, while the 35.075- and the 35.2-MHz phase-noise curves appear to be cyclical (Fig. 57). Observations during the next quarter should show any definite trends.

#### 4. Conclusions

Installation of the CFS along with its associated tests and measurements has been completed, and the system has been officially released for operational use. DSS 13 personnel have been schooled on operations, test procedures, and preventative maintenance. Three sets of

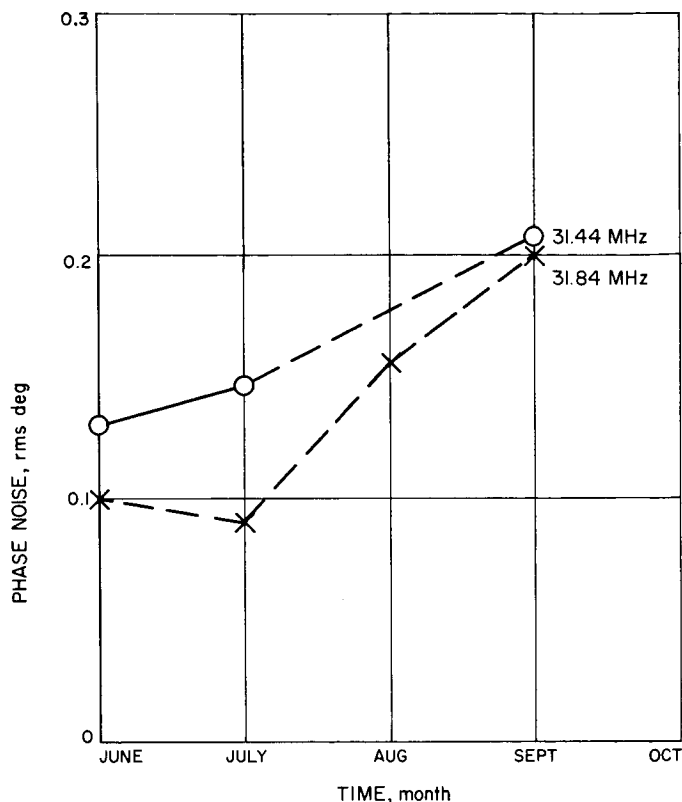


**Fig. 56. Phase noise characteristics of 31.44- and 31.84-MHz phase-lock loops**

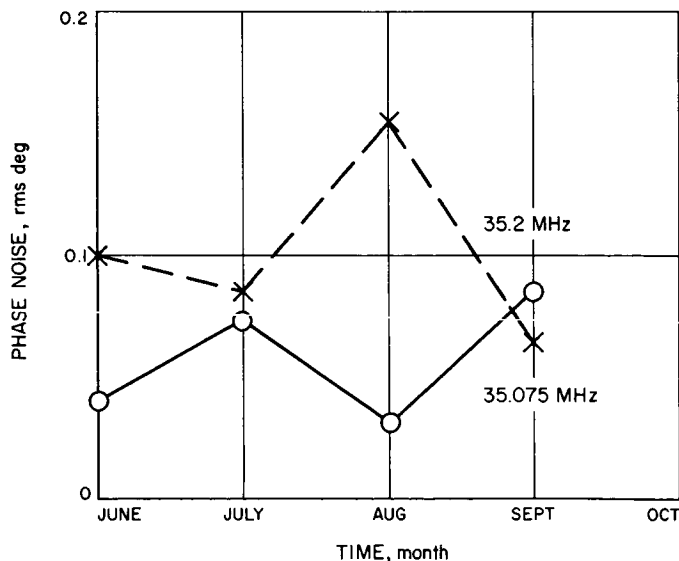


**Fig. 57. Phase noise characteristic of 35.075- and 35.2-MHz phase-lock loops**

complete documentation have been provided, and will be updated when necessary.

Further discussions will be limited to failure modes, modifications, and improvements.

## References

1. *Proc. IEEE*, Vol. 54, Feb 1966 (special issue on frequency stability).
2. Potter, P. D., "A New Horn Antenna with Suppressed Sidelobes and Equal Beamwidths," *Microwave Journal*, pp. 71-78, June 1963.
3. Potter, P. D., *A Simple Beamshaping Device for Cassegrainian Antennas*, Technical Report TR 32-214, Jet Propulsion Laboratory, Pasadena, January, 1962.
4. Ludwig, A. C., Editor, *Computer Programs for Antenna Feed System Design and Analysis*, Technical Report TR 32-979, Jet Propulsion Laboratory, Pasadena.
5. Ruze, J., "Antenna Tolerance Theory—A Review," *Proc. IEEE*, Vol. 54, No. 4, pp. 633-640, April 1966.
6. Potter, P. D., Merrick, W. D., and Ludwig, A. C., "Large Antenna Apertures and Arrays for Deep Space Communications," Technical Report TR 32-848, Jet Propulsion Laboratory, Pasadena, November 1965.
7. Ruze, J., *Physical Limitations on Antennas*, Technical Report TR 248, Research Laboratory of Electronics, Massachusetts Institute of Technology, Cambridge, ASTIA/AD 62351, October 1952.
8. Potter, P. D., *The Design of a Very High Power, Very Low Noise Cassegrain Feed System for a Planetary Radar*, Technical Report TR 32-653, Jet Propulsion Laboratory, Pasadena, August 1964.
9. Golomb, Solomon W., ed., *Digital Communications With Space Applications*, Prentice-Hall, Inc., Englewood Cliffs, New Jersey, 1964.
10. "Mark I Ranging Subsystem, Transmitter and Receiver Coders," SPS 37-21, Vol. III, Jet Propulsion Laboratory, Pasadena, California, May 31, 1963.
11. "Mark I Ranging Subsystem-Code Components Acquisition and Code Correlation," SPS 37-29, Vol. III, Jet Propulsion Laboratory, Pasadena, California, September 30, 1964, pp. 12-19.
12. DFN-1003-FNC-A Functional Specifications DSIF Tracking and Communications System, GSDS 1964 Model, Ranging Subsystem Mark I, Jet Propulsion Laboratory, Pasadena, California.
13. Hoel, P. G., *Introduction to Mathematical Statistics*, John Wiley and Sons, Inc., New York, N. Y., 1962, pp. 234-240.
14. *Tables of the Binomial Probability Distribution*, National Bureau of Standards Applied Mathematics Series, U. S. Government Printing Office, Washington, D. C., 1952.

## References (contd)

15. Tausworthe, R., *Theory and Practical Design of Phase-Locked Receivers, Vol. I*, Technical Report 32-819, Jet Propulsion Laboratory, Pasadena, California, February 1966.
16. Tausworthe, R. C., "Calculation of Range Clock Jitter," *SPS 37-40*, Vol. IV, pp. 219-225, Jet Propulsion Laboratory, Pasadena, California, August 31, 1966.
17. Martin, W. L., "Resolving the DSN Clock Synchronization Error," *SPS 37-39*, Vol. III, pp. 49-52, May 31, 1966.
18. McCoubrey, A. O., "A Survey of Atomic Frequency Standards," *Proceedings of IEEE*, Vol. 54, pp. 116-135, February 1966.
19. Wylie, C. R., *Advanced Engineering Mathematics*, Second Ed., McGraw Hill Book Co., New York, N. Y., 1960.
20. Tausworthe, R. C., "Minimizing VCO Noise Effects in Phase-Locked Loops," *SPS 37-33*, Vol. IV, pp. 287-289, May 1965.
21. Tausworthe, R. C., "Theory and Practical Design of Phase-Locked Receivers," Vol. I, Technical Report 32-819, Jet Propulsion Laboratory, Pasadena, California, February 15, 1966.
22. Gillmore, W. F., "Comparison Tests of Several Frequency Synthesizers," *SPS 37-40*, Vol. III, Jet Propulsion Laboratory, Pasadena, California, May 30, 1966.

## IV. Communications Engineering Development

### N67 15921

#### A. S-Band Receiver-Exciter Ranging Subsystem (RER), Blocks IIB and IIIC, H. Donnelly, C. E. Johns, R. W. Tappan, and M. R. Wick

##### 1. Introduction

The original S-band receiver-exciter (RE) subsystem was designated as GSDS 1964, or Block I, (Ref. 1 and 2) and was designed specifically for DSN requirements. The RE subsystem with the ranging (R) subsystem Mark I (Ref. 3) can precisely determine ranges up to 800,000 km when used in conjunction with an S-band "turnaround" transponder.

The use of this S-band RE subsystem for the MSFN necessitated the addition of some new designs as well as changes in the existing design. The RE subsystem containing these design changes has been designated Block II (Refs. 4 and 5).

Additional requirements for both the DSN and MSFN have necessitated further design improvements. These requirements are:

- (1) The capability of switching from one channel to another without the need to rephase and recalibrate the range receiver.
- (2) The capability of the receiver exciter ranging (RER) subsystem to support both DSN and MSFN tracking commitments.

The designs providing the capability of these requirements are designated the RER Blocks IIB and IIIC, respectively.

##### 2. Receiver-Exciter Ranging

The Block II RER subsystem uses a range code synchronizing signal (clock) that is derived from the exciter voltage-controlled oscillator (Fig. 1). This is mechanized by multiplying the VCO frequency by a factor of 5/221. The clock is also used as a reference signal for the ranging receiver and transfer loop.

Generating the range clock and reference signals in this manner makes it necessary to recalibrate the ranging receiver each time a large frequency change is made, such as switching between channels. This is because the delay in the ranging receiver varies as the clock frequency is changed. The primary contributor to this delay change is the predetection bandpass filter within the ranging receiver IF amplifier.

To eliminate the necessity for recalibration, the Block IIB design uses a fixed clock and reference frequency derived from the station standard. The design of the Block IIB ranging receiver and ranging subsystems is described in the following:

*a. Ranging receiver.* The fixed clock and reference frequency establishes a relatively constant delay in the rang-



ing receiver. Except for doppler offset, the detected ranging receiver clock frequency is constant, thereby minimizing the effect of the predetection filter. A fixed clock frequency of 496 kHz was selected to be compatible with most of the existing hardware. The clock signal is derived by multiplying a 1-MHz signal output from the tracking station standard by a factor of 496/1000.

The subassembly that performs the 5/221 multiplication in the Block II system to obtain the clock signal also generates two other coherent signals. These two signals drive a 57/221 frequency shifter subassembly to provide reference signals for the coherent translator and doppler extractor portions of the RF system. Since the 5/221 output is not required when the fixed clock frequency is used, a new design 57/221 frequency shifter was developed. This subassembly replaces both the Block II 5/221 and 57/221 frequency shifter subassemblies.

Fig. 1 is a block diagram showing both the present Block II ranging receiver together with the modifications which upgrade it to the Block IIB configuration.

A block diagram of the 496/1000 frequency shifter, which generates the fixed 496-kHz clock signal, is shown in Fig. 2. A 1-MHz signal from the station standard is used as the input to the shifter. At the output of the 1-MHz amplifier the signal is divided into two paths. One path connects the 1-MHz amplified signal to one input of a balanced mixer. The second path is used to synchronize an oscillator whose output is tuned to 200

kHz. Two similar divide-by-five stages follow, generating an 8-kHz signal which is applied to the second input of the balanced mixer. The 992-kHz difference frequency at the mixer output is selected by a crystal bandpass filter. After two successive stages of amplification, the 992-kHz signal is used to synchronize a divide-by-two oscillator circuit generating the desired 496 kHz signal.

The new design 57/221 subassembly utilizes a new technique for obtaining frequency division from a locked oscillator and is described in detail elsewhere in this volume.

The 496-kHz fixed clock frequency is used in both the DSN and MSFN Block IIB design. To obtain a completely common system, which is the purpose of the Block IIC design, the three Block II DSN loop noise bandwidths are being used for both the Block IIB DSN and MSFN receivers. This eliminates the need for including both the three DSN and three MSFN bandwidths and the capability of selecting either set of three. The DSN noise bandwidths (0.8, 4, 12 Hz) are adequate to meet the requirements of both the DSN and MSFN.

*b. Ranging subsystem, Mark I.* The fixed ranging clock frequency of the Block IIB receiver-exciter causes a non-integer ratio to exist between the clock and RF doppler frequency. The doppler counting logic of the Mark I must be changed to allow the RF doppler to be tallied correctly.

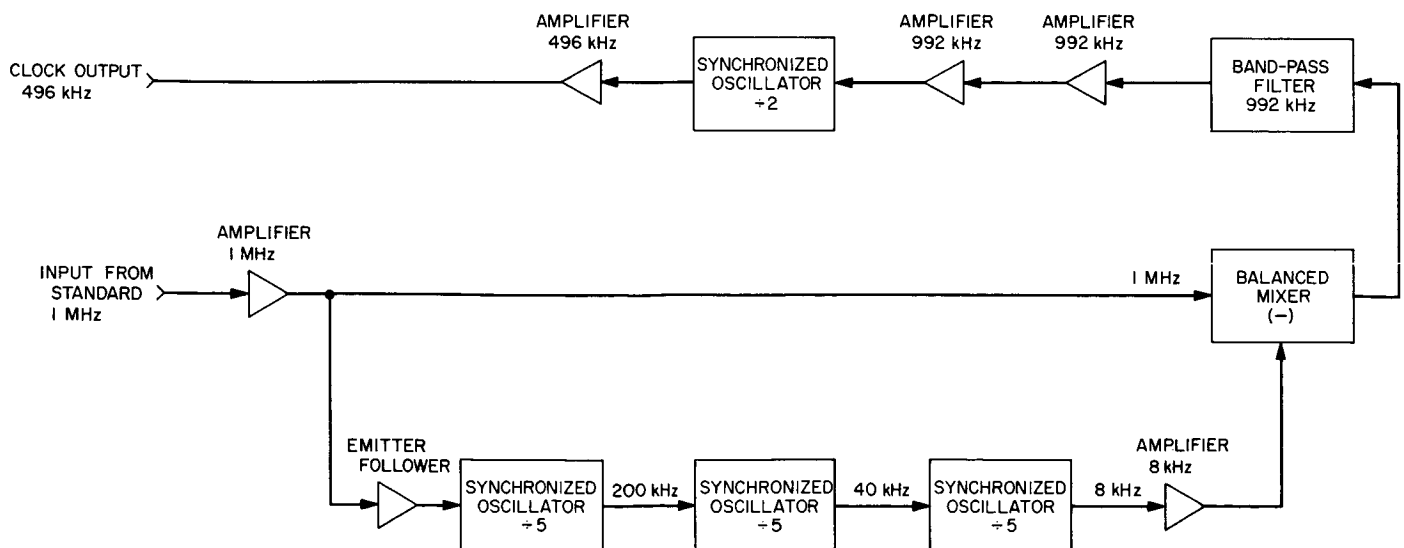


Fig. 2. 496/1000 Frequency shifter, block diagram

Fig. 3 illustrates the method of doppler counting used in the current ranging configuration. Both the clock and RF doppler signals pass through an input buffer to the range tally. The doppler selector routes the clock doppler to the range tally during code acquisition, and RF doppler to the range tally during the tracking portion of the ranging operation. The clock and RF doppler counts are related to each other by a fixed ratio. 72 RF doppler counts = 72 range units (RU) = 1 clock doppler count. The length of the range unit in light-time units is dependent upon the ranging clock frequency, which, in turn, is derived from the transmitter frequency  $F_t$ , and is

$$1 \text{ RU} = \frac{1}{2 \times 288 \left( \frac{5}{221} \times \frac{f_t}{96} \right)} \text{ light seconds, one-way range.}$$

In the Block IIB configuration, the ranging clock frequency is fixed at 496 kHz. The range unit is, therefore, a constant length, and is:

$$1 \text{ RU} = \frac{1}{2 \times 288 \times 496 \text{ kHz}} = 3.5002 \text{ light nsec, one-way range or approximately } 1.049 \text{ m}$$

Fig. 4 illustrates the manner in which the clock and RF doppler are counted in the Block IIB configuration. The range tally retains the Chinese Number and clock doppler tallying functions. The RF doppler tallying is done by a new subassembly called the RF doppler counter. This subassembly contains the RF doppler input buffer, doppler counter, and range number adder.

The range tally stores the portion of the total range that resulted from code shifting and clock doppler counting, and the RF doppler counter stores the range change that occurred since the last clock doppler count. The RF doppler counter counts the number of range units of RF doppler between clock doppler counts (Fig. 5). When the range to the spacecraft is increasing, a clock doppler count causes 72 RU to be added to the range tally, and the RF doppler counter to be reset to zero. RF doppler counts then accumulate in the RF doppler counter until the next clock doppler count resets it to zero. If the range to the spacecraft is decreasing, a clock doppler count causes 72 RU to be subtracted from the range tally, and the RF doppler counter to be set to 72. The range number adder sums the outputs of the range tally and the RF doppler counter to provide an output that is the total range.

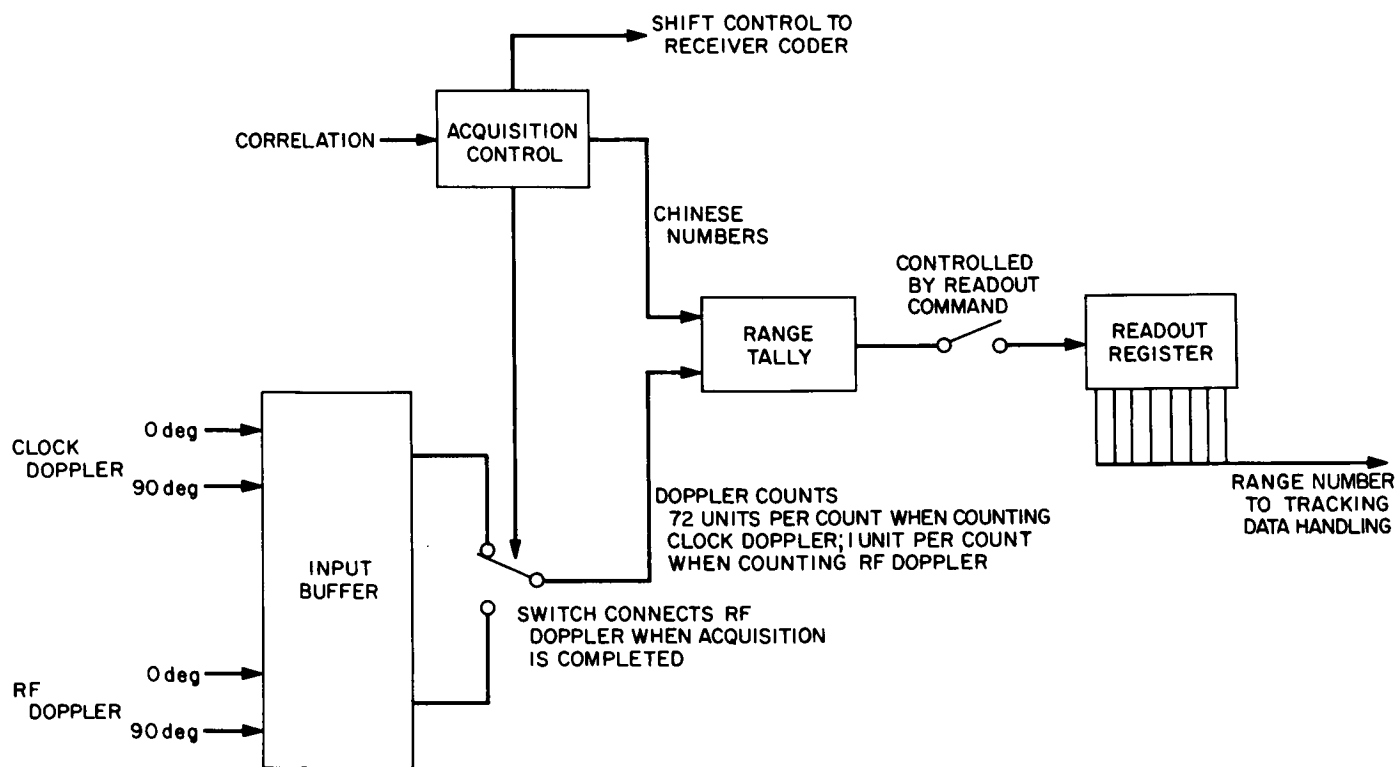


Fig. 3. Ranging subsystem Mark I doppler tally, Block II, configuration

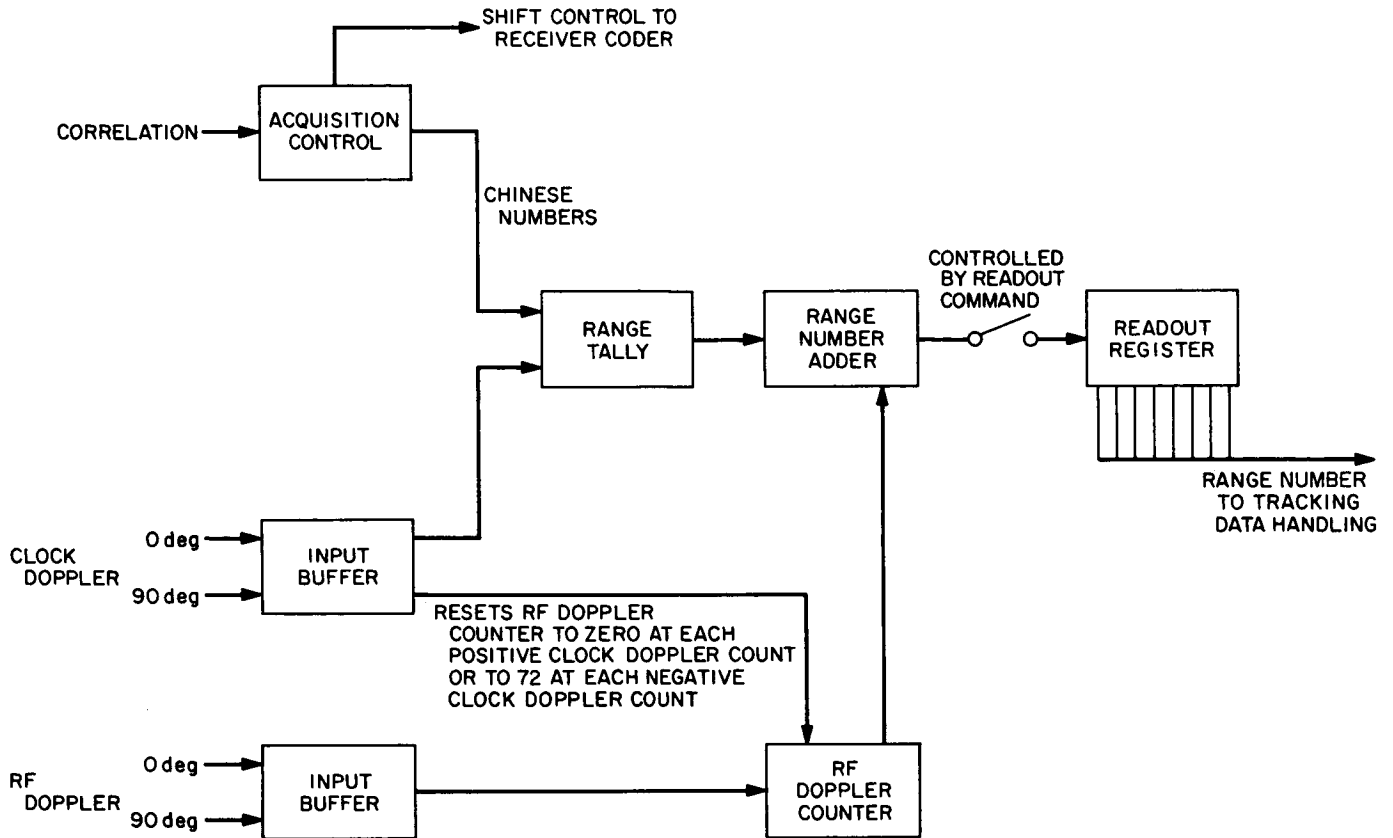


Fig. 4. Ranging subsystem Mark I Mod IIB doppler tally, Block IIB, configuration

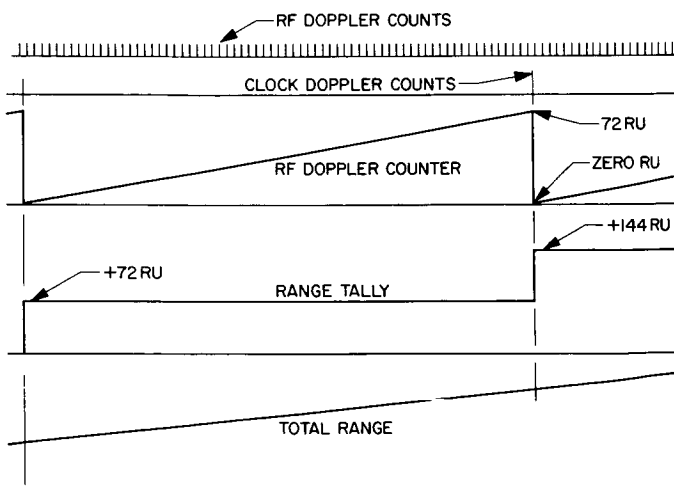


Fig. 5. Timing diagram

A small range error may exist in the Block IIB ranging configuration. The ratio of the ranging clock frequency to the S-band transmitter frequency is not constant; therefore, one clock doppler count is not always equal to

exactly 72 RF doppler counts. Since this error is not cumulative, it will always be less than 0.5 RU. Techniques for removing this error are known and may be used if the error is considered significant.

### 3. Receiver-Exciter, Block IIIC

The purpose of the Block IIIC design is to fulfill requirement 2, the capability of tracking both DSN and MSFN space probes. The existing Block II design does not provide this capability in the following areas:

- (1) Exciter tuning range
- (2) Receiver tuning range
- (3) Reference receiver predetection and loop noise bandwidths
- (4) Receiver AGC loop noise bandwidth
- (5) Range receiver predetection and loop noise bandwidths

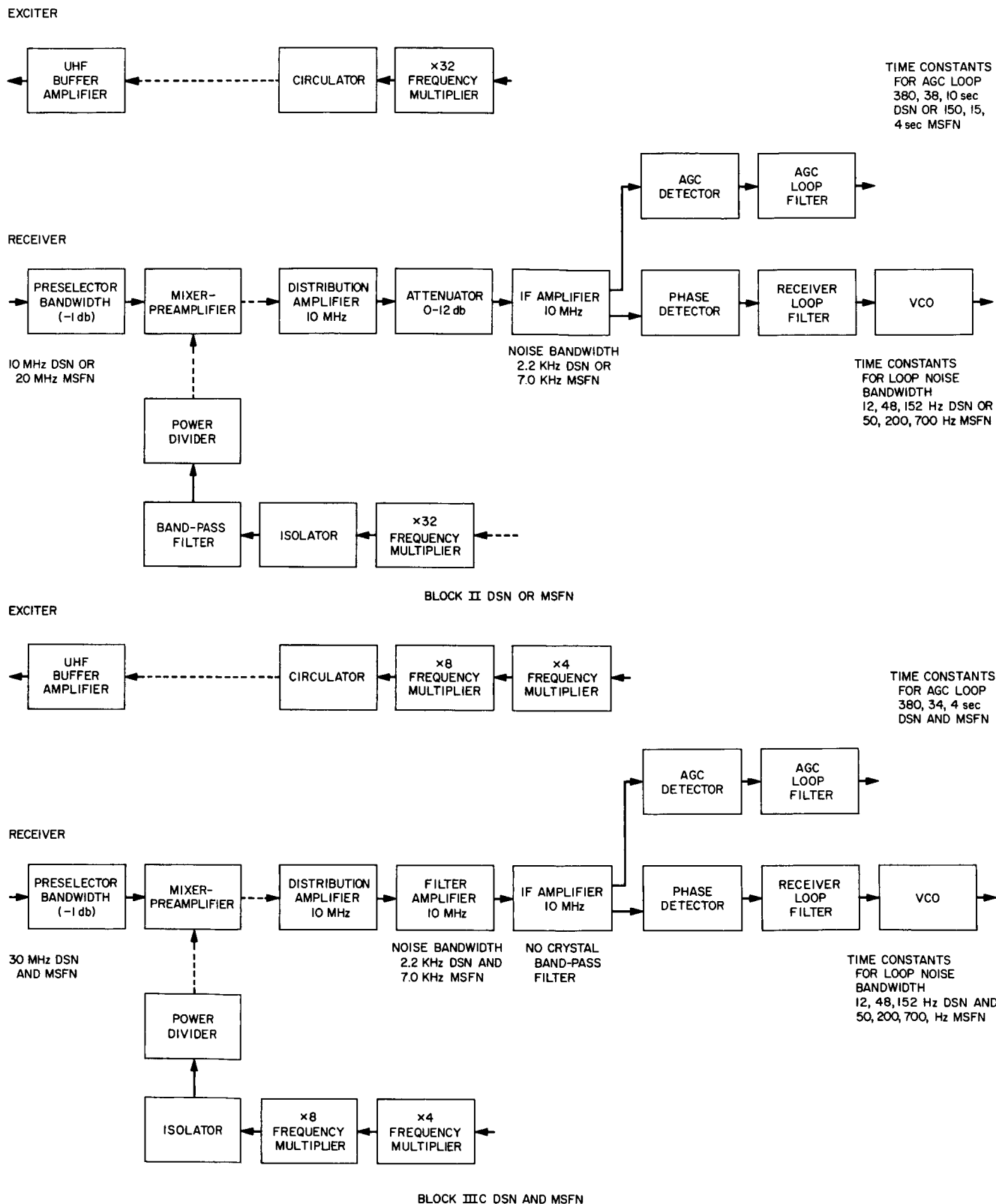


Fig. 6. Block II and III C block diagram

Following is a more detailed discussion of these areas.

*a. Exciter tuning range.* The existing  $\times 32$  frequency multiplier and UHF buffer amplifier of Block II are capable of delivering the required drive level to the power amplifier over either the DSN or MSFN 10-MHz bands but not over the combined 20-MHz band. In Block IIIC (Fig. 6) the  $\times 32$  frequency multiplier is replaced with a design that has adequate bandwidth to cover both the DSN and MSFN bands. This is accomplished in two subassemblies, a  $\times 4$  and a  $\times 8$  frequency multiplier. The  $+27.5$  dbm minimum output level of the Block IIIC multiplier chain provides adequate drive to obtain the 20-MHz bandwidth from the existing Block II UHF buffer amplifier.

The  $\times 4$  frequency multiplier subassembly consists of two cascaded low-level balanced diode doublers separated by an isolation amplifier and followed by four stages of amplification. A coaxial commercial bandpass filter is installed between the first two of the four cascaded amplifiers to provide rejection of harmonics of the input frequency other than the  $\times 4$ .

The  $\times 8$  frequency multiplier uses some of the latest techniques in step recovery diode frequency multiplication, and is discussed in detail in Ref. 6.

*b. Receiver tuning range.* The problem of adequate tuning range in the receiver local oscillator for both DSN and MSFN combined bands has been resolved in Block IIIC by replacing the local oscillator multiplier chain with the same design used in the exciter. The use of a second coaxial filter in the  $\times 4$  multiplier subassembly at the output of the final power amplifier provides the additional attenuation of sidebands that is required. With this design it is no longer necessary to provide a filter at the S-band output of the local oscillator multiplier.

Adequate tuning range at the receiver input is obtained by replacing the existing preselector with one that covers the combined DSN and MSFN bands.

*c. Reference receiver predetection and loop noise bandwidths.* The Block IIIC design contains the predetection and loop noise bandwidths of both the DSN and MSFN Block II subsystems. Selection is made independently for each receiver with the switches on the acquisition control panel (Ref. 7).

To provide both DSN and MSFN predetection filter bandwidths, a new 10-MHz filter amplifier subassembly

has been added to the subsystem ahead of the 10-MHz IF amplifier. This unit is mounted in the location now occupied by the 0-12 db attenuator subassembly (gain adjustment at 10 MHz now being provided only in the angle channel receivers). Since both the DSN and MSFN predetection crystal filters are located in the 10-MHz filter amplifier subassembly, the crystal filter in the Block II 10-MHz IF amplifier has been removed.

The receiver loop filter module contains the time constants for both the three DSN and the three MSFN loop noise bandwidths.

*d. Receiver AGC loop noise bandwidth.* Three loop time constants (380, 34, 4 sec) which adequately cover the DSN and MSFN requirements have been selected. These bandwidths are common to both systems, and no selection is required.

*e. Range receiver predetection and loop noise bandwidths.* As in the AGC loop, a design common to the DSN and MSFN has been selected for the ranging receiver (see Block IIB design).

#### 4. Conclusion

Blocks IIB and IIIC provide a system with both the DSN and MSFN parameters and the capability to select these parameters by switch control. The parameter differences have now been reduced to the reference receiver predetection and loop noise bandwidths. However, the exciter and receiver voltage-controlled oscillator subassemblies still contain only four selectable channels. Two sets of VCO subassemblies are provided in Block IIIC, one for the four MSFN channels and one for four DSN channels. Switching from an MSFN channel to a DSN channel or vice versa requires that the VCO subassemblies installed in the subsystem be replaced with the second set. Present plans are to upgrade all DSN and MSFN RER subsystems to Blocks II, IIB and IIIC.

N67 15922

#### B. 57/221 Frequency Shifter—Block IIB, C. E. Johns

##### 1. Introduction

A frequency shifter for the Block IIB receiver-exciter has been developed to derive reference signals coherently related to the exciter VCO frequency by a factor of 57/221. These reference signals are required for the doppler extractor and the coherent translator.

The block diagram of the 57/221 frequency shifter subassembly is shown in Fig. 7. The input signal from

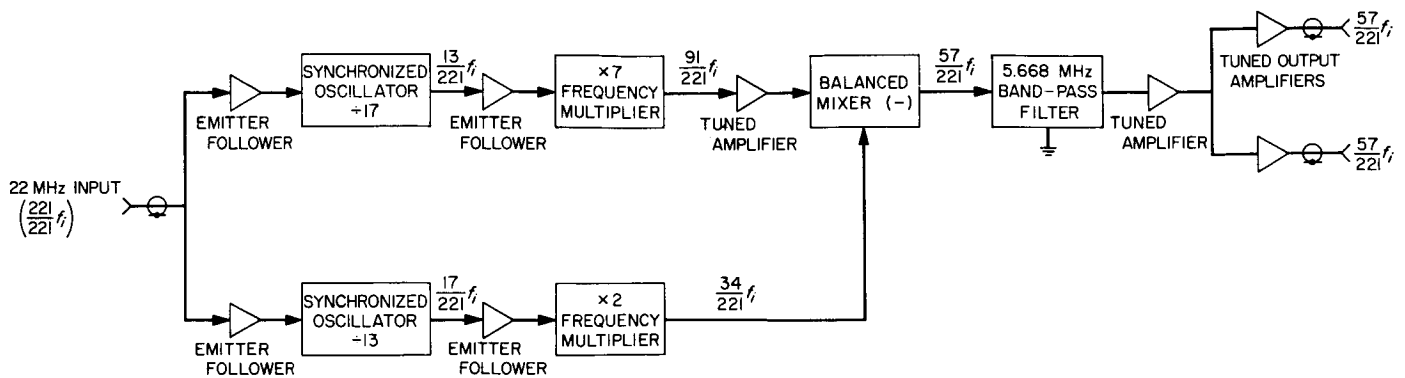


Fig. 7. 57/221 Frequency shifter block diagram

the exciter VCO is branched into two paths. One signal path is used to synchronize a transistor oscillator circuit whose output is tuned to  $\frac{1}{221}$ th of the input frequency  $f_i$ . The output frequency of this synchronous oscillator, which is  $\frac{17}{221}$  of the input frequency, is doubled in a transistor stage and coupled to one input of a balanced mixer. The second signal path is used for synchronizing a similar oscillator whose output is tuned to  $\frac{1}{221}$ th of the input frequency. This signal,  $\frac{13}{221}$  of the input frequency, is multiplied by seven in a transistor stage and applied to the second input of the balanced mixer through an isolation amplifier. The difference frequency at the mixer output,  $\frac{57}{221}$  times the input frequency to the subassembly, is selected by the crystal bandpass filter. Amplifier stages provide two isolated outputs.

Emitter followers precede the oscillators to prevent signal cross-coupling between their inputs and to reduce the amount of feedback to the input terminal. The output of each oscillator is impedance-matched to its respective multiplier by means of another emitter follower.

## 2. Synchronized Avalanche Oscillator

Basic to the operation of the frequency shifter is the type of synchronized oscillators used to perform the division processes. Although schematically the oscillators appear to be similar to the conventional type, their operation is entirely different.

In the conventional type the natural frequency (tuned circuit resonant frequency) is the desired frequency. It is difficult to force the circuit to oscillate at frequencies higher or lower than its natural frequency by an external signal and, therefore, it can be synchronized only over a narrow frequency range. During the development of the 57/221 frequency shifter, it was found that this type of oscillator would not perform the high division ratios

over the required frequency range. Another characteristic of the conventional locked oscillator is its relatively large amount of phase instability. Since the natural frequency of the oscillator is the desired frequency, synchronization is maintained by supporting this natural oscillation with the incoming signal. This does not occur at precisely the same phase in each cycle, and phase instability occurs. In addition, oscillator drift with temperature change causes loss of synchronization unless compensation is added.

To meet the requirements of the Block IIB 57/221 frequency shifter design, it was necessary to investigate other means of synchronizing an oscillator circuit. The use of avalanche breakdown as a method of synchronizing was explored. A schematic of a divider circuit using this technique is shown in Fig. 8. The resonant circuit is formed by L2 and the series combination of C2 and C3. Regeneration is accomplished by the connection of the emitter to the junction of C2 and C3.

Fig. 9 is a composite oscilloscope photograph showing operational events in their correct phase and voltage

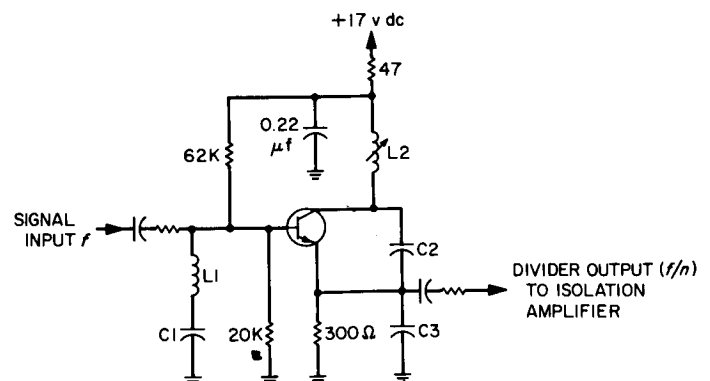


Fig. 8. Synchronized avalanche oscillator schematic

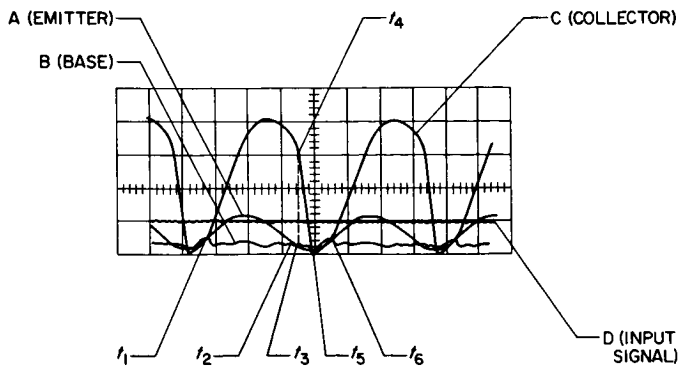


Fig. 9. Synchronized avalanche oscillator waveforms

relationships. Between  $t_1$  and  $t_2$  the emitter voltage (trace A) is positive with respect to the base voltage (trace B), therefore the transistor is not conducting. During this time the collector voltage (trace C) is increasing positively at a sinusoidal rate. At  $t_3$  the base-emitter bias voltage crosses over and starts forward biasing of the transistor. At  $t_4$  the bias becomes sufficiently large to cause the collector current to be driven into an avalanche mode of operation. The type of transistor used was selected for this characteristic. Between  $t_4$  and  $t_5$  the collector-to-emitter voltage rapidly decreases to zero and all the available supply voltage appears across the collector load. Between  $t_5$  and  $t_6$  no collector current flows as the collector-to-emitter voltage is zero. At  $t_6$  the collector voltage again starts increasing sinusoidally, and the next cycle begins.

When an input signal, which is some multiple of the oscillator frequency, is applied to the base of the oscillator, synchronization takes place. This occurs because one cycle of the input frequency ( $t_4$  on Fig. 9) adds to the base to emitter bias and forces the transistor into the avalanche mode. Capacitor C1 reduces the amount of ripple on the base, which is caused by the large collector variations. This permits the input frequency to be more effective in triggering the collector current. Inductor L1 prevents the input signal from being shorted to ground through capacitor C1. Its value is selected to give a high impedance at the input frequency and a relatively low one at the oscillator frequency.

Collector current flows only between the period of  $t_4$  and  $t_5$  which represent approximately 10% of one cycle. During the remaining 90% no current flows, therefore the transistor is acting only as a regenerative switch. The transistor is prevented from jumping into a destructive breakdown mode by limiting the maximum collector current flow with an emitter resistor. During the avalanche

conditions the collector-to-emitter voltage rapidly decreases to zero, simultaneously reducing the current. Measurements indicate a peak-to-peak current over a one-cycle period of approximately 6.8 ma.

### 3. Lock Range

The avalanche-type locked oscillator depends on the breakdown point as well as its tuned circuit to establish the output frequency, making it more easily controlled by an external signal. The waveforms of a divide-by-five locked oscillator are shown in Fig. 10 in more detail to demonstrate this. A divide-by-five circuit was arbitrarily selected to give a clear presentation of the base waveform (trace 2). The collector waveform is trace 1, while the large sine wave shown in dotted lines (trace 3) is the frequency of the collector tuned circuit. At point A on the base waveform, the collector current is triggered into the avalanche mode and causes the output frequency to be shown in trace a. If the input frequency is decreased, then the collector avalanches at point B (on the base waveform) and the output frequency is decreased (as shown on trace b of the collector waveform). Conversely, if the input frequency is increased (point C on the base waveform) the output frequency is increased (trace c on the collector waveform).

Control of the output frequency is relatively independent of the collector tuned circuit. Consequently, it is not necessary to pull the natural oscillator frequency when changing the frequency of the input synchronizing signal. The avalanche oscillator, therefore, inherently has a much larger lock range than the conventional type. Measurements of two divide-by-five circuits (28.35 to 5.67 MHz), one of each type, show the lock range for the avalanche oscillator to be more than four times that of the conventional oscillator. The conventional type was optimized for lock range prior to performing the measurements.

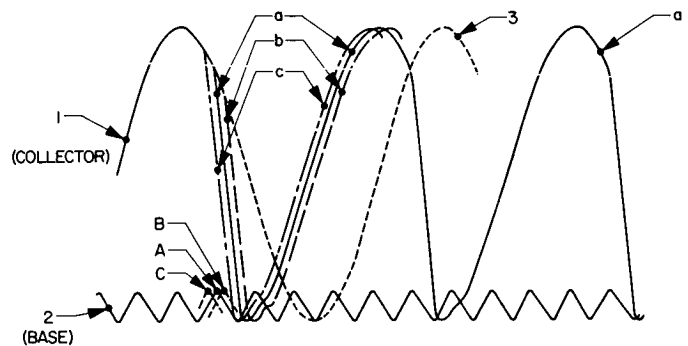


Fig. 10. Typical divide-by-five circuit waveforms

#### 4. Phase Instability

Controlling the synchronism of the oscillator by avalanche breakdown rather than supporting the natural frequency of the oscillator gives a more positive lock. This has been demonstrated in phase instability measurements made on both types. To accomplish this, two identical avalanche divide-by-five circuits (28.35 to 5.67 MHz) were compared, using a 5.67-MHz phase detector. The two divide-by-five circuits were driven by the same signal generator to eliminate the instability of the source. Then an avalanche and a conventional divider were compared in the same manner. The measurements indicated that the phase instability contributed by the conventional locked oscillator divider circuit is approximately four times as great as the avalanche type. The contribution of the avalanche oscillator in the second measurement is negligible so that this measurement represents approximately the instability of the conventional locked oscillator.

#### 5. Conclusion

Because of the method of synchronization, the avalanche oscillator has demonstrated several advantages

over the conventional locked oscillator. The advantages are that it:

- (1) maintains synchronism over a greater frequency range,
- (2) has less inherent phase instability, and
- (3) is less sensitive to temperature changes.

Typical characteristics of the 57/221 frequency shifter subassembly using the synchronized avalanche oscillator design are:

Input frequency: 21.9792 MHz

Output frequency: 5.6688 MHz

Bandwidth (controlled by crystal filter):  $\pm 33$  kHz  
(-1 db)

Lock range:  $> \pm 2\%$

Phase instability: approximately 0.01 deg rms

### References

1. "GSDS 1964 S-Band RF System," *SPS 37-28*, Vol. III, pp. 30-39, Jet Propulsion Laboratory, Pasadena, California, July 31, 1964.
2. "DSN 1964 S-Band Receiver-Exciter System," *SPS 37-32*, Vol. III, pp. 10-19, Jet Propulsion Laboratory, Pasadena, California, March 31, 1965.
3. "Mark I Ranging Subsystem," *SPS 37-20*, Vol. III, pp. 12-15, March 31, 1963; *SPS 37-21*, Vol. III, pp. 16-18, May 31, 1963; *SPS 37-22*, Vol. III, pp. 5, 6, July 31, 1963; *SPS 37-23*, Vol. III, pp. 11-14, September 30, 1963; *SPS 37-24*, Vol. III, pp. 9-11, November 30, 1963; *SPS 37-27*, Vol. III, pp. 22-25, Jet Propulsion Laboratory, Pasadena, California, May 31, 1964.
4. "Manned Space Flight Network S-Band Receiver-Exciter," *SPS 37-33*, Vol. III, pp. 39-43, and 50-54, Jet Propulsion Laboratory, Pasadena, California, May 31, 1965.
5. "S-Band Receiver-Exciter System," *SPS 37-35*, Vol. III, pp. 45-47, Jet Propulsion Laboratory, Pasadena, California, September 30, 1965.
6. "Step Recovery Diode Multiplier," *SPS 37-41*, Vol. III, pp. 99-100, Jet Propulsion Laboratory, Pasadena, California, September 30, 1966.
7. "Equipment for RF Carrier Acquisition Using the MSFN S-Band Receiver-Exciter," *SPS 37-40*, Vol. III, pp. 69-75, Jet Propulsion Laboratory, Pasadena, California, July 31, 1966.

## V. Deep Space Station Engineering and Operations

**N67 15923**

### A. Flight Project Support, J. Orbison

#### 1. Surveyor II Mission

The *Surveyor II* spacecraft was launched from Cape Kennedy, Florida, on September 20, 1966. On the same day, the Pioneer DSS, with the Echo DSS as a transmitter backup, tracked the first pass. The midcourse maneuver commands were transmitted from the Pioneer DSS early in the pass.

Following the second pass acquisition of the *Surveyor II* spacecraft on September 22 by the Pioneer DSS, unsuccessful attempts were made to stop the vehicle's tumbling, and less than 24 hr before the scheduled landing of the spacecraft, the mission was terminated.

#### 2. Lunar Orbiter I Mission

Tracking of the *Lunar Orbiter I* was performed daily by the Echo DSS until pass 36, on September 16, 1966. During pass 34, on September 14, the Goldstone calibration leader in the spacecraft camera equipment was read out in a final video sequence for a TV system degradation determination.

Following pass 36, tracking of the *Lunar Orbiter I* has been on an extended mission, as-scheduled basis. Rang-

ing and time correlation experiments using the Mark I ranging subsystem and the *Lunar Orbiter* ranging transponder have been performed between the Echo DSS and the Robledo DSS, and the Echo DSS and the Tidbinbilla DSS. Two Stanford lunar mapping experiments using the *Lunar Orbiter I* spacecraft were performed during passes 56 and 62.

#### 3. Pioneer Missions

*a. Pioneer VI mission.* Currently in the tenth month of its mission, the *Pioneer VI* spacecraft is being tracked by the Mars DSS 210-ft antenna on a scheduled basis. The Echo DSS provides telemetry and command processing via microwave to the Mars DSS. Routine data are being returned from the spacecraft, and the vehicle provides an accurate source for antenna and system testing in progress at the Mars DSS.

*b. Pioneer VII mission.* Because of the Echo DSS commitment to *Lunar Orbiter I*, the *Pioneer VII* spacecraft was tracked by the Pioneer DSS from the launching date, August 17, 1966, until pass 22, September 7, 1966. Telemetry and command processing from the Pioneer ground operations equipment (GOE) and the telemetry and command processing (TCP II) beta computer was provided by the Echo DSS to the Pioneer DSS (SPS 37-41, Vol. III, p. 116).

With pass 24, September 9, 1966, the Echo DSS assumed the *Pioneer VII* prime tracking on a daily basis, until pass 46 on October 1, 1966. An extended mission tracking on an as-scheduled basis is currently being performed three to four days a week.

**4. Mariner IV Mission**

The *Mariner IV* spacecraft, currently in the twenty-third month of its flight, continues to be tracked jointly by the Mars DSS and Venus DSS. During a scheduled monthly track, two-way lock-up is established, commands are transmitted, and telemetry is received and recorded. The Mars DSS performs the tracking, necessary command transmissions, and receiving, using the JPL R&D maser and receivers (SPS 37-39, Vol. III, p. 112). The data are microwaved to the Venus DSS for processing. During October 1966, a series of low-level telemetry experiments were performed by the two stations (SPS 37-42, Vol. III, p. 92).

**5. Atlas/Centaur Project**

The ninth in the series of *Atlas/Centaur* second-stage booster tests (A/C 9) was launched from Cape Kennedy, Florida, on October 26, 1966. The Pioneer DSS participated in the test, tracking the spacecraft for 4.5 hr during the first pass on October 27. Recorded telemetry data were forwarded to JPL for processing.

**N67 15924**

**B. Facility Construction and Equipment Installation, J. Orbison**

**1. Pioneer Deep Space Station**

The MSFN equipment installation and system testing are progressing. The RF switching box, enabling rapid transfer of the antenna and antenna-associated equipment, has been installed and operationally tested. The tower and antenna for the microwave link between DSS 11 and the Apollo Station are installed and operating.

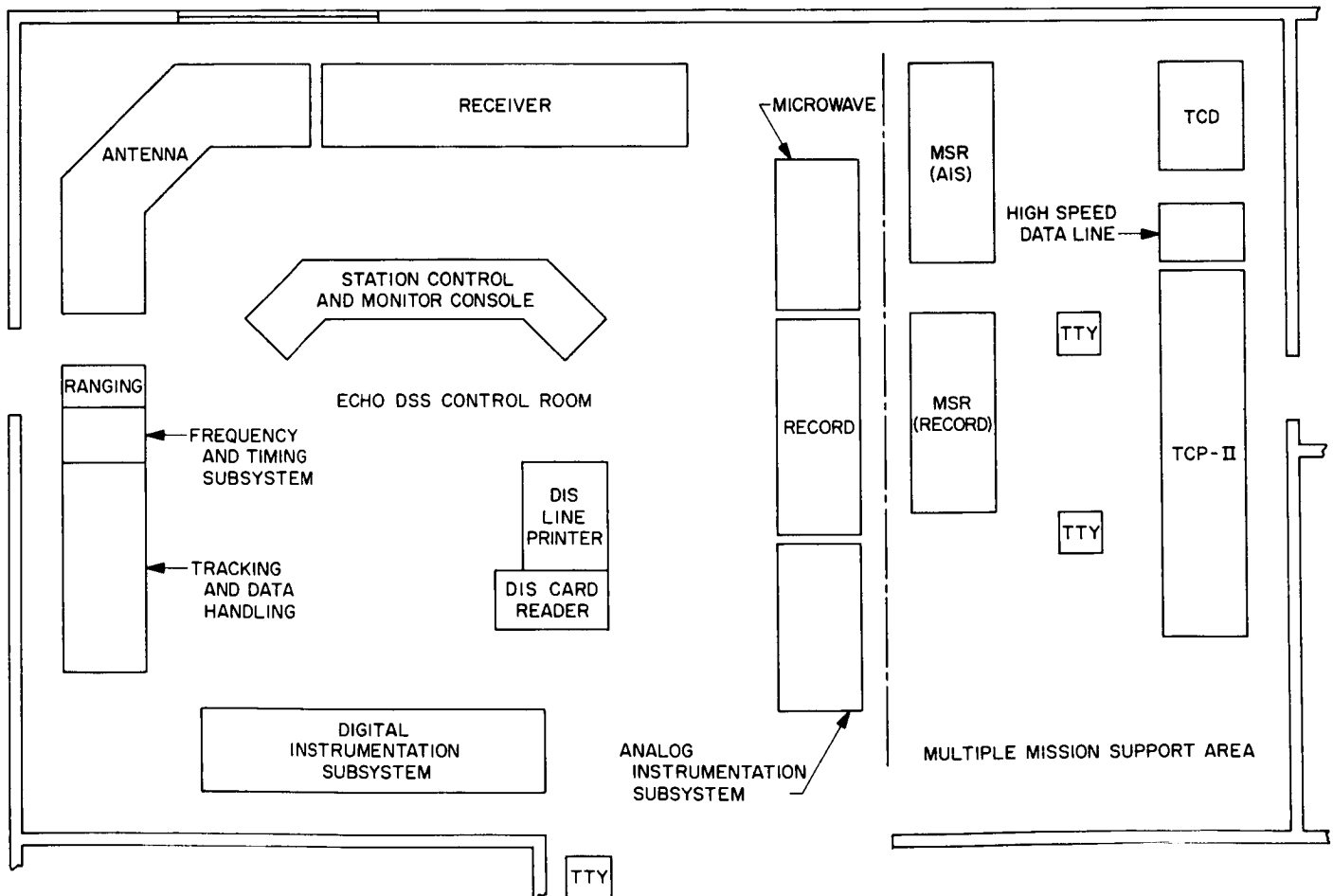


Fig. 1. Typical DSIF control room equipment location

Trenching for the underground primary power distribution system, temporarily halted during the *Surveyor II* mission, is again in progress. All primary power cables, to be placed in conduit in concrete tunnels accessible through strategically located manholes, will lead to both wings of the control building and other buildings of the station.

Installation of the waveguides and the RF power combiner for the dual transmitter (*SPS 37-41*, Vol. III, p. 122-124) on the antenna is in progress. Masers 1 and 2 have been installed on the antenna, and maser 1 is fully operational in the GSDS configuration. Maser 2, which replaces the S-band system parametric amplifier, is currently in the final assembly stage in preparation for operational testing.

Equipment of the S-band system requiring certification was routed through the Goldstone calibration, certification, and maintenance facility, following the termination of the *Surveyor I* mission. Many of the Pioneer DSS S-band receiver modules are the original pilot modules, which were calibrated and certified to establish operational levels comparable with the latest S-band systems. Concurrently, to provide an area for the new equipment, relocation of racks at the multiple mission support area (MMSA) continued. At present, the two racks for the telemetry and command data (TCD) handling are installed. Fig. 1 illustrates a typical control room configuration, including the MMSA.

## 2. Echo Deep Space Station

The MMSA/mission support recording (MSR) equipment has been installed and operationally tested. The rack rearrangement of the microwave, recording, and analog instrumentation subsystems to provide area for the installation of the MMSA/MSR also necessitated moving the communications teletype equipment to the alcove of the control room.

Construction of the commercial power line from the substation north of the Fort Irwin Army Air Field to the Tiefert Peak collimation site began in September 1966. Approximately 2 mi of poles have been set across the relatively flat part of the desert, and drilling for the pole-line up the ridge to the collimation site is in progress. Because of the extremely rugged and steep terrain (Fig. 2), men and equipment are transported to the work area by helicopter. The ridge poles will be set and the cable strung in the same manner.

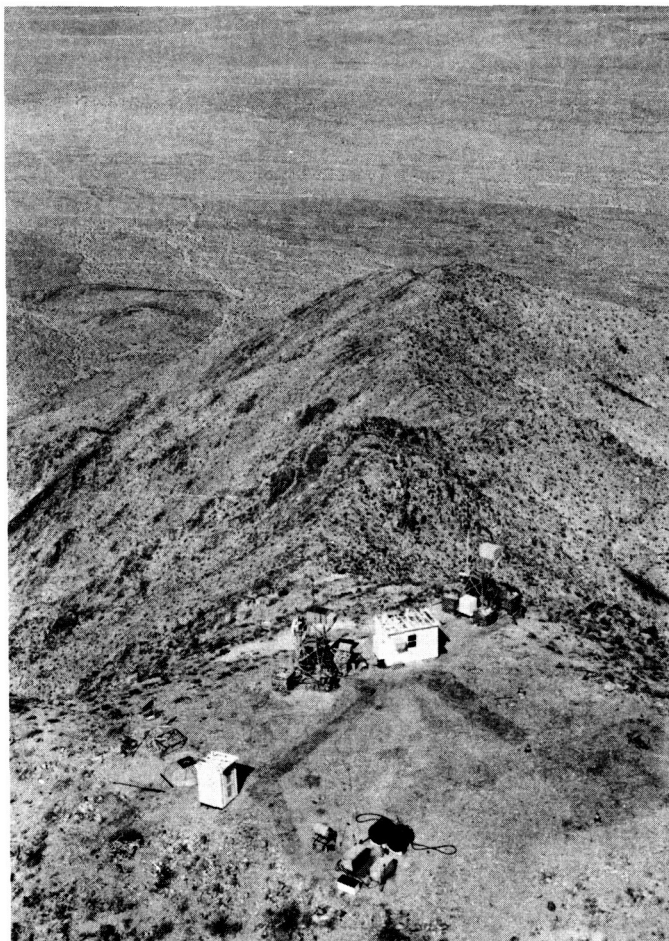


Fig. 2. Aerial view of the Tiefert Peak collimation site and power line area

## 3. Mars Deep Space Station

Except for the maser and associated equipment not presently in use, installation and operational testing of the S-band system are nearing completion. Operational testing of the subsystems is taking place during the *Pioneer VI* tracking. Station personnel are assisting in the hydrostatic bearing alignment, the master equatorial alignment and calibration, and the installation and alignment of the auto collimator in the independent reference structure (IRS) which is associated with the master equatorial.

The transfer from station power to commercial power at 10:10 PDT on October 19, 1966, marked the completion of the commercial power installation. Construction of the underground cabling (Fig. 3) from the pole-line terminal to the substation had been completed earlier.



**Fig. 3. Mars DSS underground commercial power line construction**

The backup 1126-kw diesel generator brought to the Mars DSS during the period that the three 500-kw diesel generators were being rebuilt (*SPS 37-41*, Vol. III, p. 121) was shut down and prepared for shipment. Investigation and testing of the torque problem in the 500-kw units continue; however, two 500-kw units are currently available as emergency backup to the commercial power.

#### **4. Venus Deep Space Station**

Construction of the laboratory and office building (G-60) is essentially completed (Fig. 4) and occupancy took place late in October.

**N67 15925**

#### **C. *Mariner Venus 67* Project: Ground Instrumentation for Occultation, G. Levy**

Although the ground instrumentation for the *Mariner Venus 1967* project will be similar to that used for *Mariner IV*, there will be marked differences due to the very dense nature of the Cytherean atmosphere. The prime station for the occultation measurements will be the DSS 14 210-ft advanced antenna system (AAS).

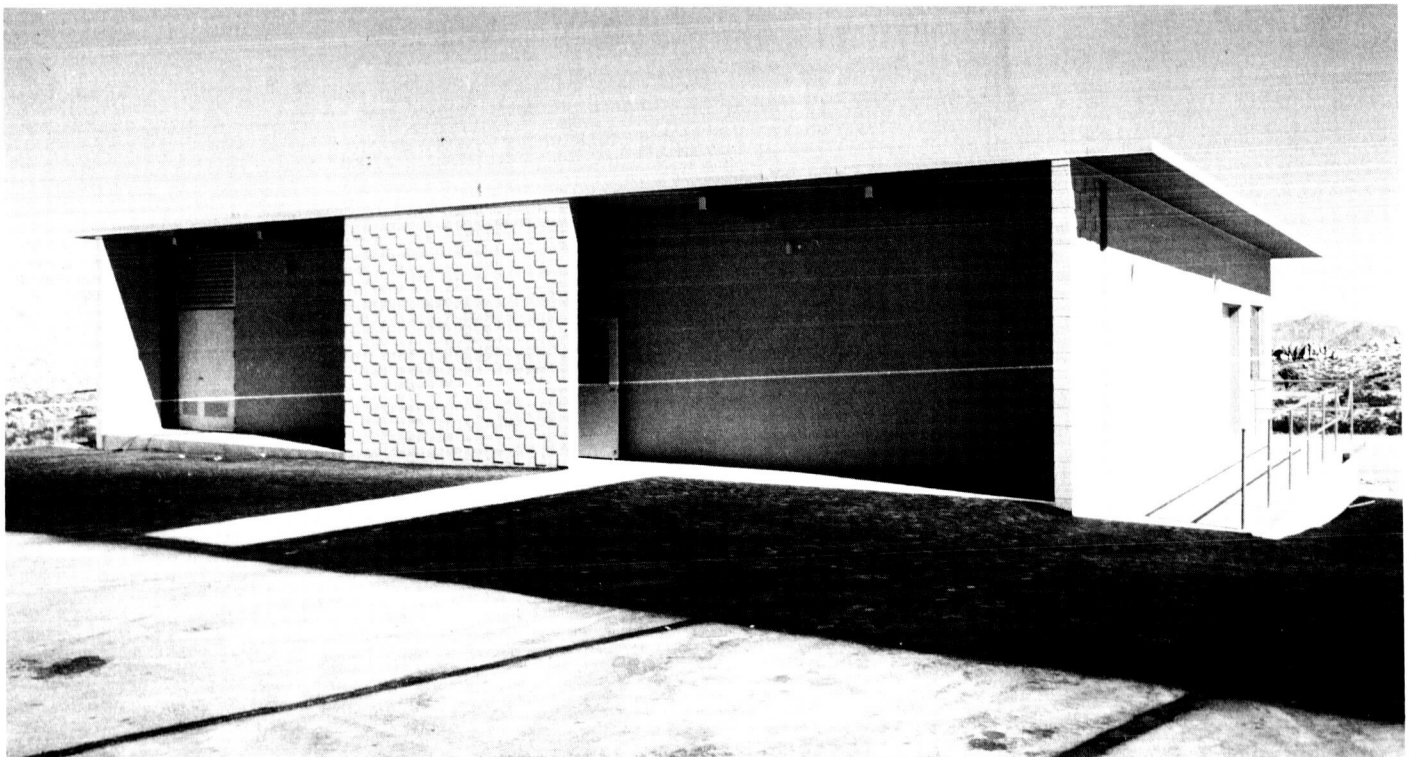


**Fig. 4. Completed laboratory and office building at Venus DSS**

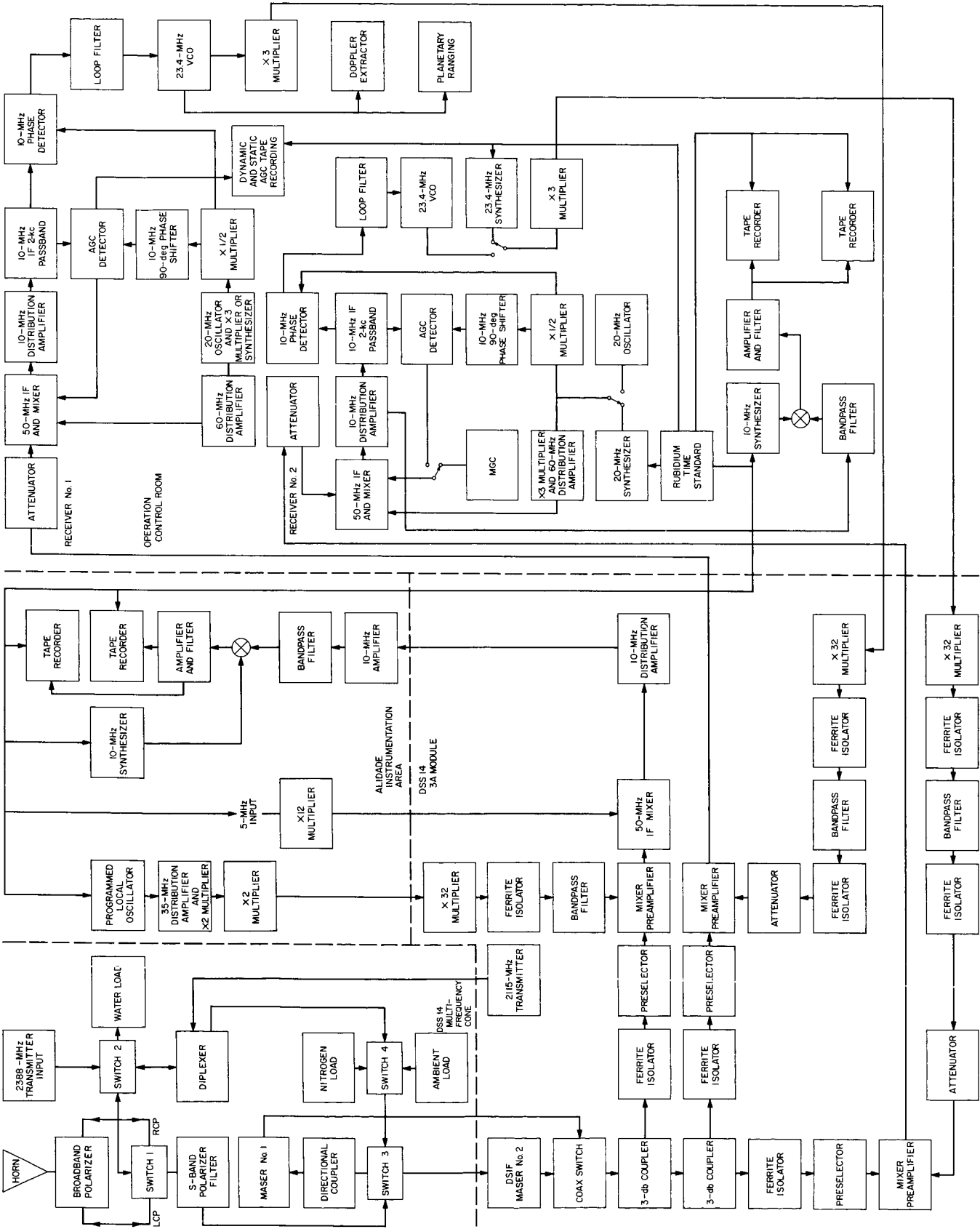


Fig. 5. Mariner Venus 67 DSS 14 occultation configuration

DSS 11 will receive doppler data in the normal configuration, and DSS 13 will have an open-loop receiver.

Because of the high atmospheric density of Venus, doppler perturbations of the order of 30 kHz are expected (in contrast to 3 Hz, one way, in the case of the *Mariner IV*). In addition, the atmosphere also acts as a defocusing lens which produces refractive attenuation estimated to be as high as 26 db. To ensure the most favorable possible signal-to-noise ratio, the 210-ft AAS site has been chosen as the prime station.

The preliminary *Mariner Venus 67* DSS 14 occultation configuration (Fig. 5) shows three separate receivers being employed. Receiver one will be the standard phase lock loop DSIF configuration and will be used for telemetry and doppler data acquisition. Receiver two will be a slightly modified standard receiver with fixed tuned local oscillator derived from the frequency standard by using a synthesizer. The 10-MHz IF of this open loop receiver will be frequency-translated to the 10- to 200-kHz region and recorded. This bandwidth is necessary because of the uncertainties in the expected signal as well as anticipated frequency shifts due to the planetary atmosphere and the orbit. In addition to the two DSIF receivers, a third receiver, the alidade instrumentation area receiver, is illustrated. This receiver has a programmable local oscillator which may be used for the occultation experiment.

At present a simulator is being constructed to produce the expected signal frequency and power fluctuations. In addition, DSS 11 will obtain telemetry and doppler data and DSS 13 will have an open loop receiver and a special low noise "Ultra-cone." The Ultra-cone will be a listen-only configuration and will have a zenith system temperature of 20°K or less.

N67 15926

**D. Venus DSS Operations, M. A. Gregg, E. B. Jackson, and A. L. Price**

**1. Experimental Activities**

During the period from August 16 through October 14, 1966, the major activities at the Venus DSS (summarized in Table 1) were bistatic (with the Mars DSS) planetary radar experiments, radio source evaluation (using the Venus DSS 85-ft AZ-EL antenna), and reception from and transmission to the *Mariner* spacecraft. Additionally, certain improvements were effected in the station antennas, buildings, and equipment.

**Table 1. Summary of Venus DSS activities (August 16–October 14, 1966)**

Activity	Hours	Per cent
Primary experiments		
Planetary radar (Venus bistatic)	49	3.40
Secondary experiments		
Radio source temperature calibration	608	42.22
Mariner experiments		
Transmission, reception, and testing (including time required to change Cassegrain feed cone)	50	3.47
Testing, calibration, construction, and maintenance	709	49.24
Holidays and scheduled nonoperating time	24	1.67
Total	1440	100.00

The cooperative, with Mars, tracks of the *Mariner* spacecraft continued to return telemetry data, spectrograms, and some doppler measurements. These tracks usually involve reception at the Mars DSS, with any necessary transmissions being accomplished by the Venus DSS. However, a low-level, low-speed telemetry simulation experiment with the *Mariner* spacecraft required weaker signals than were available from the Mars antenna. To accomplish this experiment, the Venus R&D Cassegrain feed cone, with the maser retuned to 2297.5 MHz, was used for reception of the *Mariner* spacecraft in both the one- and three-way modes. Signal strength measured at the Venus DSS in this mode was -177.6 dbm.

In addition to the signal strength measurements made on the *Mariner* spacecraft during the reception at Venus, some data were obtained on spacecraft-transmitted frequency drift rate in the one-way mode. These data were a series of 1-min integrations taken at 4-min intervals and plotted against frequency using a 29.3-Hz sampling bandwidth. The results (shown in Fig. 6) indicate that the frequency received by the Venus antenna drifted downward approximately 1.7 Hz in 20 min. Fig. 7(a) illustrates a spectrum of the spacecraft-received frequency and shows the first pair of sidebands as well as the carrier. Fig. 7(b) illustrates the carrier alone, integrated over a 31-min period.

The planetary radar experiments, with Venus as the target, were the first attempted by JPL with Venus approaching superior conjunction at a one-way range of approximately 1.632 AU. Total spectrum and ranging measurements were made using a range gate depth of 1000 μsec and disclosed that the planet Venus was

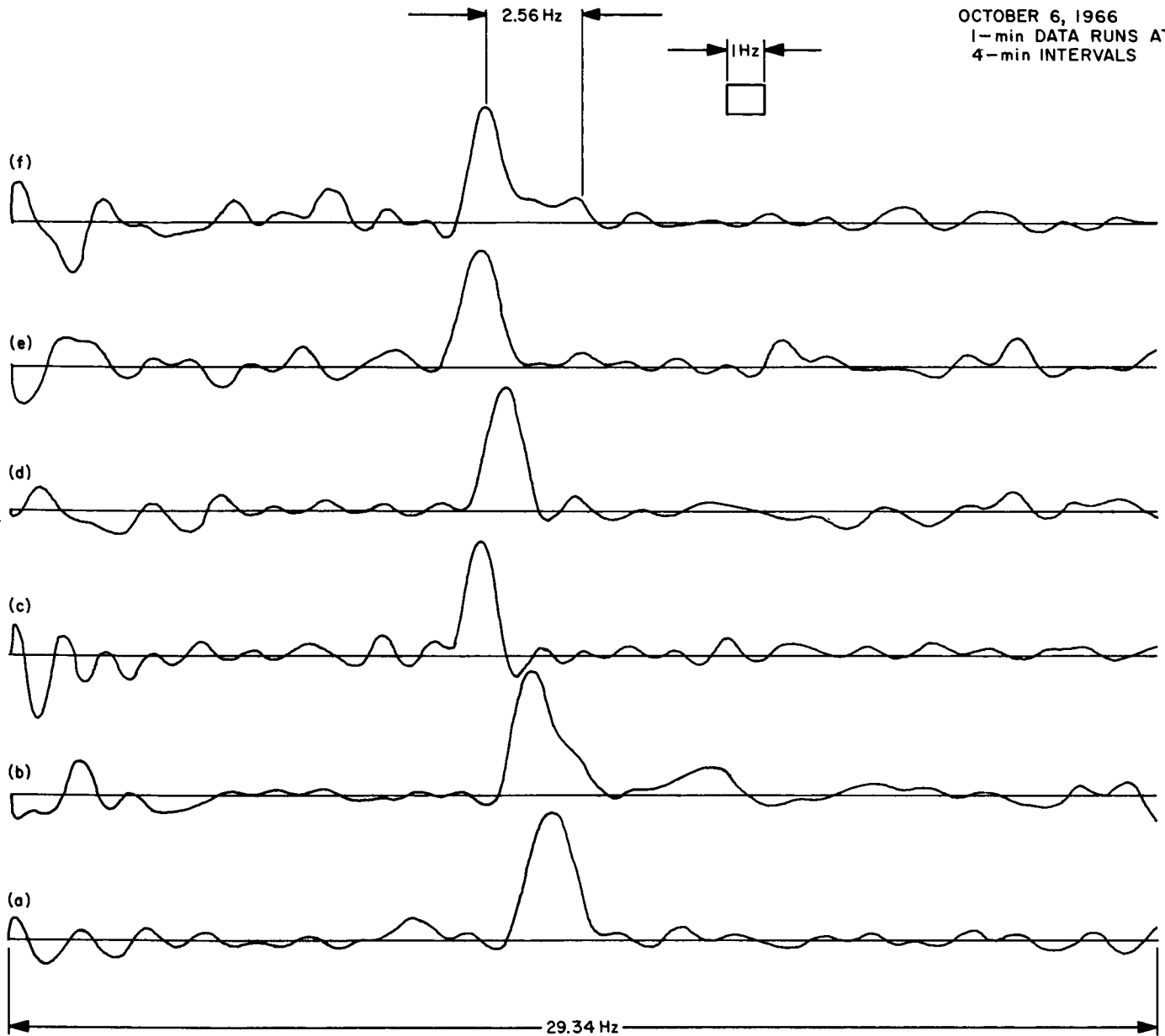


Fig. 6. Mariner Mars 1964 spacecraft, carrier only, showing frequency drift in one-way mode

approximately  $9000 \mu\text{sec}$  (round trip) closer than predicted by the JPL master ephemeris. However, because of insufficient signal strength, accurate measurements could not be made.

## 2. Subsystem Performance

**a. 100-kw transmitter (operation).** During this period, the R&D transmitter operated a total of 239.7 filament hours and 110.4 beam hours for the Mercury and Venus bistatic radar experiment. A few weeks were devoted to intensive training of personnel in operations and maintenance

of the transmitter systems and the associated equipment, both S-band and X-band.

**b. Mariner 100-kw transmitter.** The Mariner transmitter has operated a total of 33.8 filament hours and 25.8 beam hours with no inter-lock operations or loss of tracking time.

**c. Receiving systems.** Although the X-band receiver (8448 MHz) was not used during this period, the 2388-MHz receiver was used in planetary experiments and

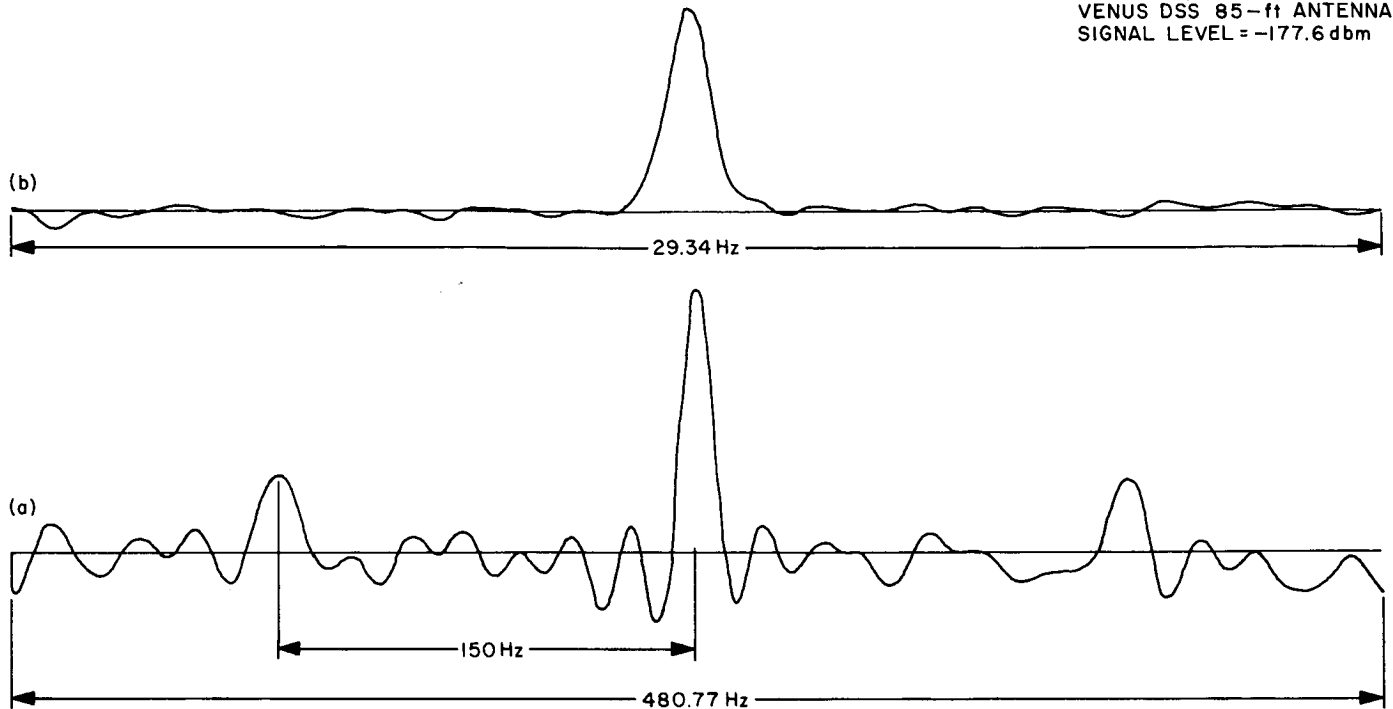


Fig. 7. Mariner Mars 1964 spacecraft, one-way mode, carrier plus sidebands and carrier alone

radio source evaluation. The receiver was used in its monostatic mode at the Venus DSS and in its bistatic mode in conjunction with the Mars DSS 2388-MHz R&D receiver. In the latter, the 455-KHz signal from the Mars DSS receiver is fed, via the microwave link, into the AM channel and the main loop channel of the Venus DSS 2388-MHz receiver.

Reception of signals from the *Mariner* spacecraft was accomplished using both the Venus DSS *Mariner* receiver (for one-way and three-way reception) and the Mars DSS 2295-MHz receiver (for one-way and two-way reception). As before, the 455-kHz signal from the Mars receiver was fed, via the microwave link, into the 455-kHz portion of the Venus Mod IV receiver.

With the exception of one failure which involved the loss of output from the bias-up synthesizer, operation of the programmed local oscillator remained satisfactory throughout this period. The failure was repaired on-site, and normal operation was restored.

Two failures occurred in the central frequency synthesizer (CFS). One was concerned with the +30-v power supply voltage vigilant unit which senses large changes

in the power supply output voltage. Although troubleshooting is now underway, it should be noted that the failure of this unit does not affect the power supply output. The other failure resulted in excessive static phase error in the 35.075-MHz reference loop. A faulty voltage-controlled oscillator was repaired, and operation was returned to normal.

### 3. System Improvements

*a. Antennas.* To improve appearance and to provide additional storage space an enclosure to contain moving portions of the cable wrap-up has been added to the 30-ft AZ-EL antenna. Also, the complete antenna structure, with the exception of the surface of the dish, has been painted white to improve appearance and to reduce structural deformation due to thermal gradients.

During the month of November, operation with an X-band cone at a frequency of 8488 MHz will commence on the 85-ft antenna. To improve performance at this frequency, thermal gradients have been minimized by complete repainting of the antenna.<sup>1</sup>

<sup>1</sup>According to JPL Specification 1006B (modified).

**b. 100-kw transmitter.** The solid-state rectifiers for the 100-kw S-band transmitter were removed and replaced with the tube rectifiers to allow the testing of the individual diodes in the stacks and replacement of defective diodes before shipping the stacks for installation in the new solid-state rectifier equipment to be used for the 400-kw system. Some tube rectifiers were lost through improper cooling and were replaced with existing spares. The inter-lock circuitry was modified to prevent this from re-occurring.

**c. Receiving systems.** To provide dual frequency receiving capability in one antenna cone, the 2295- to 30-MHz converter and power supply were removed from the *Mariner* cone and installed in the 2388-MHz R&D cone. Appropriate cabling was also installed, thus providing the two converters independent control and signal functions. A 400-cycle power cable change is the only modification required to switch reception from one frequency to another.

Because of continuing tape-reader problems in the digital portion of the programmed local oscillator, a complete mechanical and electrical overhaul of the tape reader and tape spooler was performed during this period. Modification of the tape-reader lamp power supply greatly improved operation of the reader.

**N67 15927**

#### **E. DSIF FR-900 Video Recorders, W. C. Allen**

Three DSIF stations—DSS 12, DSS 61, and DSS 41—are equipped with Ampex FR-900 rotary-head magnetic recorders capable of acquiring video data from the *Lunar Orbiter*. The machine presently installed at each site has a single wideband channel and two auxiliary tracks. The wideband can record either one channel of dc to 5.5-MHz data in an FM mode or one channel of data within a 1- to 10-MHz bandpass in a direct-record mode without bias. The *Lunar Orbiter* video data are acquired from an unrestricted 10-MHz output of the S-band receiver at approximately -10 dbm, amplified to +3 dbm and predetection-recorded directly on the FR-900. Each of the two auxiliary tracks has a 30-kHz bandwidth, on which are recorded a station voice-communication channel and serially coded GMT. A recording of approximately 1 hr can be made on 3800 ft of the 2-in.-wide video tape.

The FR-900 is a complex electromechanical device incorporating three servos that control (1) the head drum rotation, (2) the longitudinal tape speed, and (3) two

electrically variable delay lines. During record, the 2-in. video tape is moved at a constant speed of 12.5 in./sec from the supply reel to the take-up reel by means of a capstan drive assembly, while wideband data are being recorded transversely across the width of the tape by either a rotating scanning assembly or a head drum. The capstan and head drum motion are separately controlled by hysteresis synchronous motors driven by signals derived from a crystal-controlled frequency standard. The wideband response is achieved primarily by a head-to-tape speed of over 1500 in./sec as a result of the rotary-head speed of 14,640 rpm.

When a recorded tape is being reproduced, it is essential that the longitudinal motion of the tape and the transverse motion of the rotating heads be tightly controlled so that the recorded tracks are accurately scanned. To accomplish this, a control track is recorded along one edge of the tape to mark each revolution of the head drum during the recording process. During reproduction, the head drum can then be rotated at constant velocity and the capstan speed can be servo-controlled so that one control-track pulse is reproduced for each revolution of the head drum. This reestablishes the ratio of longitudinal-to-transverse motion that existed during recording and assures accurate registration of the reproduce heads on the recorded tracks.

An additional time-base reference or *pilot* signal is recorded transversely along with wideband data. When reproduced, this pilot is used as a time-base reference for control of head-drum rotation and permits additional electronic time-base correction of the reproduced data through electrically variable delay lines. The pilot is recorded below the information spectrum at 500 kHz to avoid interference with the video signal. Precision time-base control is a principal feature of the FR-900 recorder/reproducer system that makes possible the recording and reproducing of time-stable wideband information. When data are reproduced, the peak-to-peak time-displacement error is less than  $\pm 25$  nsec with respect to the system-timing reference. The two auxiliary channels are recorded in the conventional longitudinal manner along one edge of the tape, using a direct-record-with-bias technique.

The *Lunar Orbiter* video data recorded at 10-MHz center frequency has a peak phase modulation index of  $\pm 4$  rad. Information sidebands extend more than  $\pm 1.24$  MHz about the 10-MHz carrier frequency and include a 310-kHz video subcarrier modulated with video data

confined to a 230-kHz passband, a 38.75-kHz demodulator pilot reference, and a 30-kHz engineering data sub-carrier.

During the first *Lunar Orbiter* mission, approximately 300 magnetic tapes containing the above data were successfully recorded by the DSIF stations using the 10-MHz predetection record mode. Tapes recorded by the DSIF are processed at Langley Research Center, Hampton, Virginia, where film records are made for routine analysis; and magnetic tape dubs of the detected video are made for digital analysis at the Manned Spacecraft Center, Houston, Texas.

**N67 15928**

#### **F. DSIF Station Control and Data Equipment,**

*R. Flanders, G. Jenkins, A. Burke, W. Frey, and H. Baugh*

The DSIF station control and data equipment (SCDE) was introduced and described in *SPS 37-41*, Vol. III, pp. 124-127. The Space Programs Summaries will continue to be used as the reporting medium for the status of SCDE implementation; this article presents the status as of October 1966.

The SCDE consists of the following specific subsystems: (1) antenna pointing subsystem, (2) digital instrumentation subsystem, (3) station control and monitor console, (4) telemetry and command processor, and (5) frequency and timing subsystem. The functional objective of the equipment is to provide the capability for processing spacecraft telemetry and command data in direct mission support, to perform station monitoring, time tag data, supply reference frequencies, and to perform antenna pointing as mission-independent support.

##### **1. Antenna Pointing Subsystem**

The antenna pointing subsystem (APS) has been installed and is operational in its interim configuration at DSS 12, 14, 41, 42, and 62. Installation of interim APS (IAPS) equipment at DSS 62 and 72 will be completed during the fourth quarter of 1966. The hardware and software capabilities of the IAPS are described in detail in *SPS 37-38*, Vol. III, pp. 74-76. The following additional tasks have now been accomplished.

*a. Update of IAPS computer program.* An updated version of the IAPS program (DOI-5107-OP-A) has been submitted to the DSIF computer-program library. This new program will replace the existing IAPS program (DOI-5107-IN), performing the same functions as the

original program with the following additions and changes.

*Drive-tape reasonable-data-check option.* The new program performs a check on the data on the drive-tape input. This new feature is a program option which may or may not be used, depending on the setting of computer breakpoint switch 2. If it is turned to RESET, the program performs the reasonable data check; if it is turned to SET, the program does *not* perform the reasonable data check.

The reasonable data check looks at the angular data on the drive-tape samples and determines if it is acceptable for use in pointing the antenna. The program performs at straight-line extrapolation on existing data points to predict a new data point. When the new data sample is read into the computer, it is compared with the predicted value. The new angle data must agree with predicted data with an allowable tolerance of the antenna pointing beamwidth or it is rejected by the computer program. If a sample is rejected, the program will search the drive tape for the next valid sample before it will process the angular data contained on the tape. This modification to the program will eliminate the possibility of pointing the antenna to erroneous angles that are introduced on the drive tape as a result of teletype transmission errors when the antenna-pointing prediction information is sent to the DSIF stations.

*Drive-tape input-format option.* The new program has the option of reading either a drive tape generated by the teletype predict reformatting program (DOI-5004-OP) or the teletype tape as it is received by the station without using the reformatting program. The type of tape that will be accepted by the IAPS program is controlled by computer breakpoint switch 1 as follows:

If breakpoint switch 1 is at RESET, the IAPS accepts a drive tape that has been generated by the teletype reformatting program; if it is at SET, the IAPS accepts a drive tape as it is received by the station without using the teletype reformatting program.

This option allows the IAPS operator to bypass the time-consuming process of using the teletype reformatting program to generate drive tapes.

*Pointing after one real-time sample pull.* The new program generates commands to point the antenna after one real-time tape sample pull instead of two as was required in the original program. This method reduces

Except for the countdown clock, SMC Phase I is essentially complete. Problems have been encountered in the procurement of components to be used in Hi-Rel circuit modules from which the clock is to be made and are causing this portion of SMC Phase I to be approximately six months behind schedule.

The prototype program alarm and control panel has been delivered to DSS 11, where it is being evaluated. Follow-on procurement for five additional panels should be complete by March 1967. The graphical recorder should be delivered by December 1966 and evaluation completed in early 1967. Follow-on procurement should be initiated early in fiscal year 1968.

#### 4. Telemetry and Command Processors, Phase II

The telemetry and command processors, Phase II (TCP II) are the major assemblies in the telemetry and command data handling subsystem, Phase II (TCD II). A description of the TCP II has been presented in SPS 37-38, Vol. III, pp. 76-77. The major changes in TCP II during this period are as follows:

- (1) The TCP II-B configuration now operational at DSS 51 will be changed to the standard TCP II. Procurement has been initiated for the required computers, and it is estimated that the changeover will take place in mid-1967.
- (2) Procurement of analog to digital converters (A/DCs) for installation at DSS 11 and DSS 12 has been initiated. The addition of these units to the TCP II will provide a needed capability for additional flight project support. A/DCs will be added to the remaining Deep Space Stations at a later date.
- (3) A fourth teletype channel has been scheduled for addition to the TCP II communications buffer. The addition of this channel, scheduled for March 1967, will provide the capability for data transfer between the TCP II and the DIS.
- (4) TCP II implementation has been proceeding on schedule and is in agreement with Table 2, p. 126, SPS 37-41, Vol. III. The only change to this table is the configuration change (from TCP II-B to the standard TCP II) at DSS 51.

#### 5. Frequency and Timing Subsystem, Phase II

The design of frequency and timing subsystem, Phase II (FTS II) is now in its final phase and is estimated as 80% complete. An expanded block diagram is being prepared

which will show details of design in the digital divider and clock areas, as well as an expansion of the functional blocks in the simulation and frequency standard sub-assemblies. The functional specification should be ready for release by the end of the year.

Procurement of components for the digital modules is almost complete, with approximately 30% of the required parts now on hand. The Varian R20 rubidium frequency standard has been delivered and is currently under test. The most recent results indicate that performance is within specifications. However, there are still some problems involving the microphonics and the physical characteristics of the equipment, and these are undergoing thorough investigation at the standards laboratory at Goldstone.

FTS II progress is within scheduled guidelines, as indicated at the design review; the specific problem areas discussed at that time are in the process of being resolved. Of particular interest at that time were the configuration of the timing portion of the simulation equipment and the definition of voltage and current levels at the FTS II simulation interface.

Prototype fabrication is scheduled for the first quarter of calendar year 1967.

#### **N67 15929** G. Conference Nets of the Operational Voice Communications Subsystems, F. E. Bond, Jr., and J. W. Capps

This paper provides an overall description of the management, configuration, and control of the operational voice communications subsystem (OVCS), which is a communications capability of the SFOF, fulfilling the requirement of end terminations and internal distribution of audio intelligence. Since this is a leased facility, JPL and associated contractor personnel may not relocate, move, disconnect, nor alter in any way, any of the equipment associated with this communications subsystem<sup>2</sup>.

The OVCS provides (1) touch-tone signaling telephones, (2) voice conference nets (for talk-listen headsets/handsets and speakers), and (3) point-to-point intercommunications.

Any person directly involved in space flight operations in the SFOF has three voice communications interfaces:

<sup>2</sup>Configuration changes may be made only under the procedures outlined in SFOF/SOP 10-201A.

the initialization time required in the drive tape mode by one sample interval time.

*Station visibility check in the star-track mode.* The new program performs a check in the star-track mode to determine if the star to be tracked is visible to the local station. If the star is not visible, the program zeroes all command registers and waits for the subsystem operator to enter a new set of coordinates. The criteria to determine station visibility are as follows:

- (1) Local hour angle is between  $\pm 90$  deg.
- (2) Declination is between  $\pm 90$  deg.
- (3) Local elevation angle is  $> 0$  deg.

*b. Ascension Island (DSS 72) antenna pointing program.* A new antenna pointing program (DOI-5244-OP) has been written for DSS 72. The DSS 72 program is essentially identical to the antenna pointing program (DOI-5107-OP-A) that will be used at DSS 11, 12, 41, 42, 51, 61, and 62. The major difference between the two programs is in the star-track mode. The Ascension Island program generates commands to point the antenna in the azimuth/elevation coordinate system, while the program for the other DSIF stations generates commands in the polar coordinate system. This change is necessary to point the 30-ft azimuth/elevation mounted antenna at Ascension Island.

The final configuration antenna pointing subsystem (APS I), described in *SPS 37-38, Vol. III*, will be installed at DSS 14, beginning November 1, 1966. Hardware and software checkout will continue for approximately two months. The APS I is scheduled to be operational at DSS 14 by January 1, 1967.

## **2. Digital Instrumentation Subsystem, Phase II**

The digital instrumentation subsystem, Phase II (DIS II) prototype design is currently being evaluated, prior to processing the procurement for subsequent units. The DIS II configuration is an extension of the DIS I, and provides the capability for performing the DSIF system monitoring functions under control of the system monitor program. The DIS II is composed of the following major functional elements: (1) SDS 920 digital computer, including peripheral equipment, (2) computer ancillary input/output devices, (3) magnetic tape recording apparatus, (4) data gathering equipment, (5) communications buffer, and (6) alarm, control, and display elements.

The primary objectives of the subsystem are grouped into three general categories: (1) performance- and status-data presentation, (2) alarm monitoring for failure detection, and (3) preparation of permanent historical record of station performance.

The present effort involves definition of the subsystem functions, determination of the hardware configuration to accommodate these functions, establishing the monitor system program criteria, definition of the subsystem interface characteristics, and preparation of supporting documentation requirements prior to initiation of a procurement. These activities entail the selection of critical station parameters for alarm monitoring and display. Formats for periodic reports and alarm messages are being established to present information in an optimum manner for interpretation by station operating personnel. The principal functional elements of the system monitor program are being established to permit work to proceed on the actual program implementation. Formats for teletype and high-speed data messages transmitted or received external to the station are being coordinated with cognizant personnel to assure compatibility with the ground communication system requirements, the terminal equipment, and the ultimate recipient of the messages. Similarly, compatibility in the form and format of station performance data recorded on magnetic tape is to be established to permit post-mission processing for analysis at the SFOF. The present monitoring capability of the DIS I, under control of the interim monitor program, has no provision for communication of station performance and alarm messages to the SFOF. The definition of these functions is now being undertaken, along with a major expansion in the system functions to be monitored and displayed for DSIF station operating personnel.

The procurement for subsystem supporting documentation is being processed simultaneously with the subsystem hardware procurement to alleviate installation and testing difficulties and to provide complete operation and maintenance procedures at the time of installation.

## **3. Station Control and Monitor Console**

The station control and monitor console (SMC) subsystem provides a centralized location for the station manager to monitor critical station functions and to control station operations by directive. The SMC has five 17½- by 19-in. display-panel surfaces. The SMC displays mission-independent data for the most part; however, it provides for certain mission-dependent display areas. No control functions are available at the SMC.

- (1) To the higher level of authority (first order).
- (2) To lateral levels of authority (second order).
- (3) To subordinate levels of authority (third order).

The first level represents the requirement for the space flight operations director (SFOD), and assistants, to properly direct the supporting elements of his mission. To fulfill this requirement, the "command net" of any given project must be provided to each supporting agency—e.g., Comm, Flight, or Track. It should be noted that this prime net is furnished by the project supported. Business transacted on this net should be restricted to that necessary to control, direct, and determine mission status for the particular project involved.

The second level represents the requirement for the directors of the major supporting agencies, themselves, to transact business. Each supporting agency has been provided with a "home net" which is accessible to the remaining agencies. The concept in this case is that each agency will monitor and receive calls from any other lateral agency *only* on his home net, a mandatory require-

ment that eliminates any one person from being responsible for monitoring (and responding) on a multitude of nets. Business transacted on these second-order nets should be restricted to matters of immediate concern to the two parties conversing.

The third level represents the requirement for a supervisor at any specific location to control those personnel directly under his supervision. For the most part, these "internal nets," should be restricted to the pertinent area, room, or activity concerned.

Net custodians have been assigned to all existing OVCS voice conference nets. Custodial control is defined as the authority to determine fixed net configurations. All requested changes to a specific voice net will be approved by the assigned net custodian prior to implementation. Assigned custodians are listed in Table 2, which also reflects the presently existing OVCS voice conference nets.

Documentation of the current configuration of the OVCS is provided, and updated for all net custodians.

**Table 2. OVCS voice conference nets**

No.	Name	Category	Type	Custodian
3	ETR	MI	OCC	D. G. Tustin
This net is normally interconnected to a scheduled voice line to AFETR and is used to coordinate flight data between the FPAC at JPL and the RTCF at AFETR. It may also be used for discussion between the SFOF and JPL operations at AFETR. When not connected to AFETR, this net may be used as a backup net for facility or project use as scheduled.				
4	STATUS	MI	OCC	D. G. Tustin
This net is normally interconnected to a scheduled voice line to AFETR and is used to report spacecraft range, countdown, and launch status to the SFOF from AFETR and to report DSN and SFO status to the AFETR from the SFOF. When not connected to AFETR, this net may be used as an internal distribution net, under the cognizance of the operations control chief (OCC), either for backup purposes or for wide distribution of audio data.				
15	DSN	MI	OCC	D. G. Tustin
This is the home net where the DSN-OCC (OPSCON) may be reached when on duty. It will be used for overall coordination of the DSN by the OCC and the operating system chiefs, and may be used by the latter for interface coordination.				
20	COMM 1	MI	COMM	C. P. Le Veau
This net is used for coordination purposes to establish voice contact to various elements of the DSN communications center from both DSN and project personnel.				

No.	Name	Category	Type	Custodian
16	COMM 2	MI	COMM	C. P. Le Veau
This net is used as the prime internal net of the DSN communications center to permit coordination of operational internal matters within this agency.				
47	COMM 3	MI	COMM	C. P. Le Veau
This net is used as a maintenance/engineering net to which external activities are connected during those periods when communication-to-communications contact is required.				
36	COMM CONF	MI	COMM	C. P. Le Veau
The purpose of this net is threefold: (1) to provide a facility whereby groups may effect a conference with the DSS stations or other outside agencies without interfering with project-oriented nets; (2) to provide a facility whereby dictation may be received by the TRAKOM teletype operator for teletype transmission during periods of voice circuit failure to the DSS stations in a teletype conference mode; and (3) to provide a listen-only facility to be bridged to other operational nets for the use of visiting personnel.				
30	SIM 1	MI	SUPPORT	D. A. Nelson
This net is used to provide contact between various elements of the SDCC and the remainder of the SFOF.				
51	SIM 2	MI	SUPPORT	D. A. Nelson
This net is used as an internal net to provide contact between the various elements of the SDCC.				

Table 2 (contd)

No.	Name	Category	Type	Custodian
2	DATA 1	MI	DATA	G. R. Emery
<p>The purpose of this net is to provide a communications interface between the project data controller (DaCon) and the operational components of the SFOF data system. For consistency, a given project will usually be supported on the same data net; however, this arrangement will be reassigned in real time by the data chief as required.</p> <p>This net shall not be used at any time for communications between users outside the SFOF data system without the concurrence of the data chief.</p>				
9	DATA 2	MI	DATA	G. R. Emery
<p>This net provides a communications interface between DaCon and the operational components of the SFOF data system. For consistency, a given project will usually be supported on the same data net; however, this arrangement will be reassigned in real time by the data chief as required.</p> <p>This net shall not be used at any time for communications between users outside the SFOF data system without the concurrence of the data chief.</p>				
55	DATA 3	MI	DATA	G. R. Emery
<p>This net provides communications between DaCon and certain operational components of the SFOF data system. This net will be used as assigned by the data chief to supplement coverage provided by the Data 1 and Data 2 nets. Principal usage should be restricted to communications between DaCon and TPS or, in the case of tests conducted entirely within the data system, between DaCon and any operational component which would normally be contacted on the Data 1 or Data 2 net.</p> <p>With the exception of communications interface between DaCon and the data distribution system (DaFlo), this net will not be used at any time for communications between users outside the SFOF data system without the concurrence of the data chief.</p>				
56	DATA 4	MI	DATA	G. R. Emery
<p>The purpose of this net is to provide communications between DaCon and certain operational components of the SFOF data system. This net will be used as assigned by the data chief to supplement coverage provided by the Data 1 and Data 2 nets. Principal usage should be restricted to communications between DaCon and TPS or, in the case of tests conducted entirely within the data system, between DaCon and any operational component which would normally be contacted on the Data 1 or Data 2 net.</p> <p>With the exception of communications interface between DaCon and DaFlo, this net will not be used at any time for communications between users outside the SFOF data system without the concurrence of the data chief.</p>				
5	DPA 1	MI	DATA	G. R. Emery
<p>This is the home net of the data chief, and shall be used by mission-independent personnel to initiate and carry on communications with the data chief.</p> <p>This net will also be used for communications between the various operations portions of the SFOF data system at the discretion of the data chief.</p>				
54	DPA 2	MI	DATA	G. R. Emery
<p>This net will be used for communications within the SFOF data system only. This net shall not be bridged, or otherwise extended, under any circumstances, into areas of the SFOF that are not in the complete control of the data system.</p> <p>Usage of the DPA 2 net within the ground rules indicated above will be at the discretion of the data chief.</p>				

No.	Name	Category	Type	Custodian
18	DSS 11	MI	DSIF	C. A. Holritz
<p>This net is normally interconnected to a scheduled voice line to DSS 11 and is used to coordinate flight data between the SFOF and DSS 11.</p>				
19	DSS 12-1	MI	DSIF	C. A. Holritz
<p>This net is normally interconnected to a scheduled voice line to DSS 12 and is used to coordinate flight data between the SFOF and DSS 12.</p>				
25	DSS 13	MI	DSIF	C. A. Holritz
<p>This net is normally interconnected to a scheduled voice line to DSS 13 and is used to coordinate flight data between the SFOF and DSS 13.</p>				
24	DSS 14	MI	DSIF	C. A. Holritz
<p>This net is normally interconnected to a scheduled voice line to DSS 14 and is used to coordinate flight data between the SFOF and DSS 14.</p>				
10	DSS 41	MI	DSIF	C. A. Holritz
<p>This net is normally interconnected to a scheduled voice line to DSS 41 and is used to coordinate flight data between the SFOF and DSS 41.</p>				
11	DSS 42	MI	DSIF	C. A. Holritz
<p>This net is normally interconnected to a scheduled voice line to DSS 42 and is used to coordinate flight data between the SFOF and DSS 42.</p>				
13	DSS 51	MI	DSIF	C. A. Holritz
<p>This net is normally interconnected to a scheduled voice line to DSS 51 and is used to coordinate flight data between the SFOF and DSS 51.</p>				
33	DSS 61	MI	DSIF	C. A. Holritz
<p>This net is normally interconnected to a scheduled voice line to DSS 61 and is used to coordinate flight data between the SFOF and DSS 61.</p>				
49	DSS 62	MI	DSIF	C. A. Holritz
<p>This net is normally interconnected to a scheduled voice line to DSS 62 and is used to coordinate flight data between the SFOF and DSS 62.</p>				
38	DSS 71	MI	DSIF	C. A. Holritz
<p>This net is normally interconnected to a scheduled voice line to DSS 71 and is used to coordinate flight data between the SFOF and DSS 71.</p>				
50	DSS 72	MI	DSIF	C. A. Holritz
<p>This net is normally interconnected to a scheduled voice line to DSS 72 and is used to coordinate flight data between the SFOF and DSS 72.</p>				
53	SDA	MI	DSIF	D. Chaney
<p>This net is normally interconnected to a scheduled circuit to Building 33 at Goldstone and is used for voice liaison between Goldstone, FPAC 1, and scientific data analysts (SDA) in the net control area relative to orbit determinations.</p>				

Table 2 (contd)

No.	Name	Category	Type	Custodian
34	NETCON 1	MI	DSIF	C. A. Holritz
<p>This net is used by DSIF control-room personnel to coordinate their activities on a particular mission. Extensions of this net to other areas are made when DSIF personnel are located in areas outside the DSIF control room.</p> <p>DSIF operations chief assigns use of the net and approves extensions.</p>				
35	NETCON 2	MI	DSIF	C. A. Holritz
Same as Netcon 1.				
17	NETCON 3	MI	DSIF	C. A. Holritz
Same as Netcon 1.				
1	PIONEER COMMAND	MD	PIONEER	J. W. Davis
<p>This is the major Pioneer net, which is used for the control of mission operations within the SFOD, interconnecting the chiefs of all the prime operational and support areas concerned with the Pioneer mission.</p> <p>This net will be used to report the sequence of events as they are accomplished during the launch operations. This will provide the SFOD with a continuing picture of the progress of the sequence of events in support of the Pioneer flight mission before launch, during the boost phase, and during the critical phases of the flight mission. This net will also provide the SFOD with operational readiness reports, establishing areas of responsibility and readiness to support the Pioneer launch operations.</p>				
21	AMES	MD	PIONEER	J. W. Davis
<p>This net is normally interconnected to ARC and is used primarily to provide mission control for the Pioneer flight mission and, secondarily, to provide status reporting for NASA/ARC during the launch operations and the early phases of the Pioneer flight mission.</p>				
22	TRW	MD	PIONEER	J. W. Davis
<p>This net is normally connected to TRW Systems, providing voice communications between the SFOD console at JPL/SFOF and TRW Systems, Redondo Beach, California. This voice net will be made available to the SFOD to discuss areas concerned with the Pioneer spacecraft contractor.</p>				
28	PION COORD	MD	PIONEER	J. W. Davis
<p>The purpose of this voice net is to provide the spacecraft performance analysis team with an internal JPL/SFOF communications system for technical evaluation and reporting of the Pioneer VII spacecraft performance. Nominal and anomalous detailed discussions will be held on this net to provide the SPAC director with the proper information relating to his responsibility.</p>				
52	PION S/C	MD	PIONEER	J. W. Davis
<p>The purpose of this voice circuit is to provide the SFO team with the proper coordination between the flight operations control at JPL/SFOF and the launch operations control at Cape Kennedy Air Force Station (CKAFS). Discussions between TRE 1 at JPL/SFOF and the spacecraft representative at Hangar AM, CKAFS, will be concerned with detailed coordination of launch operations and spacecraft analysis being performed as part of the flight mission operations. This net will also provide the spacecraft analysis team at JPL/SFOF and, in turn, the JPL/DSN with spacecraft frequency report measurements being taken at Hangar AM.</p>				

No.	Name	Category	Type	Custodian
39	FLITE CONT	MD	LUNAR ORBITER	R. B. Rung
<p>This mission control net is utilized by SFOD, area directors, track chief, etc., and carries S/C status, SPAC and FPAC milestone reports, computer configuration, command information, and approval.</p>				
40	FPAA 3	MD	LUNAR ORBITER	R. B. Rung
<p>The FPAC set carries all FPAC business, both inter- and intra-area, using the Boeing Company and JPL personnel. Orbit determination, trajectory, and maneuver information are the prime data carried.</p>				
41	DSS 1	MD	LUNAR ORBITER	R. B. Rung
<p>This net is used to patch tracking station voice nets to all areas. SNOMAN provides patches allowing tracking stations in operation to be heard. DSS 41, 61, and 12 may appear. The communications status display board or SNOMAN correlates a given DSS to a specific net. These nets are used by video engineers for photo data evaluation and photo acquisition information.</p>				
42	DSS 2	MD	LUNAR ORBITER	R. B. Rung
<p>This net is used to patch tracking station voice nets to all areas. SNOMAN provides patches allowing tracking stations in operation to be heard. DSS 41, 61, and 21 may appear. The communications status display board or SNOMAN correlates a given DSS to a specific net. These nets are used by video engineers for photo data evaluation and photo acquisition information.</p>				
43	SPAA 3	MD	LUNAR ORBITER	R. B. Rung
<p>This is the SPAC director's net, interfacing with other operational areas and carrying only milestone data of SPAC functions, and is used for command conferences, major troubles, and analysts' reports.</p>				
44	SPAA 4	MD	LUNAR ORBITER	R. B. Rung
<p>This is the SPAC analysts' net, permitting discussion of telemetry data, data formats, minor troubles, command preparation.</p>				
45	DATA CONTROL	MD	LUNAR ORBITER	R. B. Rung
<p>This computer control net carries computer status, telemetry edit tables in operation, data being processed, identifies user programs which have been run, and processes troubles. It also carries information about computer operational modes.</p>				
46	MAA	MD	LUNAR ORBITER	R. B. Rung
<p>This is the mission advisors net, an internal conference net for contacting area directors in emergencies.</p>				
48	MAA-INT	MD	LUNAR ORBITER	R. B. Rung
<p>This is an internal conference net used primarily for coordination purposes for mission advisory personnel.</p>				

Table 2 (contd)

No.	Name	Category	Type	Custodian
6	SPAC/AO	MD	SURVEYOR	R. T. Hayes
This is the SPAC internal net, connected to Building AO voice line from prelaunch to about launch plus 1 hr.				
7	TSAC	MD	SURVEYOR	R. T. Hayes
This is the SSAC internal net for TSAC group coordination.				
8	TV DATA	MD	SURVEYOR	R. T. Hayes
This TV-1/TV-11/Telpac technical coordination net is used for (Goldstone) pre-visibility countdown and system calibration; it is disconnected on countdown completion.				
12	FPAC/RTCC	MD	SURVEYOR	R. T. Hayes
This is the FPAC internal net, connected to the RTCC voice line from prelaunch to about launch plus 3 hr.				
14	SUR COMMAND	MD	SURVEYOR	R. T. Hayes
This SFOF/DSS interface for command activity is bridged with the DSS net and connected to station voice line during station transmitting period.				

No.	Name	Category	Type	Custodian
26	TPAC	MD	SURVEYOR	R. T. Hayes
This is the SSAC internal net for Telpac group coordination.				
27	SUR FPAC	MD	SURVEYOR	R. T. Hayes
This is the FPAC internal net.				
29	SURV CONTROL	MD	SURVEYOR	R. T. Hayes
This is the primary SFOF internal mission control net, the interface between ACE 1 and area directors.				
31	TV COORD	MD	SURVEYOR	R. T. Hayes
This is the TVGDHS internal net.				
32	SURV COORD	MD	SURVEYOR	R. T. Hayes
This is the backup to the Surveyor control net; it also takes care of unplanned interfaces and discussions too lengthy for the Surveyor control net.				
37	SURV SPAC	MD	SURVEYOR	R. T. Hayes
This is the SPAC internal net.				